

DEVELOPMENT OF HDPE COMPOSITE FOR BIOMEDICAL APPLICATION USING 3D PRINTING

Thesis

Submitted in partial fulfillment of the requirement for the degree of

DOCTOR OF PHILOSOPHY

by

PRAVEEN J



DEPARTMENT OF MECHANICAL ENGINEERING
NATIONAL INSTITUTE OF TECHNOLOGY KARNATAKA

SURATHKAL, MANGALORE – 575025

OCTOBER, 2022

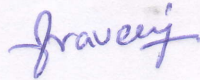
DECLARATION

By the Ph.D. Research Scholar

I hereby *declare* that the Research Thesis entitled “**DEVELOPMENT OF HDPE COMPOSITE FOR BIOMEDICAL APPLICATION USING 3D PRINTING**” which is being submitted to the *National Institute of Technology Karnataka, Surathkal* in partial fulfillment of the requirements for the award of the Degree of *Doctor of Philosophy* in **Department of Mechanical Engineering** is a *bonafide report of the research work carried out by me*. The material contained in this Thesis has not been submitted to any University or Institution for the award of any degree.

Register Number : 165095ME16F10

Name of the Research Scholar : PRAVEEN J

Signature of the Research Scholar : 

Department of Mechanical Engineering

Place : NITK – Surathkal

Date : 03-10-2022

CERTIFICATE

This is to *certify* that the Research Thesis entitled **DEVELOPMENT OF HDPE COMPOSITE FOR BIOMEDICAL APPLICATION USING 3D PRINTING**, submitted by **PRAVEEN J (Register Number: 165095ME16F10)** as the record of the research work carried out by him, is *accepted* as the *Research Thesis submission* in partial fulfilment of the requirements for the award of degree of **Doctor of Philosophy**.

RESEARCH GUIDES



Dr. Srikanth Bontha

Associate Professor

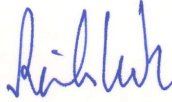


Dr. Mrityunjay Doddamani

Assistant Professor

Department of Mechanical Engineering

NITK, Surathkal.



Chairman – DRPC

Date: 3-12-2022



DEDICATION

I dedicate this Doctoral Dissertation

To my precious parents, Dr. Santhi Muthusamy and Sri. Jeyachandran Ramaraj, who have sacrificed so much for me and supported me all through my life. I am deeply grateful for their support, enduring love and sacrifices.

To my beloved sibling, Smt. Vaishnavi Jeyachandran, who has believed in me unconditionally and never left my side.

To my lovely wife, Girija S, who has continuously supported, motivated and encouraged me and whom I am happy to share my life with.

To my in-laws Sri. Sundararaj and Smt. Thangeswari, who have encouraged and trusted my endeavours.

To my dear friends Pradeep Jeyaraj, Mohammed Aamir, Agnel Xavier Fernando, Thangapandian, Mohammad Sulaiman and Balasubramanian, who have uplifted my mood and kept me optimistic.

And finally, to fellow academicians who continue to spark my interest in science, technology, engineering and mathematics.



ACKNOWLEDGEMENTS

First and foremost, praises and thanks to **GOD** for His showers of blessings throughout my life and for giving me the strength and ability to fulfill my obligations.

This work would not have been possible without the efforts, support, and guidance of many people. I foremost must acknowledge and convey my deep sense of gratitude to my research guides **Dr. Srikanth Bontha**, Associate Professor, Department of Mechanical Engineering, and **Dr. Mrityunjay Doddamani**, Assistant Professor, Department of Mechanical Engineering. My research guides have offered abundant teaching, support, and guidance, for which I am truly grateful. Their success, working style, and mentoring have always inspired me and helped me to become self-motivated and hard-working. I am also thankful to them for giving me opportunities to work on several projects, which helped me to grow as a researcher.

I am highly grateful to **Dr. Ravikiran Kadoli**, Professor and Head of the Department, and all former HOD's, faculty members, technical and administrative staff of the Mechanical Engineering Department for their help in providing the facilities during my research.

I would like to extend my gratitude to the distinguished members of my Research Progress Assessment Committee (RPAC) committee **Dr. Jeyaraj P**, Associate Professor, Department of Mechanical Engineering, and **Dr. Anandhan Srinivasan**, Professor and former Head of the department, Department of Metallurgical and Materials Engineering for their willingness to serve in their capacity and for imparting extensive knowledge and invaluable mentorship to improve my research.

I am thankful to **Dr. Vamsi Krishna Balla**, Chief Scientist and Head, Bioceramics & Coating Division, and **Dr. Subhadip Bodhak**, Senior Scientist, Bioceramics & Coating Division, CSIR-Central Glass & Ceramic Research Institute (CGCRI), Kolkata, India for extending biological characterization facilities during my research and also for their valuable inputs to me during various stages of my research.

I am grateful to **Dr. K Narayan Prabhu**, Professor and Head, **Dr. Udaya Bhat**, Professor and former Head, and **Dr. Mohammed Rizwanur Rahman**, Associate Professor of Department of Metallurgical and Materials Engineering, and **Dr. Suresha S N**, Associate Professor of Department of Civil Engineering, and **Dr. Adka Nityanandha Shetty**, Professor, and **Dr. Darshak R Trivedi**, Associate Professor of

Department of Chemistry and **Dr. Gangadharan K V**, Professor and **Dr. Pruthviraj U**, Assistant Professor at Centre for System Design (CSD) for permitting me to utilize their facilities as and when needed to carry out my research.

I am grateful to my fellow senior researchers Dr. Rakesh K Rajan, Dr. Mallikarjuna B, Dr. Jayavardhana, Dr. Mahantayya Mathapati, Dr. Ashrith, Dr. Sunil Waddar, Dr. Prasanth, Dr. Vinay Vargheese, Dr. Nithin, late Dr. Veeresh Nayak, Dr. Prabhukumar, Dr. Marimuthu and Dr. Pragadeesh for showing me the ropes during various stages of my research.

I want to acknowledge Dr. Mohammed Khalifa and Mr. Govindh Ekbote of Polymers and Advanced Nanofibers Group, Department of Metallurgical and Materials Engineering, for their assistance during various stages of my research.

I want to thank Mr. Aakash and his associates from Aha!3D, Jaipur, India, for their relentless assistance.

I cherish the time spent with Advanced Manufacturing and Additive Manufacturing Laboratory members for all the helpful discussions and assistance during my doctoral journey. Thanks to Dr. Balu P Patil, Dr. Uzwalkiran Rokkala, Mr. Jitender Kumar chaurasia, Mr. Ravi Chandan, Mr. Adithya Kale, Mr. Pavan Beeshetty, Mr. Aneesh Patil, Mr. Nithin, Mr. Danish Ashraf and Mr. Bonthu Dileep for their assistance.

I am fortunate to be acquainted with Dr. Narendran Ganesan, Dr. Vijay Gunasekaran, Dr. Prithivirajan Sekar, and Mr. Balaji. They have been empathetic and compassionate and offered emotional and physical assistance whenever needed. I consider myself privileged to have such amazing people in my life. Without them, achieving this goal would not have been possible.

This work has been supported by the Doctoral Fellowship offered by the Ministry of Education, Government of India, and financial assistance from NIT Karnataka. My sincerest gratitude to them for their vital assistance. I would like to acknowledge CRF at NITK for extending access to various characterization facilities.

Finally, to all those I have unintentionally left out that have helped and supported me along the way, I thank you.....!

Praveen J
NITK, Surathkal-575025.

ABSTRACT

Bioactive Glass (BAG) is a biomaterial well known to interact with physiological fluids to form strong bonds with hard (bone) and soft (muscle, tendons, ligaments, etc.) tissue. BAG tends to release ions, prompting amicable cellular response and formation of bone. The inherent brittleness of BAG inhibits its direct use in load-bearing orthopaedic applications. A viable alternative is to develop polymer-based BAG composites. The most affordable way to develop such intricate orthopaedic polymeric implants is by fused filament fabrication (FFF) based on material extrusion additive manufacturing (MEAM). FFF is a 3D printing (3DP) technique that deposits molten particulate reinforced thermoplastics through a heated liquefier and a nozzle. FFF process is one of the enablers of Industry 4.0 in orthopaedics because of its ability to produce customized implants in both lower time and cost.

The initial part of the present work aims to develop high density polyethylene (HDPE) reinforced with BAG (H/BAG) composites as feedstock for the FFF process. HDPE is the bio-inert constituent responsible for structural integrity, and BAG is the bioactive constituent responsible for biological interactions. Additionally, neat HDPE (H) filament feedstock is developed to evaluate the baseline properties. The degradation behaviour of as received HDPE granules (H_G) was evaluated to find the operable temperature ranges for composite development and filament extrusion. The composite blends are developed using the melt compounding technique. Micrography and elemental mapping of the composite blends reveal uniform distribution of BAG in HDPE matrix without any agglomeration.

Neat H and composite H/BAG filament feedstock are extruded using a single screw extruder. Diameter, density, void content, thermal stability, thermal properties, and tensile properties of the developed filament feedstock are evaluated. The diameter of the feedstock is found to be within the permissible limit favourable for 3DP. Density and void content increase with BAG addition of 5 (H_5), 10 (H_{10}), and 20 (H_{20}) wt.% respectively. Furthermore, the thermal stability of the filament feedstock is marginally improved when compared with H_G . Crystallization temperature (T_c) and tensile modulus increase with BAG addition, although melting temperature (T_m)

remains unaffected. Crystallinity and tensile strength decrease with BAG addition. The stiffer composite filament feedstock is effortlessly spooled and stored. Additionally, the filaments resist the forces exerted at the printer head and maintain the circular cross-section without any slippage during printing at elevated material flow rates.

A deeper understanding of the process parameters influencing the FFF process is essential to print the newly developed filament feedstock. The second part of the present work aims to fabricate stable, defect-free printed parts by carefully identifying the influencing print parameters and their effect on print quality. The effect of BAG on the thermal and melt behaviour of developed semicrystalline feedstock is evaluated, and print parameters are manipulated effectively to achieve high quality prints.

From both calorimetric and diffraction analysis, the crystallinity of the prints is found to be decreasing with BAG addition. The printed samples exhibit higher crystallinity than their respective filaments. The complex viscosity of the prints increases with BAG addition, which denotes the increased resistance to the material flow of the composites. The coefficient of thermal expansion (CTE) is inversely proportional to the prints' dimensional stability. As CTE decreases with BAG addition, the composite prints are observed to be dimensionally stable. Optical warpage and shrinkage analysis show the reduction in warpage with BAG addition. Furthermore, optical analysis confirms that the combined warpage and shrinkage of the prints lie in a narrow range. This indicates the effective selection of material flow rate despite having different melt viscosity. Storage and loss modulus of the composites increases with BAG addition.

The samples are printed using styrene-ethylene-butylene-styrene (SEBS) adhesive, which exhibited adequate adhesion during printing and effortless detachment after printing. The influencing process parameters such as printing temperature (T_p), bed or substrate temperature (T_b), build envelope temperature (T_e), printing speed, and material flow rate are found to be affected by feedstock properties such as crystallinity, melting temperature, crystallization temperature, and viscosity. The resulting print induced defects are observed to be warpage, shrinkage, inept diffusion, delamination, voids, nozzle clogging, underfill and overfill.

Adhesion is improved by enhancing T_b (value closer to crystallization temperature), thereby controlling the warpage and peeling of the initial first layer. Uniform temperature distribution is achieved by increasing T_e , thereby nullifying delamination of prints because of homogeneous thermal stress distribution. Print induced defects such as inept diffusion and voids are eliminated by increasing T_p and material flow rate. Furthermore, all the completed prints are left inside the print chamber and allowed to cool by natural convection, thereby reducing thermally induced stress. It is observed that the prints fabricated at elevated temperatures are dimensionally stable. Process parameters are optimized to obtain stable, defect-free, dense prints.

The mechanical behaviour of the printed samples is evaluated as the final part of the present work. The effect of BAG addition on tensile, flexural, static, and quasi-static compression, impact, and DMA behaviour of the prints is investigated. Structure-property correlation of the properties is explained with extensive micrographic images to understand the deformation mechanism.

Tensile modulus is observed to be increasing with BAG addition, and ultimate tensile strength is observed to be decreasing with BAG addition. The fracture strength of the samples increases with BAG addition. Printed samples exhibit higher tensile modulus and ultimate tensile strength than their respective filament. The printed neat H samples display a 26% higher modulus than injection moulded samples. The deformation of H/BAG composites under tensile load is observed in three stages. Micrographs show various features like voids, dimples, fibrils, and coalescence. The flexural modulus and strength of the composites are higher than the neat H samples. Stiffer BAG acts as stress concentrators, thereby increasing flexural strength. The printed neat H samples show 1.85 times higher flexural modulus when compared with injection moulded counterparts.

All the compression samples exhibit the same levels of strain and similar deformation features irrespective of strain rate (static and quasi-static). Stress-strain curves are divided into three distinct regions to understand the deformation mechanism. The fractured surface shows brittle surface, wrinkles, fibrils (buckled, elongated, ruptured,

peeled), voids, crazes, cracks, and ductile bands. Irrespective of strain rate (static and quasi-static), compression strength and modulus increase with BAG addition. Energy absorption of the developed composites improved with BAG addition. Yield strain is observed to be decreasing with BAG addition.

The impact properties of the prints are studied. The impact strength of the samples decreases with BAG addition. Micrographs show that the insufficient adhesion between HDPE matrix and BAG results in swift propagation of cracks. Localized plastic deformation followed by void formation is also observed from the micrographs. Viscoelastic properties of the developed feedstock are evaluated by dynamic mechanical analysis. Storage and loss modulus is found to be increasing with BAG addition. Storage modulus is observed to be decreasing with sweep temperature. Loss modulus increases with temperature until α - relaxation of the HDPE matrix and then starts decreasing. The changes in storage modulus, loss modulus, and loss factor with increase in temperature below the melting point indicate the disappearance of crystal phases that restrict the mobility of the amorphous phase. This emphasizes the necessity of considering the temperature-dependent viscoelastic properties while designing the H/BAG implants. At the clinical temperature of 37 °C, storage modulus, loss modulus, and loss factor are observed to increase with BAG addition highlighting the enhanced ability to dissipate energy.

Selective mechanical properties of the developed feedstock are compared with other bioactive thermoplastic composites processed via the traditional manufacturing processes. Furthermore, the obtained results are compared with trabecular and cortical bone properties. The obtained results illustrate strong potential of FFF process to fabricate customized orthopaedic implants to mimic human bone.

Keywords: Bioactive Glass, High Density Polyethylene, Fused Filament Fabrication, 3D Printing, Material Extrusion Additive Manufacturing, Filament Feedstock, Printability, Rheology, Dynamic Mechanical Analysis, Warpage Analysis, Polymer Composites, Mechanical Behaviour.

CONTENTS

DECLARATION

CERTIFICATE

DEDICATION

ACKNOWLEDGEMENTS

ABSTRACT

CONTENTS.....	i
LIST OF FIGURES	v
LIST OF TABLES.....	ix
ABBREVIATIONS	xi
NOMENCLATURE	xv
1 INTRODUCTION	1
1.1 Additive manufacturing (AM)	1
1.2 Polymer AM.....	2
1.3 AM process chain.....	4
1.4 MEAM process	5
1.5 Filament feedstock for FFF process	6
1.5.1 Feedstock requirements	7
1.5.2 Pure filament feedstock.....	8
1.5.3 Composite filament feedstock.....	10
1.6 Limitations of FFF process	12
1.7 Literature Review	13
1.8 Summary of literature survey	39
1.9 Motivation	39
1.10 Objectives and scope of the work.....	40
1.11 Outline of the thesis	41
2 MATERIALS AND METHODS.....	43
2.1 Constituents.....	43
2.1.1 Bioactive glass	43
2.1.2 HDPE	43
2.2 Thermogravimetric analysis (TGA).....	45
2.3 Differential scanning calorimetry (DSC).....	45

2.4	Melt compounding and filament extrusion	46
2.5	X-ray diffraction (XRD).....	48
2.6	Rheology	49
2.7	Density measurement	49
2.8	Build plate adhesive preparation	50
2.9	FFF of developed feedstock	50
2.10	Coefficient of thermal expansion (CTE)	52
2.11	Warpage analysis.....	52
2.12	Melt flow index (MFI).....	53
2.13	Tensile test.....	53
2.14	Flexural test	54
2.15	Compression test.....	55
2.16	Impact.....	56
2.17	Dynamic mechanical analysis (DMA)	56
2.18	Scanning electron microscopy.....	57
3	COMPOSITE BLENDS AND FILAMENT FEEDSTOCK CHARACTERIZATION	59
3.1	Melt characterization.....	59
3.1.1	Micrography of composite blends	59
3.2	Filament characterization	61
3.2.1	Density and void content of filament feedstock	61
3.2.2	Thermal properties of extruded filaments.....	62
3.2.3	XRD analysis of extruded filaments	66
3.2.4	Tensile properties of filament feedstock.....	67
3.2.5	Micrography of filament feedstock.....	68
3.3	Conclusions	70
4	PRINTABILITY	73
4.1	Substrate and print adhesion	73
4.2	Thermal behaviour analysis	74
4.2.1	Thermal gravimetric analysis (TGA).....	74
4.2.2	Differential scanning calorimetry (DSC).....	76
4.2.3	X-ray Diffraction	77
4.2.4	Coefficient of thermal expansion (CTE).....	78

4.2.5	Thermal behaviour and printability of H/BAG composites.....	79
4.2.6	Warpage analysis	82
4.3	Melt behaviour analysis	84
4.3.1	Melt flow index (MFI).....	84
4.3.2	Rheology.....	85
4.3.3	Melt behaviour and printability of H/BAG composites.....	87
4.4	Surface and microstructural features of printed samples	87
4.5	Conclusions	90
5	TENSILE PROPERTIES.....	93
5.1	Tensile properties of neat H and H/BAG prints.....	93
5.2	Micrographic analysis of fractured samples.....	95
5.3	Property map	96
5.4	Conclusions	97
6	FLEXURAL PROPERTIES	99
6.1	Flexural properties of neat H and H/BAG composites	99
6.2	Micrographic analysis	100
6.3	Property map	101
6.4	Conclusions	102
7	COMPRESSION PROPERTIES	105
7.1	Compression properties of neat and H/BAG composites	105
7.2	Static compression.....	106
7.2.1	Micrography analysis.....	107
7.2.2	Property map.....	110
7.3	Quasi-static compression.....	111
7.3.1	Micrographic analysis.....	112
7.4	Conclusions	117
8	IMPACT TEST.....	119
8.1	Impact test	119
8.2	Micrography analysis	119
8.3	Conclusions	119
9	DYNAMIC MECHANICAL ANALYSIS.....	121
9.1	Temperature sweep	121
9.2	Conclusions	123

10	SUMMARY AND CONCLUSIONS	127
10.1	Summary.....	127
10.2	Conclusions	128
	SCOPE OF FUTURE WORK	134
	REFERENCES	135
	LIST OF PUBLICATIONS	151
	BIO-DATA	153

LIST OF FIGURES

Figure 1.1. Classification of AM processes based on different context.	3
Figure 1.2. Overview of polymer materials for additive manufacturing and their applications.	4
Figure 1.3. AM process flow for FFF process.	5
Figure 1.4. Schematic of FFF process.	7
Figure 1.5. Vital filament properties and their influence on FFF processability and part properties.....	8
Figure 1.6. Overview of filaments available for FFF from literature.	9
Figure 2.1. Representative images of (a) Ball milled, (b) micrographic morphology and (c) particle distribution of BAG and (d) Granular HDPE used in the present investigation.....	44
Figure 2.2. Thermogravimetric analyser (TGA 4000, PerkinElmer, USA).....	45
Figure 2.3. Differential scanning calorimeter (DSC 6000, PerkinElmer, USA).	46
Figure 2.4. Melt compounder (Haake Rheomex PTW 16 OS, Thermo Fisher Scientific, Germany), (b) H ₂ O melt blend, (c) single-screw extruder (25SS/MF/26, Aasabi Machinery Pvt Ltd, India) and (d) H ₂ O filament feedstock.	47
Figure 2.5. X-ray diffractometer (Empyrean 3rd Gen, Malvern PANalytical, Netherlands).....	48
Figure 2.6. Rheometer (Anton Paar Rheometer, MCR 502, Austria).....	49
Figure 2.7. Density measurement kit.	50
Figure 2.8. FFF based 3D printer (Protocentre 999, AHA 3D, Jaipur, India).	51
Figure 2.9. (a) CAD model of warpage sample (All dimensions are in mm) and (b) Hand-held 3D scanner (Artec 3D Space Spider, USA).	52
Figure 2.10. Melt flow index (MFI) apparatus (Zwick Roell Mflow, USA).....	53
Figure 2.11. Tensile test on (a) filament feedstock and (b) printed tensile specimen with an extensometer attachment.	54
Figure 2.12. Flexural test using 3-point bending configuration.....	55
Figure 2.13. Compression test setup.	56
Figure 2.14. Impact test apparatus (ZWICK ROELL HIT50P, USA).....	56

Figure 2.15. (a) Dynamic mechanical analyser apparatus and (b) 3-point bending configuration.....	57
Figure 2.16. (a) Field emission scanning electron microscope (CARL ZEISS, FESEM, Germany) and (b) optical microscope (Zeiss, Germany).....	58
Figure 3.1. BAG distribution (a), (c) and (e) and corresponding elemental mapping (b), (d), and (f) of respective H ₅ , H ₁₀ , and H ₂₀ blends.....	60
Figure 3.2. BAG distribution and HDPE-BAG interface of (a) H ₅ , (b) H ₁₀ and (c) H ₂₀ blends in higher magnification.....	61
Figure 3.3. Diameter of the extruded filament feedstock.	62
Figure 3.4. Representative (a) TGA and (b) DTG of H _G and filament feedstock.	63
Figure 3.5. Representative (a) cooling (in-sets showing cold-crystallization phenomenon) and (b) heating curves of H _G and filament feedstock.	65
Figure 3.6. Representative XRD pattern of (a) BAG and H _G and (b) filament feedstock.	66
Figure 3.7. (a) Tensile response of the developed neat H and H/BAG composite feedstock and (b) circular cross-section of the extruded filaments. Representative feedstock, filaments and print of (c) H, (d) H ₂₀ composites and (e) show an increase in turbidity of filaments with BAG addition.....	69
Figure 3.8. BAG distribution (a), (c) and (e) and corresponding elemental mapping (b), (d), and (f) of respective H ₅ , H ₁₀ , and H ₂₀ filaments.....	70
Figure 4.1. Substrates used to print HDPE. (a) HDPE plates (HS et al. 2020, Patil et al. 2019) (b) SEBS plates (Schirmeister et al. 2019) and (c) SEBS adhesives applied over Kapton tape struck on to the heated glass plate (present work).....	74
Figure 4.2. Representative (a) TGA and (b) DTG curves of printed samples.	75
Figure 4.3. DSC curves for (a) cooling cycle with in-sets showing cold-crystallization phenomenon and (b) second heating cycle print samples.....	77
Figure 4.4. XRD of printed samples.	78
Figure 4.5. CTE values printed samples.	79
Figure 4.6. Representation of printing defects such as (a) warpage, (b) inept diffusion, (c) delamination, (d) print induced voids, (e) clogging, (f) underfill and (g) overfill.	80
Figure 4.7. Representative dimensionally stable neat H (a,c) and H ₂₀ samples (b,d). (Arrow indicating build direction).....	81

Figure 4.8. Optical warpage analysis of (a) neat H, (b) H ₅ , (c) H ₁₀ , and H ₂₀ printed samples. All dimensions are in mm.	83
Figure 4.9. MFI of feedstock composites.	84
Figure 4.10. (a) Storage modulus, (b) loss modulus and (c) complex viscosity of printed samples at 240 °C frequency sweep.....	86
Figure 4.11. Micrographs of (a) surface topography and seamless layer interface and (b) freeze fractured neat H printed samples. (c) Freeze fractured and (d) BAG distribution in H ₂₀ printed samples. Printed (e) human mandible and (f) segment of cranium.	89
Figure 5.1. Stress – strain curves of (a) neat H and (b) H/BAG printed samples.....	94
Figure 5.2. Photograph showing failure of tensile samples.	94
Figure 5.3. Micrography of fractured (a) H ₁₀ and (b) H ₂₀ tensile samples showing stiffer BAG and deformation features such as fibrils, voids and coalesce.	96
Figure 5.4. Tensile properties of the developed composites are compared with properties of biocompatible composites from the available studies.	97
Figure 6.1. Flexural response of the printed samples.	99
Figure 6.2. Micrography of the freeze fracture post flexural (a) neat H and (b) H ₂₀ samples.....	101
Figure 6.3. Flexural properties of the developed composites are compared with properties of biocompatible composites from the available studies.	103
Figure 7.1. Schematic of stress-strain response of neat H samples showing three distinct regions (I - elastic, II - plateau and III – densification regions).	106
Figure 7.2. Compressive response of printed samples.....	107
Figure 7.3. Micrography showing ductile damage under compression load: (a) fibril formation and void elongation of neat H sample (Region – I), (b) ruptured fibrils due to void elongation of H ₅ samples, (c) slenderous microfibril of H ₁₀ sample (Region – I), formation crazes and crack propagation normal to the elongation direction of (d) neat H and (e) H ₂₀ sample (Region – II), and (f) severe plastic collapse of H ₂₀ sample (Region – III).	109
Figure 7.4. Compressive properties of the developed composites are compared with properties of biocompatible composites from the available studies.	111

Figure 7.5. Representative stress-strain plots at different strain rates of (a) 0.001, (b) 0.01, and 0.1 s ⁻¹	112
Figure 7.6. Compression sample (a) before the test and (b) showing barrelling effect – after the test. Polished H ₂₀ post-compression samples in (c) transverse and (d) longitudinal directions. Optical micrography of polished post-compression samples showing shear bands (e-f).	114
Figure 7.7. Micrography showing various features under compression load (a) wrinkles and brittle fracture, (b) HDPE fibrils and stiffer BAG, (c) void elongation and fibril formation, (d) fibril peeling, ductile bands and elongation direction at higher magnification (e) voids, ruptured and buckled fibrils and (f) craze formation and crack propagation	115
Figure 8.1. Impact strength of printed samples.....	120
Figure 8.2. Micrographs of fractured (a) neat H and H ₂₀ samples.....	120
Figure 9.1. (a) Storage modulus, (b) loss modulus, and (c) Tan δ results from temperature sweep at 1 Hz.	125
Figure 9.2. (a) Storage modulus, (b) loss modulus, and (c) Tan δ results from temperature sweep at 10 Hz.	126

LIST OF TABLES

Table 1.1. Literature survey on filament feedstock extrusion of thermoplastics and its composites.....	15
Table 1.2. Literature survey on 3D printing of thermoplastics and its composites.	20
Table 1.3. Literature survey on biomedical applications of BAG.	29
Table 1.4. Literature survey on biomedical applications of HDPE and its composites	34
Table 2.1. Properties of HDPE grade 180M50 used in the present investigation.	44
Table 2.2. FFF parameters used in the present investigation.....	51
Table 3.1. Density and void content of the developed filament feedstock.	62
Table 3.2. Thermal degradation properties of H _G and filament feedstock.	64
Table 3.3. Thermal properties and crystallinity of H _G and filament feedstock.	65
Table 3.4. Tensile properties of filament feedstock.....	68
Table 4.1. Thermal degradation of printed samples.	75
Table 4.2. Thermal properties of printed samples.	77
Table 4.3. CTE and % reduction in CTE values of printed samples.	79
Table 4.4. MFI and percentage reduction MFI of feedstock composites.	85
Table 4.5. Rheological properties of the printed samples.....	86
Table 4.6. Density and void content of printed samples.....	90
Table 5.1. Tensile response of printed samples.	95
Table 6.1. Flexural properties of the printed samples.....	100
Table 7.1. Compressive properties of printed samples.	107
Table 7.2. Quasi-static compression behaviour of printed samples at 0.001, 0.01 and 0.1 s ⁻¹	116
Table 8.1. Impact strength and % reduction in impact strength of printed samples..	120
Table 9.1. Comparison of storage modulus, loss modulus and Tan δ of samples from temperature sweep at 1 Hz and three representative temperatures	124
Table 9.2. Comparison of storage modulus, loss modulus and Tan δ of samples from temperature sweep at 10 Hz and three representative temperatures	124
Table 9.3. Storage modulus, loss modulus and Tan δ at the physiological condition of	125

ABBREVIATIONS

3DP	: 3-Dimensional Printing
ABS	: Acrylonitrile butadiene styrene
AM	: Additive Manufacturing
AMP	: Amorphous Magnesium Phosphate
ASA	: Acrylonitrile-Styrene-Acrylate
ASTM	: American Society for Testing and Materials
BAG	: Bioactive Glass
BN	: Boron nitride
CAD	: Computer-Aided Design
CaP	: Calcium Phosphate
CB	: Carbon Black
CF	: carbon fibre
CNT	: Carbon nanotubes
CTE	: Coefficient of Thermal Expansion
Cu	: Copper
DIW	: Direct Ink Writing
DMA	: Dynamic Mechanical Analysis
DSC	: Differential Scanning Calorimetry
DTG	: Derivative Thermogravimetry
FDM	: Fused Deposition Modelling
FFF	: Fused Filament Fabrication
GF	: Glass Fibre
HAp	: Hydroxy apatite
HDPE	: High Density Polyethylene

HIPS	: High Impact Polystyrene
LAAM	: Large Area Additive Manufacturing
LDPE	: Low Density polyethylene
LENS TM	: Laser Engineered Net Shaping
MEAM	: Material Extrusion Additive Manufacturing
MFI	: Melt Flow Index
MTT	: (3-(4,5-Dimethylthiazol-2-yl)-2,5-Diphenyltetrazolium Bromide)
MWCNT	: Multiwalled carbon nanotubes
OM	: Optical Microscopy
OMMT	: Organo-modified montmorillonite
PA	: Polyamide
PAEK	: Polyaryl ether ketone
PAI	: Polyamide
PBS	: Phosphate Buffer Solution
PC	: Polycarbonate
PCL	: Polycaprolactone
PE	: Polyethylene
PEEK	: Polyether ether ketone
PEI	: Polyethylenimine
PEK	: Polyether ketone
PEKK	: Polyether ketone ketone
PES	: Polyether sulfone
PET	: Polyethylene terephthalate
PETG	: Polyethylene terephthalate glycol
PGA	: Polyglycolic acid

PI	: Polyimide
PLA	: Polylactic acid
PLGA	: Polylactic coglycolic acid
PMMA	: Polymethyl metha acrylate
PP	: Polypropylene
PPS	: Polyphenylene sulfide
PS	: Polystyrene
PSU	: Polysulfone
PTFE	: Polytetra fluoroethylene
PVA	: Polyvinyl acetate
PVC	: Polyvinyl chloride
PVDF	: polyvinylidene difluoride
SBF	: Stimulated Body Fluid
SEBS	: Styrene-ethylene-butylene-styrene
SEM	: Scanning Electron Microscope
stl	: Standard Triangle Language or Standard Tessellation Language
TCP	: Tri-calcium phosphate
TGA	: Thermogravimetric Analysis
TPE	: Thermoplastic Elastomer
TPU	: Thermoplastic polyurethane
UHMWPE	: Ultra High Molecular Weight Polyethylene
USD	: United States Dollar
UTS	: Ultimate Tensile Strength
UV	: Ultra-Violet
XRD	: X-ray Diffraction

NOMENCLATURE

G	Granules	-
ρ_t	Theoretical density	kg/m ³
ρ_m	Density of the matrix	kg/m ³
V_m	Volume fraction of matrix	%
ρ_f	Density of the filler	kg/m ³
V_f	Volume fraction of filler	%
Φ_V	Void content	%
ρ_t	Theoretical density	kg/m ³
ρ_e	Experimental density	kg/m ³
T_p	Print temperature	°C
T_b	Bed temperature	°C
T_e	Build envelope temperature	°C
LT	Layer thickness	mm
X_c	Degree of crystallinity	%
ΔH_f	Heat of fusion	J g ⁻¹
ΔH_f^*	Heat of fusion per gram for 100% crystalline HDPE	J g ⁻¹
wt	Weight	%
I_c	Integral intensity of crystalline phase	-
I_a	Integral intensity of amorphous phase	-
E_{fM}	Flexural modulus	MPa
σ_{fS}	Flexural strength	MPa
L	Length of support span	mm
b	Width of the beam	mm
d	Thickness of the beam	mm
m	Slope of the tangent to the initial linear portion of the load deflection curve	-

P	Load	N
ϵ_{40}	Strain at 40%	MJ/m ³
σ	Stress	MPa
T_{d5}	On-set degradation temperature	°C
T_{dmax}	Maximum degradation temperature	°C
T_c	Crystallization temperature	°C
T_m	Melting temperature	°C
G'	Storage modulus	Pa
G''	Loss modulus	Pa
η'	Complex viscosity	Pa s
E'	Storage modulus	MPa
E''	Loss modulus	MPa
$Tan \delta$	Damping factor	-

1 INTRODUCTION

1.1 Additive manufacturing (AM)

Additive Manufacturing (AM) refers to technologies that produce end products without any dies or tooling. This provides AM technologies with design freedom to manufacture any shapes without constraints. Compared to conventional manufacturing methodologies, AM processes combine materials layer by layer based on the CAD model. AM favours on-demand manufacturing as it does not require specific tooling, thus eliminating longer lead times. AM can achieve zero-waste manufacturing because of its weight-saving tendency compared to conventional manufacturing processes. Due to the design and manufacturing feasibility of producing functional and complex intricate structures by AM, the need to assemble multiple parts is eliminated. Also, AM technologies have proven to be sustainable manufacturing practices with the potential to reduce 525.5 metric tonnes of carbon footprint by 2025 (Tan et al. 2020). Further, the product development cost and time to market the products are significantly reduced by 70 and 90%, respectively, compared to conventional manufacturing processes (Gebler et al. 2014). This makes AM global market valued at 23 billion USD by 2023, along with a 22% compound growth rate (Ribeiro et al. 2020). All these qualities propel AM technologies essential for Industry 4.0.

In spite of the promise shown, AM technologies face several challenges. Primarily, AM is focused on producing a low volume of customized products, which makes it challenging to match the economic scales of bulk-quantity products produced by conventional manufacturing (Vaes and Van Puyvelde 2021). Furthermore, the design of complex structure with overhangs and undercuts necessitates additional support structures. Such support structures fabricated from sacrificial materials are removed by additional post-processing operations. Water or solvent-soluble supports are generally dissolved in respective solutions, and non-soluble supports are mechanically removed from the printed samples (Siacor et al. 2021). Due to characteristic layer-by-layer manufacturing, the resulting printed samples often suffer from insufficient interfacial adhesion, porosity, and anisotropic mechanical properties. This emphasizes the need for a systematic study of the effect of parameters on the quality of printed samples

(Petersmann et al. 2020). AM technologies are applied in several fields such as automotive, aerospace, biomedical, electronics etc. Furthermore, AM technologies are classified into three major categories, as depicted in Figure 1.1 (Saleh Alghamdi et al. 2021).

1.2 Polymer AM

Polymers are macromolecules fundamentally made of repeating units bonded through a covalent bond. Polymers are classified based on thermomechanical properties into thermoplastics and thermosets. AM technologies use polymers and their composites to fabricate products with enhanced biological, corrosion, mechanical, electrical, optical, and thermal properties (Tan et al. 2020). Smart structures which respond to external stimuli such as light, temperature, moisture, stress, electric and magnetic fields can also be produced by AM. This gives rise to a sub-set of AM technologies called 4D printing, with time as the fourth dimension (Peng et al. 2020). Feedstock in the form of powders, inks, filaments, and resins are widely used in polymer AM processes. They cater to biomedical, aerospace, automotive, robotics, marine, smart structures, and electronics applications. Figure 1.2 shows the various AM technologies that used polymer in various forms as feedstock and their associated field of applications.

Initially, polymer AM was used to produce prototypes due to their limited strength and surface properties. Due to increased demands such as reproducibility, functionality, and appropriate properties for real-time applications, extensive research has been conducted to introduce new materials as polymer feedstock for AM (Vaes and Van Puyvelde 2021). On the other hand, continuous improvements are being made, making polymer AM processes to utilize a broad spectrum of materials with higher accuracy, faster feed rates and better resolution (Saleh Alghamdi et al. 2021). With this combined effect, researchers have made polymeric near-finished products a reality.

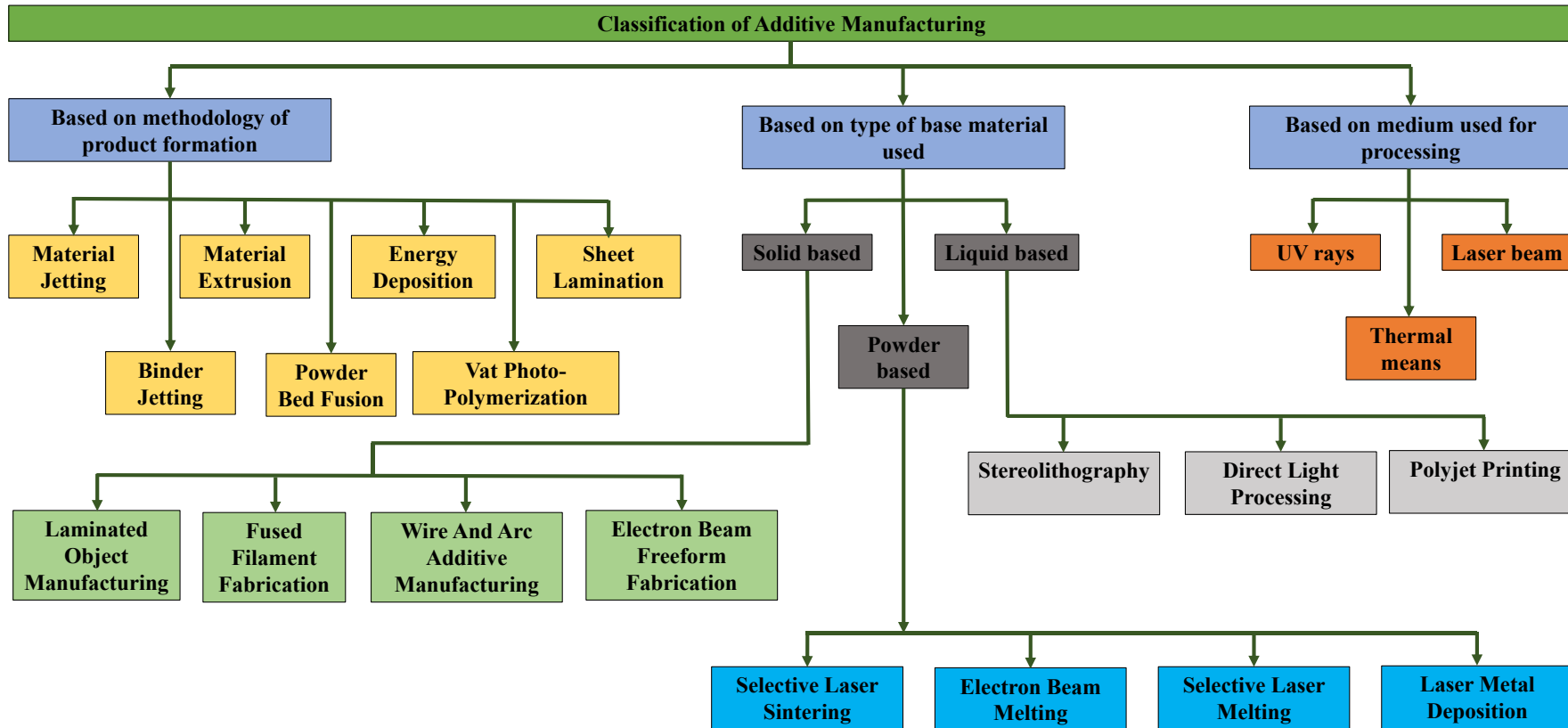


Figure 1.1. Classification of AM processes based on different context.

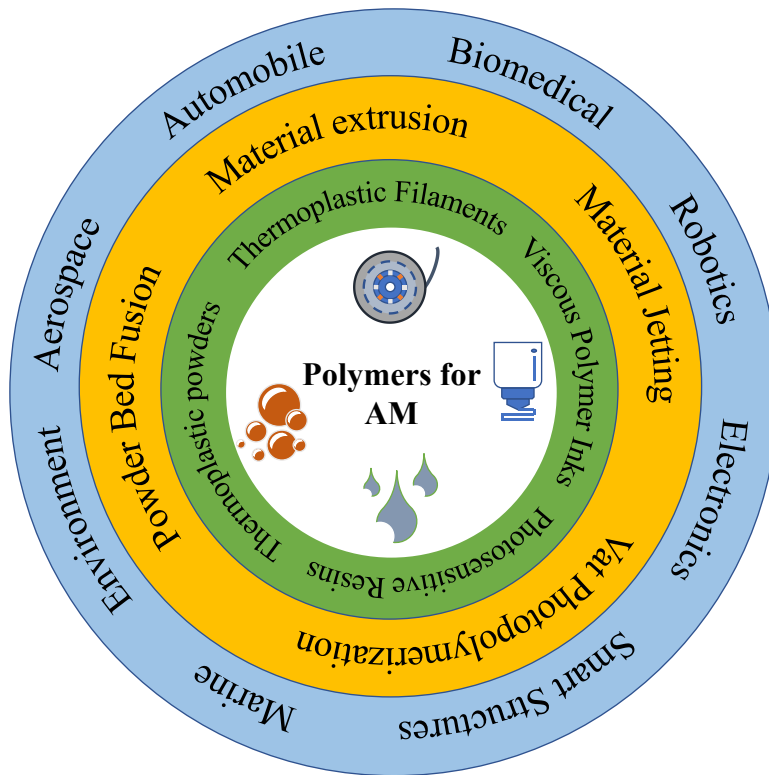


Figure 1.2. Overview of polymer materials for additive manufacturing and their applications.

1.3 AM process chain

AM processes begin with CAD model design in *.stl file format, which constitutes the model in the form of triangular facets (Saleh Alghamdi et al. 2021). A slicing software using these CAD files generates a toolpath with specifics for layer resolution, printing speed, material feed rate, spacing details, environment conditions, particle size, processing temperatures, and print-associated metrics. The generated tool path is similar to codes generated in computer numeric control (CNC) programming. The AM machines use the generated toolpath to fabricate the end products. The present study focuses on FFF based on the material extrusion additive manufacturing (MEAM) process; therefore, the AM process chain for filament feedstock-based FFF processes is depicted in Figure 1.3.

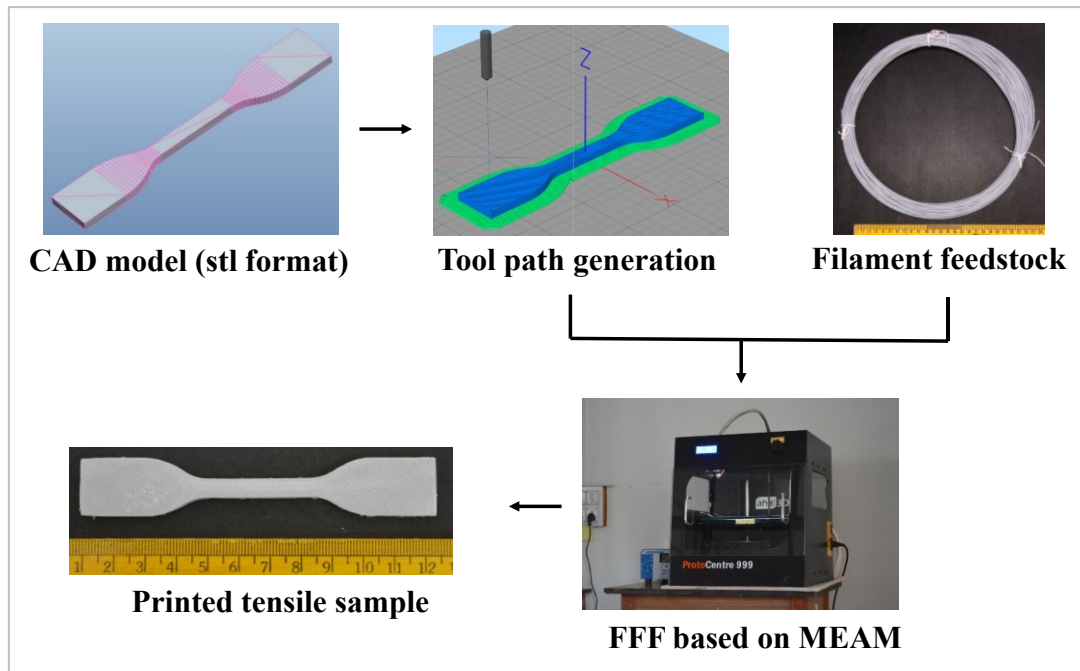


Figure 1.3. AM process flow for FFF process.

1.4 MEAM process

MEAM process uses feedstock in the form of filaments, viscous inks, or pellets. The continuous extrusion of feedstock via heated nozzle or orifice onto the build plate or substrate and subsequent solidification results in the fabrication of final printed samples. The pressure applied during extrusion must be constant to ensure the steady and continuous flow of material.

The MEAM process can be carried out in two different ways. The standard way is to use the temperature to control the material state and flow. The molten feedstock is extruded via a heated nozzle and deposited to form interfacial adhesion with adjacent deposited material while solidifying (Tan et al. 2020). This forms the basis for the FFF technique. FFF is the most commonly used AM process because of its affordability and uses thermoplastic based filament feedstocks. Recent developments in MEAM use pellets as feedstock to directly fabricate the end products without requiring filament as feedstock (Vaes and Van Puyvelde 2021). Such pellet feedstock-based MEAM gives rise to a new domain called large-area additive manufacturing (LAAM). Such a process is being widely used to fabricate fully operational components up to a few meters in

dimension (Lamm et al. 2020). Functionally graded material and multi-material structures are effortlessly fabricated due to the distinct on-the-fly material-changing ability of LAAM processes (Brackett et al. 2021).

The other way of controlling the MEAM process is to solidify the ink-based feedstock via chemical changes (Vaes and Van Puyvelde 2021). Curing agents, chemical reactions, cooling, and drying deposited material are some ways to solidify such feedstock. Direct Ink Writing (DIW), also known as 3D plotting, is a MEAM process that uses viscous ink feedstock in the form of slurry or polymer solution to fabricate components (Konka et al. 2021). DIW operates in ambient temperature conditions with a broad spectrum of printing materials. One of the recent developments of MEAM technologies is bio-printing that is being used to develop functional organs. Bones, muscles, cartilage, tendons, and ligaments are bio-printed using specialized inks made of specific cells, gelatins, PCL, cellulose, alginate, HAp, chitosan, and collagen (Potyondy et al. 2021, Vijayavenkataraman et al. 2018).

The present study focuses on developing filament feedstock for the FFF process for potential orthopaedic applications. Hence the various aspects of filament are discussed herein.

1.5 Filament feedstock for FFF process

FFF typically prints thermoplastics and their composite filament feedstock (Vaes and Van Puyvelde 2021). Recent developments includes the printing of metals and ceramic components by developing metal/ceramic filament feedstock (Singh et al. 2020). Typical FFF (Figure 1.4) process involves a pinch roller feeding the filament into the heated nozzle, where the filament melts and gets pushed by the solid filament that enters the nozzle. The deposited molten filament called raster is solidified on the substrate. The requirements of the filament for successful printing are explained herein.

1.5.1 Feedstock requirements

During the extrusion process, solid filaments are subjected to continuous compressive load. This requires filaments to possess sufficient strength and stiffness to prevent

buckling and slippage between the pinch roller and heated nozzle (Patil et al. 2019). A minimum strain at yielding of 5% is vital for the filaments to be spooled and despoiled for successful printing (Tan et al. 2020). During continuous printing, highly viscous filaments tend to buckle upon melting in the nozzle as it exerts a more significant force on solid filaments. This can be eliminated by keeping the ratio of elastic modulus to viscosity greater than $3 \times 10^5 \text{ s}^{-1}$. An increase in printing temperature is found to decrease the viscosity and enable continuous printing and thereby improve mechanical properties as it enhances interfacial adhesion (Spoerk et al. 2017).

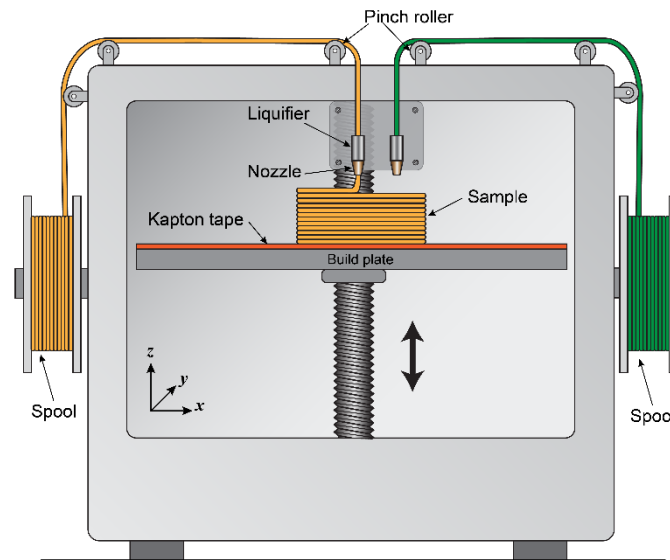


Figure 1.4. Schematic of FFF process.

Inter and intra layer adhesion is improved when the new raster is deposited over and next to the previous raster. The interface between the two rasters is diffused via time-dependent polymer chain diffusion, which significantly depends on the viscosity and thermally induced residual stress (Vaes and Van Puyvelde 2021). Inter and intra layer adhesion also depends on the time interval between the deposition of subsequent rasters. Longer time intervals lead to a decreased temperature at interfaces resulting in inadequate polymer diffusion and adhesion. The resulting printed samples will show anisotropy (Siacor et al. 2021). Printing samples with zero print-induced voids and perfectly diffused rasters, enhances mechanical, electrical, and thermal properties (Saleh Alghamdi et al. 2021).

Amorphous filament feedstock is dimensionally stable (Tan et al. 2020). In contrast, semi-crystalline filament feedstock undergoes crystallinity-induced shrinkage and warpage upon melting and cooling (Spoerk et al. 2020). The dimensional stability of the printed samples significantly depends on crystallinity and Coefficient of Thermal Expansion (CTE). Thermal gradient in the printing environment often leads to warpage and delamination of the resulting prints. For enhanced stability of the printed parts, filament feedstock with lower crystallinity and CTE values is highly recommended. Enhancing the printing (T_p), bed (T_b), and build envelope (T_e) temperatures of semicrystalline feedstock reduces the thermal gradient resulting in dimensionally stable prints (Spoerk et al. 2017). The vital material requirements for successful FFF are summarized in Figure 1.5. FFF process hypothetically allows any thermoplastics, which typically melt upon heating and solidify upon cooling. However, the options are limited because of filament development (Spoerk et al. 2020). The following sections explain various pure and composite filament feedstock in detail.

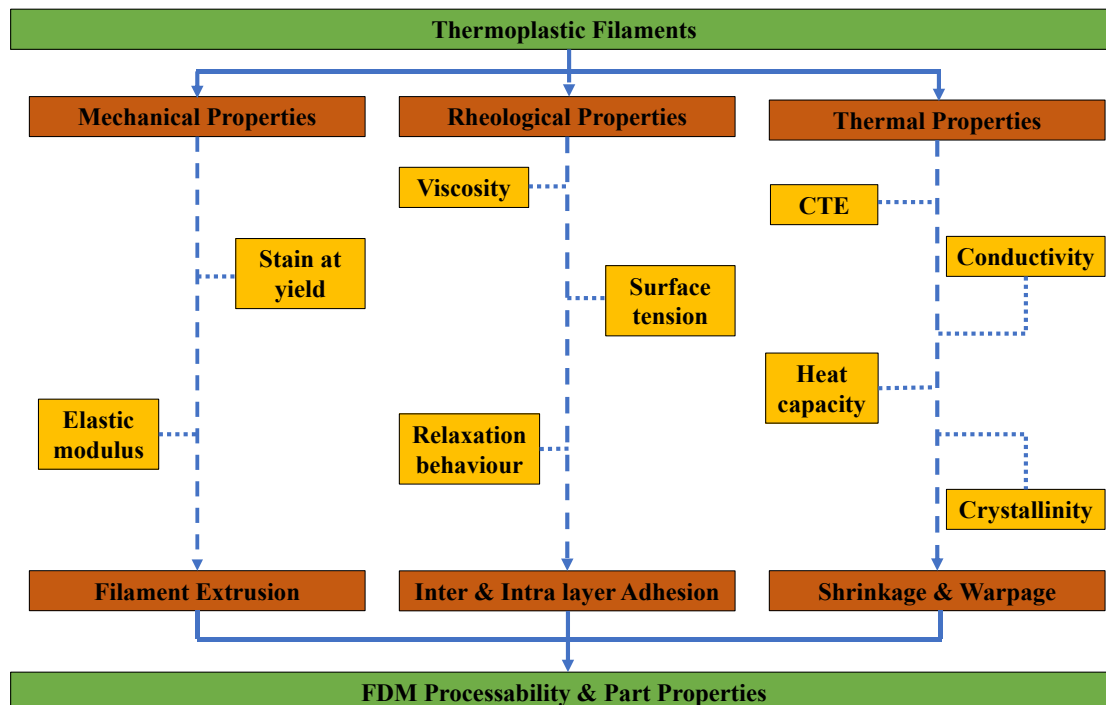


Figure 1.5. Vital filament properties and their influence on FFF processability and part properties.

1.5.2 Pure filament feedstock

Amorphous thermoplastics such as ABS, ASA, PC, and PEI are the most commonly used filament feedstock. Recently an elastomer such as TPE and semicrystalline thermoplastics like PLA, PET, PA, PP, and PEEK have been commercialized as filament feedstock (Al Rashid et al. 2021). Figure 1.6 shows the widely available commercial and laboratory-developed filament feedstock for FFF process.

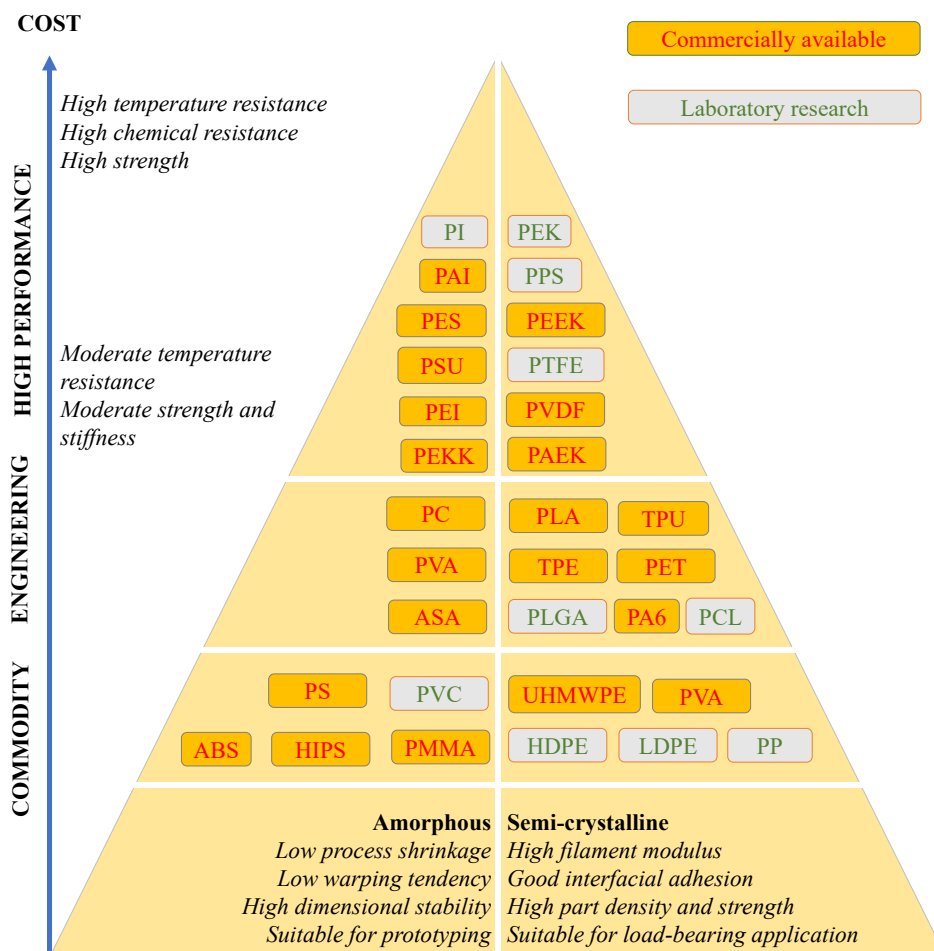


Figure 1.6. Overview of filaments available for FFF from literature.

ABS is the most widely used material in FFF process as it offers durability, toughness, tensile properties, and temperature resistance. ASA is another viable amorphous option, especially for outdoor applications. Due to the acrylate rubber component, ASA is highly weather resistant. A substantial proportion of amorphous thermoplastics are commercialized into filament feedstock as they offer dimensional stability (Vaes and

Van Puyvelde 2021). However, due to their inferior dimensional stability, a small fraction of semicrystalline polymers is commercialized for the FFF process. However, semicrystalline polymers are frontrunners in advancing the FFF process into producing load-bearing consumer products rather than just making prototypes (Saleh Alghamdi et al. 2021).

PLA is a semicrystalline thermoplastic widely used because of low CTE and T_p , better tensile properties, and dimensional stability (Vaes and Van Puyvelde 2021). Further, PLA has the advantage of being a biodegradable polymer derived from renewable sources. PLA components are widely used in households as they are highly reliable and environmentally friendly. The mechanical properties offered by semicrystalline polymers are comparatively higher than their amorphous counterparts (Tan et al. 2020). Hence significant research efforts are being carried out to introduce more semicrystalline thermoplastic polymers for FFF processes.

Several studies have been dedicated towards material development for the FFF process via new polymer, their blends, and composites. Polymer blends are produced to enhance the performance and processibility between amorphous and crystalline polymers. Properties such as higher mechanical properties, isotropy, shape memory, dimensional stability, and smooth surface finish can be obtained from polymer blends. Commercially available polymer blends such as PC/ABS, PC/PEI, ABS/SEBS, PCL/PHBV, UHMWPE/SEBS, and ABS/PTE are widely used in aerospace, automotive, and medical applications (Vaes and Van Puyvelde 2021). Further, the development of polymer blends is restricted by the miscibility of the constituents, melt, and thermal properties. Several research groups are conducting research to optimize the polymer proportion and processing temperature to introduce new polymer blends as filament feedstock (Saleh Alghamdi et al. 2021).

1.5.3 Composite filament feedstock

Composite filament feedstock is developed to enhance mechanical, electrical, thermal, and biomedical properties. Reinforcements are added to improve the aforementioned properties (Dey et al. 2021). The key challenges in developing filament feedstock lie in

extrusion and resulting filament properties. Ideal composite filaments should possess homogeneous filler distribution, zero void content, and continuous extrudability (Tan et al. 2020). The resulting composite filaments must have appropriate melt flow index (MFI), viscosity, coefficient of thermal expansion (CTE), and stiffness to be used in FFF processes. (Singh et al. 2020) The proportion of the filler should be optimum to have the required characteristic improvement, adequate stiffness, and flowability at the heated nozzle. The reinforcements for composite feedstock are classified into particulates and fibers (Saleh Alghamdi et al. 2021).

Particulate reinforced filament feedstock is developed by melt compounding polymers with particulates and that are subsequently extruded into filaments. Such filament feedstock with optimized process parameters is known to produce products with isotropic properties (Spoerk et al. 2017). Various fillers are used to enhance different properties. Engineered hollow particles and cenospheres (waste of thermal power plant) are used to produce filament feedstock to fabricate lightweight products. Such filaments are cost-effective and environmentally friendly (Bonthu et al. 2020, Patil et al. 2019). Electromagnetic devices are fabricated using ceramic particle reinforced filament feedstock (Dey et al. 2021). Metal reinforced filament feedstock has been observed to offer improved stiffness, mechanical, wear, and thermal conductivity properties (Al Rashid et al. 2021). Biological properties of the filament feedstock can be enhanced by reinforcing with bioactive fillers like bioactive glass (BAG), hydroxy apatite (HAp), calcium phosphate (CaP), tri-calcium phosphate (TCP), and zirconia (Rodzeń et al. 2021). Nanofibers such carbon nano tubes (CNT), multi walled CNTs, carbon black (CB), carbon nano fiber (CNF), and graphene are widely used to develop filament feedstock for functional applications involving sensors, electromagnetic shielding, piezoelectric, and shape memory effect (Dey et al. 2021). However, it is advised that the proportion of nanofibers to be kept to a minimum as they tend to agglomerate because of the high surface area to volume ratio (Beesetty et al. 2020). The agglomeration can be mitigated by surface modification of the constituents or by using compatibilizers (Tan et al. 2020).

Fiber-reinforced filament feedstock is produced by incorporating discontinuous and continuous fibers. As fibers tend to align themselves in the print direction, a significant enhancement in properties is observed along the print direction. Fibers such as GF, CF, Kevlar, and those derived from natural sources in dimensions ranging from nanometres to millimetres are used as discontinuous fiber reinforcements (Al Rashid et al. 2021). The extrusion of such fiber-reinforced filament feedstock significantly depends on fiber length and proportion. Longer fibers and increased fiber proportion results in parts with high tensile properties along the print direction. However, filaments with high fiber proportions tend to embrittle the matrix and clog the nozzle (Saleh Alghamdi et al. 2021). Hence proportion of fibers in the composite is reduced to a maximum of 40% to have homogeneous dispersion and smooth processability. Such discontinuous fiber reinforced filament feedstock has proven to enhance the resulting mechanical, fatigue, corrosion, stiffness, and electrical properties of the printed samples (Dey et al. 2021). As the load is dispensed along the fiber length, continuous fibers have proven to enhance tensile properties compared to discontinuous fiber-filled composites. Continuous fiber reinforcement MEAM can be performed by either developing continuous fiber reinforced filament or co-extruding pure filament and continuous fiber simultaneously through two different nozzles (Tan et al. 2020). Tool paths have to be optimized to avoid cutting the continuous fiber reinforced filaments while printing intricate shapes or at the end of printing without affecting the property of the final prints. Furthermore, the surface-treated continuous fibers are observed to give properties better than untreated fibers (Saleh Alghamdi et al. 2021). Liu et al. 2019 reported that PA6 composites reinforced with continuous Kevlar fiber and 0.1 wt.% graphene nanoplatelets exhibited 1600% and 680% enhancement in tensile strength and modulus respectively as compared to printed pure PA6 ().

Ceramic and metal powder filaments are relatively newer feedstock for FFF based on MEAM process. Such filaments are extruded by mixing various proportions of powders and binders. The developed filaments are extruded through the heated nozzle to fabricate green parts. This is followed by subsequent debinding and sintering to produce the final parts. Low working temperatures, affordability, and simple operations are some of the key benefits of using metallic/ceramic filament feedstock with the FFF

technique. Iron, bronze, titanium alloy, 316 stainless steel, glass, zirconia and alumina are some newly developed metallic/ceramic filament feedstock (Liu et al. 2019, Nurhudan et al. 2021).

1.6 Limitations of FFF process

Affordability and diverse material options to cater to different applications are the prime reasons for the success of the FFF process. Like other processes, the filament-based FFF process also suffers limitations in terms of accuracy, printing speed, and material feed rate. The smallest layer thickness possible in printing is 78 μm , which limits the feature size and accuracy (Schirmeister et al. 2019). Precision nozzles with smaller diameters can be used to print such minute features but at relatively longer printing times. All the commercial printers are fitted with nozzles having a circular cross-section, which can only produce curvatures, but not sharp corners. The radius of curvatures have been observed to be equivalent to the radius of the nozzle (Tan et al. 2020).

Feed rate determines the maximum printing speed of the FFF systems. The combined effect of the ability to supply feedstock and the rate at which the feedstock gets melted and deposited determines the feed rate (Spoerk et al. 2018). Any modifications in the printer head to accommodate higher material feed rate will result in increased weight of the printer head. This will restrict the speed of the printer head. This can be countered by finding ways to reduce the friction generated from the increased weight of the printer head. Also, filaments should accommodate such higher material feed rate without slipping or breaking at the printer head (Singh et al. 2020).

Identifying suitable printing substrates is another challenge when printing newly developed materials (Schirmeister et al. 2019). The developed feedstock should possess affinity towards the printing substrate in order to adhere efficiently while printing and to detach effortlessly after printing. Generally, thin sheets, plates, and adhesives are developed using base polymers with similar or different polarities to serve the purpose (Spoerk et al. 2017).

Qualities such as manufacturing flexibility, low-volume custom-made products on demand, and efficient manufacturing make AM technology a vital enabler of Industry 4.0 (Nurhudan et al. 2021). Even though several feedstock are sold as proprietary products by the original equipment manufacturers, research is actively ongoing to develop novel feedstock to fabricate implants and smart structures. The filament feedstock for the FFF process is being developed to enhance biological, optical, mechanical, thermal, electrical, and magnetic properties. The performance of the final component and the repeatability of the FFF process significantly relies on the processability of the developed filament feedstock.

The present study aims to develop HDPE composites reinforced with BAG as filament feedstock for orthopedic application using fused filament fabrication process. Such feedstock with enhanced biological properties can be used developed patient-specific implants that mimic structural and mechanical behaviour of human bones.

1.7 Literature Review

An extensive amount of work has been carried out on the development of feedstock for FFF technique to cater to different applications. As demonstrated by researchers, only thermoplastics and their composites can be used as filament feedstock (Vaes and Van Puyvelde 2021). The nature of the reinforcement may vary from particulates, fibers or polymer blends to address the demands (Tan et al. 2020). The properties of the resulting composites highly rely on the manufacturing process parameters (Spoerk et al. 2019). Hence it is imperative to identify the influencing extrusion and printing parameters and their respective significance on the performance of newly developed filament feedstock and respective printed samples. Numerous investigations on various aspects of filament extrusion, FFF, and biomedical application of BAG and HDPE have been published in recent years and are tabulated into the following categories:

1. Filament feedstock extrusion of thermoplastics and its composites.
2. 3D printing of thermoplastics and its composites.
3. Biomedical applications of BAG.
4. Biomedical applications of HDPE and its composites.

Table 1.1. Literature survey on filament feedstock extrusion of thermoplastics and its composites.

Author and Year	Extrusion parameter	Material	Properties investigated	Remarks
Morales et al. 2021	Screw speed, barrel, and die temperatures.	Recycled PP/rice husk composites.	Density, water absorption and swelling diameter.	<ul style="list-style-type: none"> • Density decreases with filler addition. • With the increase in hydrophilic filler content, the water absorption and swelling diameter of the filaments are increased drastically. • Crystallization temperature and crystallinity increase with filler proportions.
Beesetty et al. 2020	Screw speed, barrel, and die temperatures.	HDPE/nanoclay composites.	Tensile, thermal, and melt properties.	<ul style="list-style-type: none"> • Tensile modulus and strength increase with filler addition. • Crystallinity and crystallization temperature increase with an increase in filler proportion. • The melt flow index decreases with an increase in filler content.
Patil et al. 2019	Screw speed, barrel, and die temperatures.	HDPE/cenosphere composites.	Tensile, thermal, and rheological properties.	<ul style="list-style-type: none"> • Tensile modulus and void content increase with filler addition. • Tensile strength and crystallinity decreased with an increase in filler proportion.

				<ul style="list-style-type: none"> • Complex viscosity increases with filler addition leading to dimensionally stable printed samples.
Spoerk et al. 2019	Barrel and die temperatures.	PP/mineral-filled composites.	Tensile and rheological properties, ovality and multiple extrusions.	<ul style="list-style-type: none"> • Tensile strength and complex viscosity remain comparable until 14 cycles of extrusions and then decrease drastically. • The Ovality of the filaments is suggested to remain less than 50 μm for ideal printing. • Filaments extruded after 14 cycles show higher ovality leading to oozing, overhangs, and warpage in the final prints.
Spoerk et al. 2018	Barrel and die temperatures, diameter and length of the die.	PP/CF composites.	Tensile property, rheology.	<ul style="list-style-type: none"> • Yield stress and Young's modulus increase with fibre content. • Yield strain decreases with an increase in fibre content. • Viscosity increases with fibre content leading to smaller diameter variation.
Singh et al. 2018	Melting temperature, and Die diameter.	HDPE and HDPE/Cenosphere composites.	Density and Tensile property.	<ul style="list-style-type: none"> • The density of composite filaments increases with an increase in extrusion passes.

				<ul style="list-style-type: none"> • Tensile modulus and yield strength increase with extrusion passes. • HDPE filament during tensile testing shows ductile behaviour with necking and plastic deformation. • Composite filaments show brittle behaviour without any visible sign of necking.
Wang et al. 2016	Barrel temperature, Screw speed and weight percentage of CNT.	PLA/CNT.	Filler dispersion, thermal and tensile properties.	<ul style="list-style-type: none"> • For the same temperature and speed levels, the distribution and dispersion of CNTs are better for lower concentrations. • Viscosity increases with CNT addition resulting in agglomeration. • Tensile property exhibits an increase of 37.83% at 3% filler and starts decreasing as filler percentage increases because of agglomeration of CNTs. • Crystallinity increases with CNT addition, while the thermal stability of the composites is good as neat PLA counterparts.
Singh et al. 2016	Barrel temperature,	ABS.	Diameter variation,	<ul style="list-style-type: none"> • Tensile strength increases with an increase in barrel temperature and screw speed.

	Screw and Take-off speeds.		Tensile property.	<ul style="list-style-type: none"> • Diameter deviation increases with an increase in screw speed because of inconsistent inflow at the exit. • Barrel temperature has a negligible effect on diameter deviation.
Boparai et al. 2016	Melt flow index, screw speed, barrel and die temperatures.	Nylon/Al-Al ₂ O ₃ composites.	Tensile property.	<ul style="list-style-type: none"> • Filaments are extruded in-house with properties such as melt flow index and tensile strength, the same as commercially available filaments. • Suggests usage of proprietary 3D Printer hardware or software with the developed filaments. • Tensile strength of the filaments decreases with the addition of filler.
Lee et al. 2014	Barrel temperature, compression ratio, length of the feeding and metering zone.	PMMA.	Viscosity, Melt pressure, and temperature.	<ul style="list-style-type: none"> • Length of the feeding and melting zone determines the complete melting and stability of the molten material. • Screw speed influences the melt temperature at the end of the screw.

				<ul style="list-style-type: none"> • Compression ratio and length of the feeding zone control the complete melting of the incoming material.
Chen et al. 2008	Barrel temperature, extrusion pressure and Screw speed.	HDPE/UHMWPE composites.	Tensile properties.	<ul style="list-style-type: none"> • Tensile strength is improved by the increase in extrusion pressure. • The optimum die temperature is found to be in the narrow range around melting temperature (~127 °C) with a window of 10 °C.
da Costa et al. 2007	Barrel temperature and Screw speed.	PP.	Thermal properties, Mechanical properties.	<ul style="list-style-type: none"> • Crystallinity increases with an increase in die temperature and extrusion cycles. • Melting temperature, tensile, and impact properties decrease with increased extrusion cycles. • Break stress, strain, and energy to break are reduced significantly with extrusion cycles.

Table 1.2. Literature survey on 3D printing of thermoplastics and its composites.

Author and Year	Print Parameters	Materials Used	Properties Investigated	Remarks
Palacios-Ibáñez et al. 2022	T_p , LT , T_b , and printing speed.	ASA/PEEK composites.	Tensile and thermal properties.	<ul style="list-style-type: none"> • PEEK is dispersed in the ASA matrix. • Young's modulus, strength and yield strain increase with PEEK addition. • Crystallization temperature and crystallinity increase with filler addition. • Thermal stability of the composites is as good as neat ASA samples.
Elhattab et al. 2021	T_e , T_b , printing speed and infill density.	PLA/AMP	Thermal, tensile, rheological and biological properties.	<ul style="list-style-type: none"> • Crystallinity decreases with filler addition. However, it is recrystallized to higher crystallinity after incubating in PBS. • Tensile strength and Young's modulus decreased with filler addition and decreased further after incubating in PBS. • Viscoelastic modulus and complex viscosity of composites are lower than neat PLA.

				<ul style="list-style-type: none"> • Printed scaffolds are dimensionally stable as the loss modulus is higher than the storage modulus. • Filler addition leads to higher degradation, significantly enhancing cell proliferation and pre-osteoblast cell attachment.
Bakır et al. 2021	LT, printing speed, T_p and T_b .	PET.	Tensile properties.	<ul style="list-style-type: none"> • Increase in T_p increases tensile strength by two-fold. • Parallel rasters exhibit more than 200% elongation, while perpendicular rasters exhibit elongation of less than 10%. • Because of insufficient fusion, samples printed in vertical orientation show lower strength compared to horizontal orientation samples.
Yeo et al. 2021	T_p , T_b and print speed.	PGA/HAp composites.	Compression, degradability and biological studies.	<ul style="list-style-type: none"> • Compression strength increases with HAp content up to 12.5 wt.% and starts decreasing. • Biodegradability of the composites is directly proportional to HAp proportions and is observed to increase with HAp additions.

				<ul style="list-style-type: none"> • Composites exhibit remarkable osteoblast proliferation. • <i>In vivo</i> animal studies reveal that the composites show superior bone regeneration and excellent mineral density.
Pan et al. 2021	T _p , T _b , LT, and printing speed.	PPS/CNT composites.	Thermal, wear, tensile and flexural properties.	<ul style="list-style-type: none"> • Tensile and bending properties of the composites are improved by 26 and 29% compared to neat PPS samples. • Crystallinity of the composites is improved by CNT addition. • Wear rate of 0.7 wt.% composites is reduced by 73.49% compared to neat PSS samples.
Kim et al. 2021	T _p , T _b , LT, infill density and printing speed.	PCL/HAp composites.	Tensile and electrical properties.	<ul style="list-style-type: none"> • Dielectric constant increases with filler addition. • Tensile strength and fracture strain decrease with filler addition. • Maximum dimensional error of the printed samples is 0.54 mm, which is acceptable for scaffold fabrication.

Schirmeister et al. 2021	T_p , and printing speed.	HDPE and HDPE/UHMWPE composites.	Crystal morphology, tensile and impact properties.	<ul style="list-style-type: none"> • 3D printed samples show 1D nanostructure in extended chain forms (shish-kebab formation) are formed in situ as a reinforcing phase. • Injection and compression moulded all HDPE samples show isotropically oriented crystals. • 3D printed composites show oriented UHMWPE in print direction. • Different processing conditions do not affect the crystallinity of all HDPE and HDPE/UHMWPE samples. • Printing speed of 150 mm/s and nozzle temperature of 210 °C gives maximum tensile and impact properties. • 3D printed samples exhibit properties comparable to injection and compression-moulded counterparts.
Rodzeń et al. 2021	LT, T_p , T_b , printing speed, T_e ,	PEEK/HAp composites.	Thermal, tensile, flexural and DMA properties.	<ul style="list-style-type: none"> • Tensile and flexural modulus increases with filler addition. • Crystallinity decreases with filler proportions.

	and raster angle.			<ul style="list-style-type: none"> • Storage modulus increases with filler content while the damping factor decreases. • Crystal grain size increases with filler proportions till 10 wt.% and starts decreasing.
Beatrice et al. 2021	T_p and printing speed.	PCL/TCP composites.	Chromatography, thermal, rheological and compression properties.	<ul style="list-style-type: none"> • Average molecular weight and on-set degradation temperature decrease with filler addition. • Crystallinity, melting, and crystallization temperature decreases with an increase in filler content. • Complex viscosity increase with filler proportion. • Compressive modulus increases with filler addition. • Pore size decreases with an increase in filler content.
Bragaglia et al. 2021	T_p and T_b .	PA6/BN composites.	Tensile and thermal conductivity.	<ul style="list-style-type: none"> • Density, void content, and viscosity increase with filler addition. • Thermal stability of the composites increases with filler proportion.

				<ul style="list-style-type: none"> • Tensile strength and elongation at break decreased with an increase in filler. • Elastic modulus, thermal conductivity and diffusivity increase with filler proportion.
Mahesh et al. 2021	T _b , LT, material flow rate, printing speed, and T _p .	PETG/OMMT nanoclay composites.	Tensile, flexural, compression, and impact properties.	<ul style="list-style-type: none"> • Density increases with an increase in nano clay proportion. • Tensile, flexural and compression strength increase with nano clay content to 5 wt.% and decreases. • Similarly, tensile, flexural and compression modulus and impact energy increase up to 5 wt.% of nano clay and decrease.
Nabipour et al. 2020	T _p , T _b , nozzle diameter and print speed.	PE/Cu composites.	Flexural and electrical properties.	<ul style="list-style-type: none"> • A thin sheet of polyethylene is chosen as substrate material. • Flexural strength and modulus increase with filler addition. • The specific resistance of the composites decreases with filler addition leading to increased conductivity.

Petersmann et al. 2020	T _p , and printing speed.	PP.	Crystal morphology.	<ul style="list-style-type: none"> • At 250 °C nozzle temperature and 2.25 mm/s print speed, strongly fused weld lines are formed, resulting in homogeneous crystal morphology. The resulting samples are isotropic. • Non-homogeneous morphology is developed because of poor weld lines resulting from the 200 °C nozzle temperature and 22.5 mm/s. The resulting samples are anisotropic. • Alternating structures of large and small spherulites are formed at 250 °C and 22.5 mm/s. This is analogous to the printing suggested by slicing software when large or multiple components are printed. • Crystal morphology is highly dependent on print temperature and speed, which determines the mechanical properties of the resulting semicrystalline samples.
Schirmeister et al. 2019	Nozzle diameter and	HDPE.	Build plate adhesion, tensile properties,	<ul style="list-style-type: none"> • Adhesion and shrinkage issue of printing HDPE is eliminated by using SEBS plates.

	T_p , T_b , LT , and printing speed.		surface quality and anisotropy.	<ul style="list-style-type: none"> • Tensile strength and stiffness of the samples printed using 0.4 and 0.8 mm nozzle diameter is comparable with the injection-moulded counterparts. • Elongation at break of the samples depends on print orientation. • Increasing printing speed from 25 to 150 mm/s does not affect the mechanical properties. • Mechanical properties are not influenced by 0° and 90° print direction. • Parts printed at optimised condition shows zero degrees of anisotropy, and micrography shows features analogous to injection moulded samples. • Surface quality of the parts is affected when printing at a higher speed.
Spoerk et al. 2018	T_p , T_e , T_b , printing speed, and flow rate.	PP/glass spheres composites.	Thermal, tensile, impact and warpage.	<ul style="list-style-type: none"> • Polypropylene plates with slightly different polarity are used as substrates. • All the samples are printed at elevated chamber temperature to control warpage.

				<ul style="list-style-type: none"> • Composites show increased crystallinity and crystallization temperature with the addition of filler. • Different filler sizes do not alter the crystallinity, crystallization melting and temperatures of the composites. • Young's modulus and yield strength of the composites are lower than the neat PP samples. • Notched impact energy decreased by 70-90% for the composites compared to neat PP samples. • Irrespective of the filler size and resulting crystallization temperature, all the composite samples tend to minimize warpage.
Singh et al. 2018	Infill (%), LT, Feed rate, Printing speed, T_p , T_b , and	HDPE/Cenosphere.	Density, and Tensile property.	<ul style="list-style-type: none"> • 3D printed HDPE has 19% lower density than its injection-moulded counterpart. • 3D printed HDPE-Cenosphere(40%) has 6 % lower density compared to its injection-moulded counterpart.

	Air cooling.			<ul style="list-style-type: none"> • Modulus of 3D printed HDPE is 16% more than the injection-moulded HPDE, and failure at 50% shows fibrous fracture. • Failure strain of 3d printed HDPE-cenosphere is 40% less than the filament counterpart, which reveals that the material had become brittle after 3D printing.
--	--------------	--	--	---

Table 1.3. Literature survey on biomedical applications of BAG.

Author and Year	Type of sample	Fabrication Process	Applications	Remarks
Zheng et al. 2021	PCL/Bioglass-nanoclay composites.	Foam replication and UV photo-polymerisation.	Endogenous bone regeneration.	<ul style="list-style-type: none"> • Developed interconnected microporous and macroporous scaffolds favour cell adhesion, proliferation and blood vessel formation. • <i>In vitro</i> bioactivity studies confirm the formation of the HAp layer on SBF immersed samples. • <i>In vitro</i> cell, studies show excellent adhesion, proliferation and polygonal morphology of cells.

				<ul style="list-style-type: none"> • The ADSC culture results show increased bone mineral density and bone tissue calcification from all samples. • Histological staining of scaffolds implanted into the cranial defect of rats shows cell penetration, tissue growth and new bone tissue formation.
Santos et al. 2021	PVA/Cu-BAG composites.	Tape casting.	Bioresorbable membrane for guided bone regeneration.	<ul style="list-style-type: none"> • Composite membrane shows excellent adhesion efficacy of MG-63 cells. • Degradation ratio decreases with the addition of BAG, which gives sufficient time to form new <i>in vivo</i> tissue. • Bioactivity assay shows the formation of the HAp layer on samples, and the amount of precipitation increases exponentially with time. • Presence of Cu increases the damage of bacteria membranes leading to its anti-bacterial effect.
Lacambra-Andreu et al. 2021	PLA/BAG composites.	Injection moulding.	Implants.	<ul style="list-style-type: none"> • Compression strength and modulus increase with BAG addition. • Storage modulus increases with BAG proportion. • <i>In vitro</i>, bioactivity studies show the formation of HAp on all composites.

				<ul style="list-style-type: none"> • Crystallinity induced by the thermal process reduces BAG solubility, leading to reduced bioactivity kinetics.
Distler et al. 2020	PLA/BAG composites.	MEAM.	Scaffolds.	<ul style="list-style-type: none"> • Compression strength and modulus decrease with BAG addition. • Bioactivity studies of the filament show the formation of the HAp layer after incubation in SBF for 28 days. • Though being hydrophobic, cell culture studies of the scaffolds show elongated fibroblastic morphology highlighting cytocompatibility. • Scaffolds show enhanced osteogenesis of ADSC <i>in vitro</i>.
Ghorbani et al. 2020	PCL/BAG composites.	Slurry-based 3DP.	Bioresorbable scaffolds.	<ul style="list-style-type: none"> • 3D printed scaffolds and their surfaces are modified with UV irradiation to improve the efficacy of bone regeneration. • Developed scaffolds show adequate cell adhesion, proliferation and osteogenesis. • Scaffolds are hydrophilic with interconnected pores and are observed to enhance capillary action, scaffold/cell interaction and tissue in-growth.

				<ul style="list-style-type: none"> • Degradation at the end of 5 weeks shows less than 50% degradation of scaffolds, which is essential to maintain a balance between regeneration and biodegradation.
Dutta et al. 2019	Magnesium/BAG composites.	Spark plasma sintering.	Bioresorbable implants.	<ul style="list-style-type: none"> • Vicker's hardness and elastic modulus increase with BAG addition. • Hydrogen evolution and corrosion rates of magnesium in composites are reduced by BAG addition. • Porosity of the samples after immersion is increased, leading to enhanced cell proliferation. • BAG addition increases hardness and modulus by 2.5 and 1.7 times, respectively. • Cytocompatibility results show sufficient cell viability of the composites.
Chalishgaonkar et al. 2018	BAG coating on Titanium.	LENS TM	Porous implants.	<ul style="list-style-type: none"> • MTT assay shows a high concentration of living cells on coated surfaces. • Coated samples exhibit enhanced cell proliferation and provide supportive habitat for cell attachment and growth. • Hardness and <i>in vitro</i> wear resistance are improved for coated samples.

Khan et al. 2016	BAG.	Cold isostatic pressing.	Rabbit porous femoral bone defect model.	<ul style="list-style-type: none"> • Samples exhibit accelerated early-stage bone formation at defect sites. • Samples display accelerated bone healing and better anchorage of bone implants. • Excellent vascularization is observed from the implants engulfed with mature bone tissue and blood vessels. • Collagenous microstructure and bony network are formed between the implanted samples and surrounding bones.
Yao et al. 2014	PCL/BAG-chitosan composites.	Foam replicator.	Osteochondral tissue engineering.	<ul style="list-style-type: none"> • Bioactivity studies after immersion in SBF solution for 3 days show deposition of HAp and carbonated HAp layers. • Cell culture studies on porous scaffolds show enhanced cell viability favouring infiltration and proliferation of cells into the internal porous region. • Cells are grouped and form a monolayer on the scaffold surface. • In vitro studies adequate cell adhesion, growth and proliferation.

Table 1.4. Literature survey on biomedical applications of HDPE and its composites

Author and Year	Constituents	Fabrication Process	Nature of implants	Remarks
Paxton et al. 2021	Porous HDPE.	Selective laser sintering.	Maxillofacial implants.	<ul style="list-style-type: none"> • Plasma-treated scaffolds result in 1.6 times higher cell proliferation than untreated porous scaffolds. • Rapid tissue integration and vascularization are higher in plasma-treated porous samples. • The highly deposited collagen matrix around the implant and fibrous capsule formation show the typical foreign body response.
Salem et al. 2021	Molybdenum disulphate, cuttlebone and red coral-based HDPE composites.	Hot pressing.	Artificial joints.	<ul style="list-style-type: none"> • Effects of hydrothermal ageing on tribological behaviour of the developed composites are studied. • Cuttle bone-based composites show enhanced frictional resistance after ageing. • Molybdenum disulphate and red coral-based composites exhibit a higher frictional coefficient than unaged samples. • Aged samples show accelerated wear rates because of the degradation of the matrix-filler interface.
Al-allaq et al. 2021	HDPE/HAp, HDPE/HAp-	Hot pressing.	Tissue engineering	<ul style="list-style-type: none"> • Degree of crystallinity increases with MWCNT addition (up to 2 wt.%).

	MWCNT composites.		for bone reconstruction.	<ul style="list-style-type: none"> • Vickers hardness increases with MWCNT addition (up to 2 wt.%). • 1 wt.% MWCNT composites show higher fracture strength.
Choi et al. 2017	Porous HDPE.	Moulding.	Mandibular implant.	<ul style="list-style-type: none"> • Mandibular implant removed from the patient after one year of service. • The outer surface of the implant is covered with fibrous connective tissue. • Compact fibrous tissue covers the inner side of the implants. • Implants do not show signs of chronic inflammation.
Fouad et al. 2013	HDPE/HAp composites.	Injection moulding.	Bone substitute.	<ul style="list-style-type: none"> • Fracture toughness of composite is less compared to neat samples. • Melting temperature and crystallinity decrease with HAp addition. • This is because of conglomerate formation or heating at a lower temperature. • Storage and loss modulus, hardness and wear resistance value increase with HAp addition.

				<ul style="list-style-type: none"> • Fracture toughness of composites decreases with the addition of HAp.
Suwanprateeb et al. 2012	Porous HDPE.	Binder printing.	Cranial implants.	<ul style="list-style-type: none"> • Porous HDPE samples are printed with 20, 30 and 40 % porosity and heat-treated via single and two-step processes. • Two-step heat-treated samples with 30% porosity show higher tensile modulus, strength, and elongation at break. • Cell viability of the 30% porous, two-step heated samples shows no toxicity and high cell viability.
Dong et al. 2011	HDPE/silane treated TiO ₂ composites.	Moulding and hot pressing.	Bone substitute.	<ul style="list-style-type: none"> • Fatigue tests are performed in dry and 0.9% NaCl saline solution. • Fatigue life of wet specimen is longer than dry specimen at a stress lower than 30 MPa. • Silane treatment enhances load-bearing and eliminates interfacial failure during flexural fatigue. • Effect of silane connection in silane-TiO₂/HDPE is similar to that of the acid phospho-protein bond.
Fouad and Elleithy 2011	HDPE/graphite nanocomposites.	Injection moulding.	Total hip joint replacement.	<ul style="list-style-type: none"> • HDPE and HDPE/Graphite samples exhibit no signs of cytotoxicity.

				<ul style="list-style-type: none"> • Crystallinity is observed maximum at 2% of graphite and starts decreasing with an increase in filler content due to restriction in mobility. • Yield strength, storage, loss and Young's modulus are directly proportional to filler content and increase with filler addition.
Deshpande and Munoli 2010	Porous HDPE.	Prefabricated Medpor [®] sheets.	Facial skeletal augmentation.	<ul style="list-style-type: none"> • HDPE implants provide adequate and stable augmentation of the desired contour while maintaining a natural appearance. • In the follow-up, one case of sub-clinical infection and three cases of implant deviation are observed out of 70 patients over an average period of 46.34 months
Wu et al. 2010	HDPE/PGA fibres.	Prefabricated Medpor [®] rod.	Cartilage support.	<ul style="list-style-type: none"> • Non-woven PGA fibre is wound around the rod and compressed by a mould into the required shape. • <i>In vitro</i> culture shows that the regenerated cartilage tissue grew into and around the HDPE core. • Cytocompatibility of the support is observed from the formation of chondrocytes into HDPE pores.

				<ul style="list-style-type: none"> • This enables the regeneration of cartilage in the required size and shape.
Mavrikakis et al. 2009	Porous HDPE.	Moulding.	Lower eyelid spacer.	<ul style="list-style-type: none"> • Implants show significant bio integration via fibrosis and vascularization.
Salmonia et al. 2007	Porous HDPE.	Selective laser sintering.	Drug delivery, tissue engineering scaffolds.	<ul style="list-style-type: none"> • Functionally graded porous samples are fabricated with powders of different size ranges. • Elastic modulus and ultimate tensile strength decrease with an increase in powder size. • Failure deformation increases with powder size.
Chowdhury et al. 2004	HDPE/CF and HDPE/Kevlar fiber.	Compression molding.	Acetabular cup.	<ul style="list-style-type: none"> • 10% Kevlar-filled HDPE composites show a lower wear rate than unfilled and filled HDPE samples. • Unfilled HDPE samples are hydrophobic, while composite samples are hydrophilic. • Hemocompatibility increases with the addition of fibres.

1.8 Summary of literature survey

Though numerous FFF composite filament feedstock based on established matrices are developed, research reporting the introduction of new material as filament feedstock is scarce. Also, feedstock development with biomedical properties to cater to on-demand orthopaedic needs is rising. Bioactive glass is known to possess exceptional biological properties. Hence the introduction of BAG reinforced composite filament feedstock for FFF process is worthy. Hence, the present study attempts to develop and characterize BAG reinforced HDPE filament feedstock for FFF printing technique for possible orthopaedic applications.

1.9 Motivation

Bioactive glass reacts with the physiological environment and readily undergoes osseointegration (bonding to existing bone) and osteoconduction (new bone growth on the surface). These are vital features for numerous biomedical applications. However, BAG's poor mechanical properties and innate brittleness restrict its utilization in rectifying bone defects due to trauma, tumor removal, and congenital anomalies. Combining bio-inert HDPE polymer and bioactive glass in the form of composites is a promising way of modulating the mechanical and biological properties of the individual constituents. Researchers have shown the merits of such hybridization resulting in bio-compatible polymer composites with the combined bioactivity of inorganic filler and structural integrity of polymer matrix.

A good number of research show that the most affordable way to develop intricate orthopaedic polymeric implants to rectify bone defects is the FFF based on MEAM processes. Researches also highlight fewer materials and corresponding composites are established as filament feedstock for FFF process. Further, limited researchers have successfully introduced new feedstock materials. The present study attempts to introduce new HDPE feedstock for the FFF process with biological capabilities to cater to orthopaedic needs. The motivation to pursue this study is outlined as follows:

- New feedstock material for FFF.
- Filament feedstock with the biomedical property.
- Tailorability to mimic bone properties.

- Patient-specific implants and scaffolds.
- Affordable cost and fabrication on-demand.
- Enabler of Industry 4.0 for orthopaedics.

The objectives are formulated and presented based on the aforementioned rationale in the following section.

1.10 Objectives and scope of the work

From the precedent literature survey, it is evident that the development of H/BAG composite filament feedstock for FFF process is scarce. Hence, the development of H/BAG composite feedstock and subsequent evaluation of its printability and mechanical behaviour of the printed samples are proposed in the present investigation. The proposed work pursues the following objectives:

- Preparations of H/BAG blend of different filler percentages using twin-screw melt compounder followed by micrographic analysis to ensure homogeneous blending.
- Development of neat H and H/BAG composite filament feedstock using a single screw extruder by optimizing extruder parameters.
- Characterization of filament feedstock for their physical (density, void content), thermochemical (DSC, TGA/DTG), spectroscopic (XRD), and mechanical properties (tensile).
- Optimization of print parameters for printing neat H and H/BAG filament feedstock.
- Investigate the effect of BAG addition on physical (density and void content), thermochemical (TGA/DTG and DSC), spectroscopic (XRD), thermophysical (CTE and MFI), and rheological properties of the printed samples.
- Investigation of the effect of BAG addition on mechanical (tensile, flexural, compression and impact) and the printed samples' thermomechanical (DMA) properties.
- Extensive micrography on filaments, printed and fractured samples for structure-property correlations.
- Fabricate representative implant models to showcase the printability of developed feedstock material.

The scope of the present work includes the melt compounding of BAG reinforced (5, 10, and 20 wt.%) HDPE composites and corresponding micrography analysis to evaluate the homogeneous distribution. Subsequently, neat HDPE and composite blends are extruded using optimized process parameters to obtain filament with the required diameter and rigidity, which can be effortlessly fed into the printer. The melt, thermal and mechanical properties of filaments are evaluated to correlate the effect of BAG addition and printability. Printer parameters are optimized, and samples are printed for subsequent evaluation of tensile, flexural, compression, impact, and dynamic mechanical properties. Property maps of selected properties are presented along with properties of bone for comparative analysis of the developed feedstock and available bio-composites. Simultaneously, representative implant models are printed to demonstrate the feasibility of the developed feedstock to fabricate complex and intricated biological models.

1.11 Outline of the thesis

The meticulous research performed in regards to the defined objectives is presented in the thesis. The concise framework of the thesis is as follows:

Chapter 1 presents details of additive manufacturing and its types, polymer-based AM processes, composite feedstock development for FFF process, and its limitations. This chapter also furnishes an extensive literature survey on filament extrusion, printability and properties of polymer composites, and biomedical applications of the constituents, followed by the objectives.

Chapter 2 concentrates on the constituents used to develop filament feedstock and various processing routes such as melt compounding, filament extrusion, and printing of the developed feedstock. The various techniques used to analyze printability, mechanical behaviour, and microstructural features of the filament feedstock and printed samples are described in detail.

Chapter 3 focuses on the characterization of the melt blends and filament feedstock. Investigation of the filaments' physical, thermal and mechanical properties are present, along with microstructural analysis of filler distribution.

Chapter 4 illustrates the printability of the developed filament feedstock. The relationship between influencing process parameters and the quality of the final part is presented. Process parameter optimization to eliminate print-induced defects is described in detail.

Chapter 5 presents the tensile properties of the printed samples. The deformation mechanism from stress-strain curves and microstructural analysis is illustrated in detail.

Chapter 6 analyses the flexural properties of the printed samples. The structural deformation and nature of load transmission are analyzed from microstructural analysis and are described in detail.

Chapter 7 focuses on the compression behaviour of the printed samples. The deformation features are analyzed using micrography, after which the deformation mechanism is formulated and illustrated in detail.

Chapter 8 presents the impact behaviour of the printed samples. The dissipation of applied energy is studied from micrography and is explained in detail.

Chapter 9 concentrates on the viscoelastic behaviour of the printed samples. The effect of BAG addition and temperature variation on damping ability is reported in detail.

Chapter 10 emphasizes the comprehensive conclusions interpreted from the results present in the thesis, followed by the future scope of work.

2 MATERIALS AND METHODS

2.1 Constituents

The current study uses BAG filler and HDPE matrix to prepare biocompatible thermoplastic feedstock for FFF process. The specifics of the constituents are provided as follows.

2.1.1 Bioactive glass

The conventional glass melting process is used to synthesize BAG, and the composition is as follows 57SiO₂-10Na₂O-22CaO-6P₂O₅-2TiO₃-3B₂O₃ (wt.%). The synthesized BAG is a derivative of traditionally synthesized 45S5[®] bioglass (45SiO₂-25.4CaO-24.5Na₂O-6P₂O₅) with additives to improve the bioactivity (Khatua et al. 2018). TiO₃ enhances antibacterial properties and bone healing ability and is biologically attractive as it regenerates tissue response (Riaz et al. 2016). B₂O₃, on the other hand, plays a significant role in bone physiology, wound healing, and increased extracellular matrix (Yang et al. 2012). The raw materials used for the synthesis are chemically pure (99%) silicon dioxide (SiO₂, Merck), calcium oxide (CaCO₃, Sigma Aldrich), sodium carbonate (Na₂CO₃, Merck), phosphorus pentoxide ((NH₄)₂HPO₄, Merck), titanium dioxide (TiO₂, Merck), and borax (Na₂B₄O₇·10H₂O, Merck). The batches are weighed and homogeneously mixed with the help of agate mortar and a pestle, followed by melting in a platinum crucible for an hour at 1450 °C. The melt is quenched in water and dried at 100 °C, followed by ball milling using zirconia balls and ethanol as the medium for 24 hours (Figure 2.1a, b). Sympatec high-speed image analysis system (QICPIC, USA) estimates particle size. BAG particles are separated by the transportation fluid (water), and image analysis is carried out. The mean particle size of the ball-milled BAG particles is found to be 3.02 μm (Figure 2.1c).

2.1.2 HDPE

Granular HDPE (HG) of grade 180M50 is acquired from Indian Oil Corporation Ltd, Mumbai, India is used as the matrix material. The average size of the granular resin is 3 mm (Figure 2.1d) with a molecular weight of 97,500 g/mol. The properties of the thermoplastic matrix used are listed in Table 2.1.

Table 2.1. Properties of HDPE grade 180M50 used in the present investigation.

Properties	Test method	Value	Unit
Melt flow index (190°C & 2.16 kg)	ASTM D1238	20	gm/10 min
Density @ 23°C	ASTM D1505	0.950	gm/cm ³
Tensile yield strength	ASTM D638	22	MPa
Elongation at yield	ASTM D638	12	%
Flexural modulus	ASTM D790	750	MPa
Hardness	ASTM D2240	55	Shore D
Vicat softening point	ASTM D1525	124	°C

* As specified by the supplier

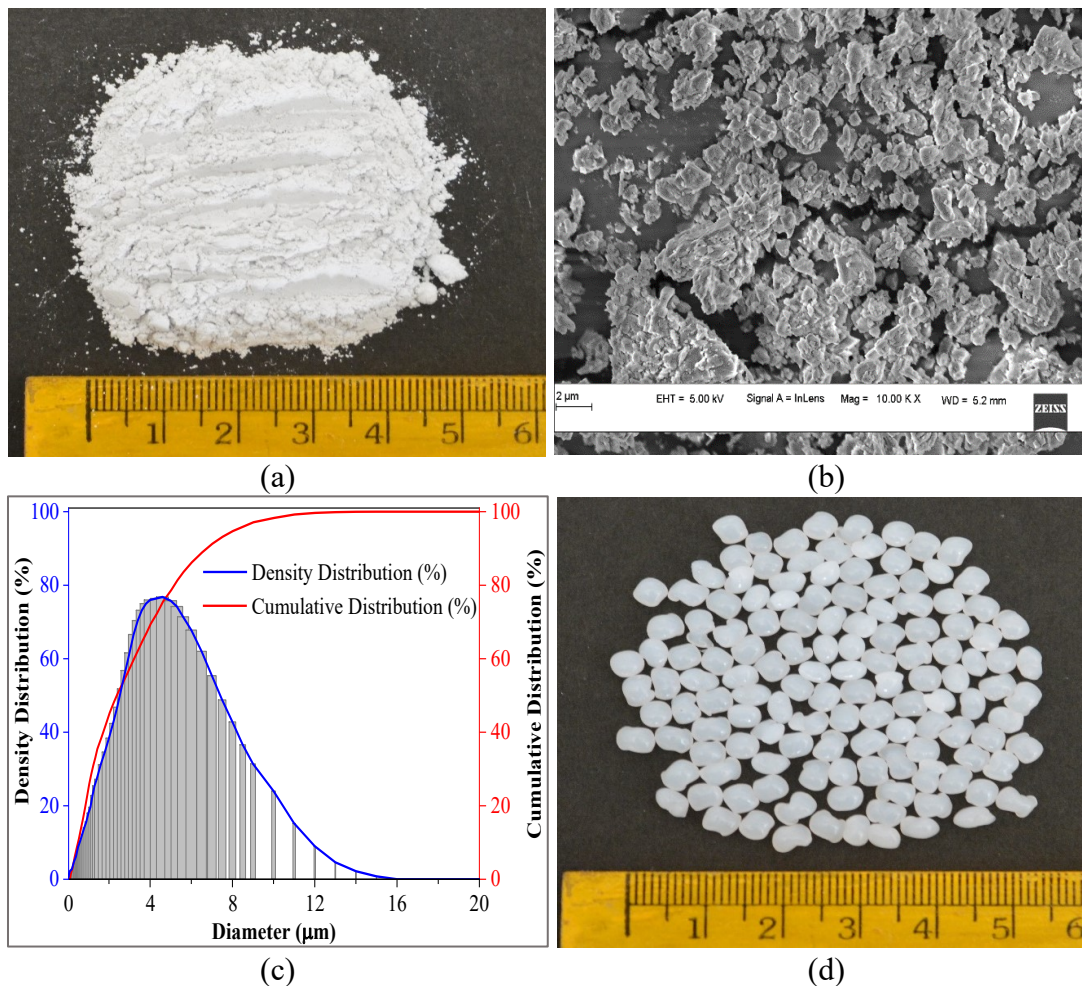


Figure 2.1. Representative images of (a) Ball milled, (b) micrographic morphology and (c) particle distribution of BAG and (d) Granular HDPE used in the present investigation.

2.2 Thermogravimetric analysis (TGA)

Thermal stability and degradation temperature of the composites are determined using a thermogravimetric analyzer (TGA 4000, PerkinElmer, USA) (Figure 2.2). The degradation of the polymer composites at elevated temperatures is accompanied by weight loss due to molecular chain deterioration. Thermogravimetry (TG) and derived TG (DTG) curves give char residue (%), onset degradation temperature (T_{d5} - the temperature at which 5% degradation occurs), and maximum degradation temperature (T_{dmax}). The analysis is carried out over the temperature range of 0 - 600 °C at the rate of 20 °C/min using dry nitrogen (30 ml/min) and a sample weight of 10 mg. The degradation temperature from TGA is essential to determine the processing temperatures for melt compounding of blends, filament extrusion, and sample printing. A minimum of three samples are tested, and average values with standard deviation are reported.



Figure 2.2. Thermogravimetric analyser (TGA 4000, PerkinElmer, USA).

2.3 Differential scanning calorimetry (DSC)

The thermal behaviour of filament and printed samples are analyzed using a differential scanning calorimeter (DSC 6000, PerkinElmer, USA) (Figure 2.3) under fixed nitrogen gas flow of 30 ml/min. A small sample weighing approximately 10 mg is taken in an aluminum crucible, and the test is performed in two thermal cycles. The first cycle is carried over a range of 0 – 200 °C at the rate of 10 °C/min. Then the sample is held at 200 °C for 2 min, followed by cooling at a rate of 10 °C/min. The Second heating is performed over the same temperature range. The first heating cycle removes solvents

and thermal history from earlier processes. Parameters such as crystallization temperature (T_c), melting temperature (T_m), and enthalpy of melt (ΔH_f) are calculated as per ASTM D3418-15. % X_c can be calculated using the equation:

$$X_c = \frac{\Delta H_f}{\Delta H_f^* \times wt.} \times 100 \% \quad (2.1)$$

Where *wt.* and ΔH_f^* denote the weight percentage of H in the H/BAG composites and the melting enthalpy of 100% crystalline HDPE (293 J g^{-1}), respectively (Khalifa et al. 2022).



Figure 2.3. Differential scanning calorimeter (DSC 6000, PerkinElmer, USA).

2.4 Melt compounding and filament extrusion

Melt compounding is generally used for preparing particulate reinforced thermoplastic composites. The constituents are fed through a gravity feeder into the electrically heated barrel of the melt compounder. The thermoplastic polymer is melted by the combined action of the heated barrel and friction generated from the molten melt due to the rotation of the Archimedean screw within the barrel. Melt compounding of BAG and HDPE is executed using a co-rotating twin-screw extruder as shown in Figure 2.4a (Haake Rheomex PTW 16 OS, Thermo Fisher Scientific, Germany) to develop composite blends to develop filament feedstock. Before melt compounding, BAG and HDPE are kept in a vacuum oven at 100 and 80 °C, respectively, for 24 hours to remove residual moisture, if any. A screw speed of 100 rpm and temperature profile of 130 - 180 °C in increments of 10 °C across six heating zones are used to get continuous composite strands. A 2 m long water bath maintained at 25 °C is used to quench the strands of 5, 10, and 20 weight fractions of BAG in HDPE (H). These weight fractions will henceforth be denoted as H_5 , H_{10} , and H_{20} , respectively. Before filament extrusion,

composite strands are pelletized (Figure 2.4b) and dried at 80 °C for 24 hours to remove residual moisture, if any.

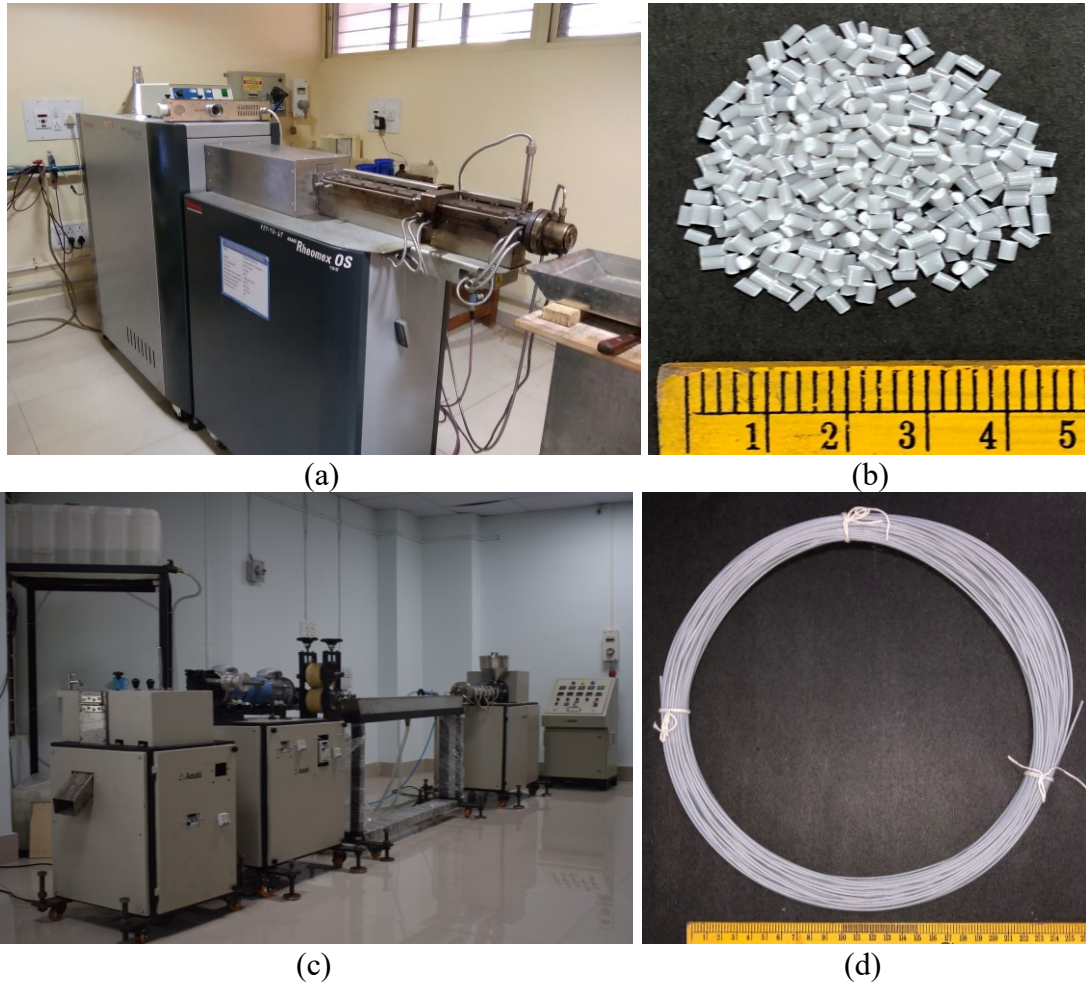


Figure 2.4. Melt compounder (Haake Rheomex PTW 16 OS, Thermo Fisher Scientific, Germany), (b) H₂O melt blend, (c) single-screw extruder (25SS/MF/26, Aasabi Machinery Pvt Ltd, India) and (d) H₂O filament feedstock.

Neat H and H/BAG composite filaments are extruded using a single screw extruder (25SS/MF/26, Aasabi Machinery Pvt Ltd, India), as shown in Figure 2.4c. The mechanism of the melt formation is the same as that of the twin-screw melt compounder, except for uniform melt output. This favours the cross-section of the composite filament feedstock to be uniform which is crucial for FFF. Extrusion is carried out at an optimized screw speed of 15 rpm and temperature profile of 140-150-160-145 °C. A 1.5 m long water bath maintained at 25 °C is used to quench the filaments. Filaments with a consistent diameter of 1.75 ± 0.05 mm are obtained by appropriate adjustment of take-off speed (Figure 2.4d).

2.5 X-ray diffraction (XRD)

X-ray diffraction (Empyrean 3rd Gen, Malvern PANalytical, Netherlands) (Figure 2.5) is performed to analyze the effect of amorphous BG filler on the semi-crystalline HDPE matrix. The analysis is carried out at 2 °/min in 2 θ range of 10° - 80° using a Cu- α radiation source ($\lambda=1.5406\text{\AA}$) at a voltage of 40 kV and a tube current of 15 mA with a Nickel filter. % Crystallinity ($\%X_c$) of specimen is calculated using the following equation:

$$\%X_c = \frac{I_c}{I_c + I_a} \quad (2.2)$$

Where I_c and I_a are the integral intensities of the peaks corresponding to crystalline and amorphous phases, respectively (Khalifa et al. 2022). A minimum of three samples are tested, and average values are reported.

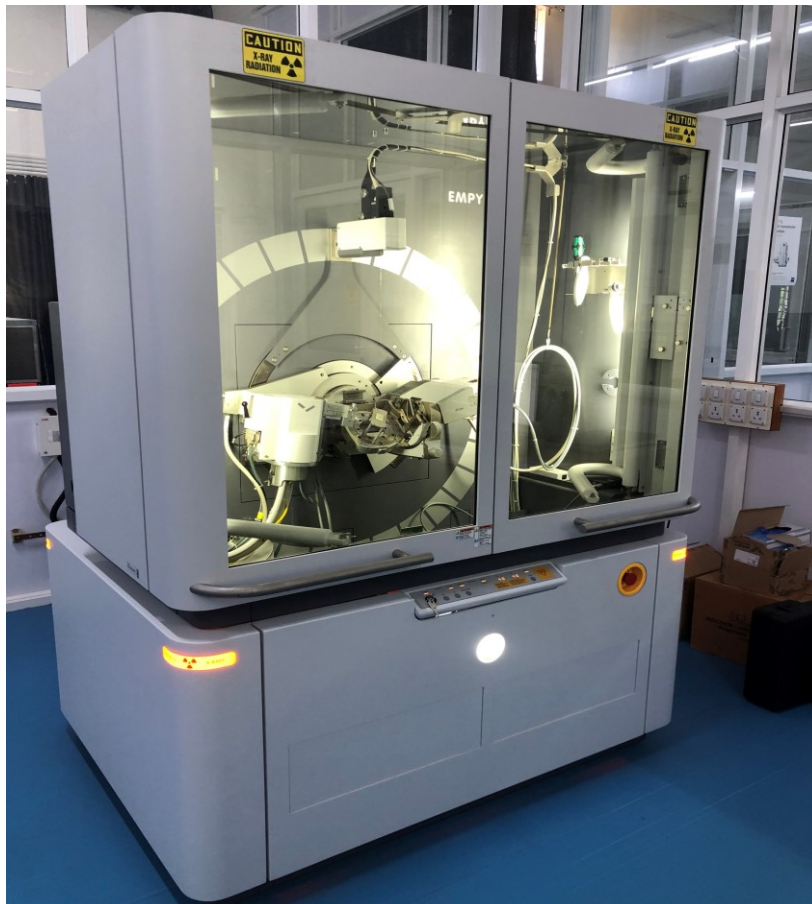


Figure 2.5. X-ray diffractometer (Empyrean 3rd Gen, Malvern PANalytical, Netherlands).

2.6 Rheology

The rheological behaviour of the development composites plays a vital role in predicting and controlling the FFF process. Rheological properties are studied using a rotational rheometer (Anton Paar Rheometer, MCR 502, Austria) in parallel plate configuration, as shown in Figure 2.6. A frequency sweep of 0.01 – 100 Hz in oscillatory mode is carried out at 240 °C (T_p) and 1 % strain rate, respectively, as per ASTM D4440-15. A minimum of five samples of each composition are tested, and average values are reported.



Figure 2.6. Rheometer (Anton Paar Rheometer, MCR 502, Austria).

2.7 Density measurement

The density (ρ) of the filament feedstock and printed parts are measured as per ASTM D792-13 using a density measurement kit, as shown in Figure 2.7. Five samples are examined per composition, and the mean values with standard deviations are reported as experimental density (ρ_e). Using the rule of mixtures, the theoretical density (ρ_t) of the composites is estimated as follows:

$$\rho_t = \rho_m V_m + \rho_f V_f \quad (2.3)$$

where V is the volume fraction and the subscripts m , and f denote the matrix and filler, respectively. The density of neat HDPE and BAG are taken as $0.950 \pm 0.006 \text{ g/cm}^3$ (Jayavardhan and Doddamani 2018) and $2.428 \pm 0.003 \text{ g/cm}^3$ (Khatua et al. 2018),

respectively, which are used in computing ρ_t . Furthermore, using ρ_e and ρ_t , the porosity content (φ_v) in filaments and printed samples are calculated using the following equation:

$$\varphi_v = \frac{\rho_t - \rho_e}{\rho_t} \quad (2.4)$$

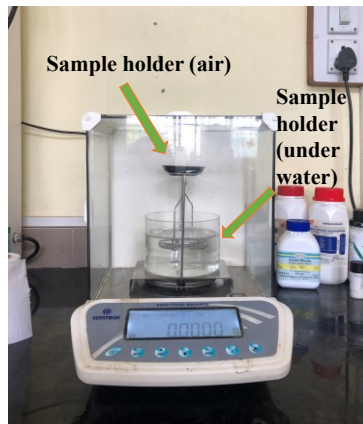


Figure 2.7. Density measurement kit.

2.8 Build plate adhesive preparation

50 g of Styrene-ethylene-butylene-styrene (SEBS) (TAIPOL SEBS 6150) is dissolved in 300 ml of xylene in a closed glass container. A vortex mixer (Fisher Scientific, Germany) is used to dissolve SEBS fully in the solution. Samples are printed over Kapton tape applied with SEBS adhesives glued over the heated glass plate, with an infill of 100% to achieve dense, defect-free prints.

2.9 FFF of developed feedstock

Neat H and H/BAG composites are additively manufactured using a commercial dual extruder printer (Protocentre 999, AHA 3D, India). The printer (Figure 2.8) utilizes a ϕ 0.4 mm brass nozzle, and the tool path is generated using Simplify 3D software for printing. Printability of the developed feedstock is evaluated by varying LT (350 and 150 μ m), T_p (200 and 240 $^{\circ}$ C), T_b (ambient and 110 $^{\circ}$ C), and T_e (ambient and 70 $^{\circ}$ C). T_e is restricted to a maximum value of 70 $^{\circ}$ C to prevent printer hardware failure. Expanded polystyrene sheets are used as insulation to withstand elevated temperatures. All the samples are printed with two outer perimeters without any support structures. Printing temperatures and flow rates are set to achieve fully dense parts with an infill

of 100%. The printing parameters used in the present investigation are listed in Table 2.2 . Post printing, samples are allowed to cool down to ambient temperature inside the printing chamber and stored under standardized conditions ASTM D618-13 for subsequent characterization. Unless otherwise stated, parameters in Table 2.2 are used for printing samples for various characterizations.



Figure 2.8. FFF based 3D printer (Protocentre 999, AHA 3D, Jaipur, India).

Table 2.2. FFF parameters used in the present investigation.

Parameters	Values
T_p (°C)	240
T_b (°C)	110
T_e (°C)	70
Multiplier	1 – H, H ₅ ; 1.05 – H ₁₀ ; 1.1 – H ₂₀
LT (mm)	0.150
Printing speed (mm/s)	35
Infill (%)	100
Infill pattern	Rectilinear ($\pm 45^\circ$)
Orientation	Flatwise, along the x-axis

2.10 Coefficient of thermal expansion (CTE)

The coefficient of thermal expansion of the prints is essential in understanding the dimensional stability of the printed samples. CTE gives the measure of polymerization-

induced shrinkage and resulting warpage concerning the BAG content of the developed composites. CTE of the prints is measured using a push-rod dilatometer (CIPET-Chennai) as per ASTM E228-17. Test temperature is varied between 30 – 90 °C, and corresponding linear expansion is measured. A minimum of five samples of dimensions $75 \times 12.7 \times 3$ mm of each composition are tested, and average values are reported.

2.11 Warpage analysis

Printed neat H and H/BAG composites undergo warpage due to volumetric shrinkage, affecting the dimensional stability of the resulting prints. (Schirmeister et al. 2021, Spoerk et al. 2017). Warpage samples are printed per the dimension in Figure 2.9a and stored at 23 (C, 50% relative humidity for 72 hours post crystallization. As warping tends to tilt the prints from their printing position once removed from the print bed, all the samples are scanned upside-down. Excess materials resulting from nozzle oozing are removed prior to warpage analysis. All the samples are sprayed with zinc to make the surface reflective and scanned by a portable hand-held 3D scanner (Artec 3D Space Spider, USA), as shown in Figure 2.9b. The obtained 3D point cloud data from the 3D scanner is processed to represent the 2D actual shape of the prints and are compared with the geometry in the CAD file using CloudCompare version 2.12.

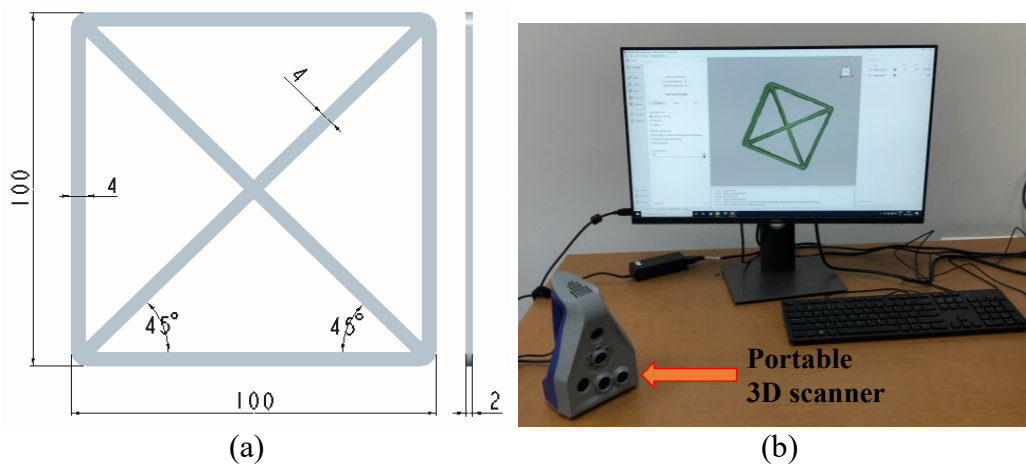


Figure 2.9. (a) CAD model of warpage sample (All dimensions are in mm) and (b) Hand-held 3D scanner (Artec 3D Space Spider, USA).

2.12 Melt flow index (MFI)

MFI of the neat H and H/BAG composites are measured using Zwick Roell Mflow, USA (Figure 2.10) as per ASTM D1238-13. MFI is used to understand the flowability and viscosity of the developed composites concerning the filler content. This aids in selecting appropriate flow parameters for printing. MFI is measured at the temperature of 190°C and a load of 2.16 kg. A minimum of five samples are tested, and average values are reported.



Figure 2.10. Melt flow index (MFI) apparatus (Zwick Roell Mflow, USA).

2.13 Tensile test

Filaments and printed samples are subjected to tensile tests to understand the influence of BAG addition on the mechanical properties of H/BAG composites. Filaments with an overall length of 176 mm and a distance between the grips of 76 mm are used for tensile testing at 5 mm/min crosshead speed. A 20 kN loadcell capacity Zwick universal testing machine (Zwick Roell Z020, USA) and the strain is captured using an extensometer of gauge length 50 mm (Figure 2.11a). Printed samples as per ASTM D638-14 are also tested at identical crosshead speed and strain is captured using an extensometer of gauge length of 25 mm (Figure 2.11b). A minimum of five samples are tested, and average values are reported with standard deviation.

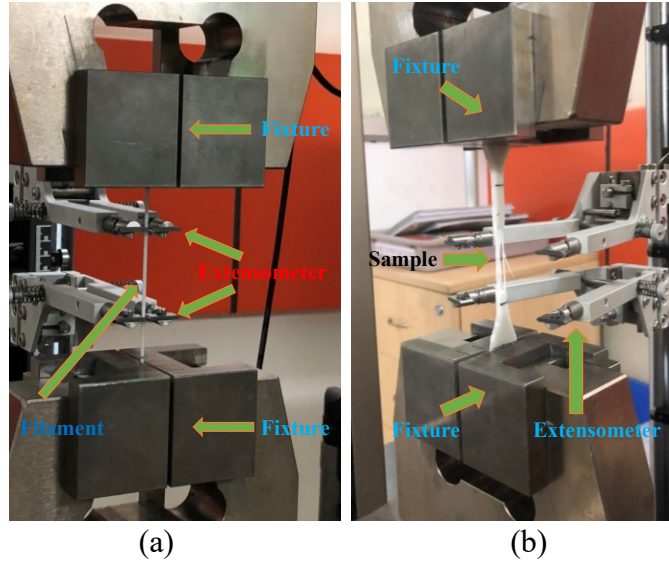


Figure 2.11. Tensile test on (a) filament feedstock and (b) printed tensile specimen with an extensometer attachment.

2.14 Flexural test

Printed samples of dimension $127 \times 12.7 \times 3.2$ mm are subjected to three-point bending based flexural tests as per ASTM D790-17. A 20 kN loadcell capacity Zwick universal testing machine (Zwick Roell Z020, USA) with a preload of 0.1 MPa and a displacement rate of 1.54 mm/min is used to carry out the tests as shown in Figure 2.12. The span length to thickness ratio is maintained at 16:1. The tests are carried out until the rupture of the sample or a maximum strain of 10%, whichever is earlier. A minimum of five samples are tested, and average values are reported with standard deviation. The flexural modulus is estimated using

$$E_{fM} = \frac{L^3 m}{4bd^3} \quad (2.5)$$

where L is the support span (mm), b is the width of the beam (mm), d is the thickness of the beam, and m is the slope of the tangent to the initial linear portion of the load-deflection curve. The flexural stress is calculated using

$$\sigma_{fS} = \frac{3PL}{2bd^2} \quad (2.6)$$

where P is the load (N) at a given point on the load-deflection curve (Bharath Kumar et al. 2016, Patil et al. 2019).

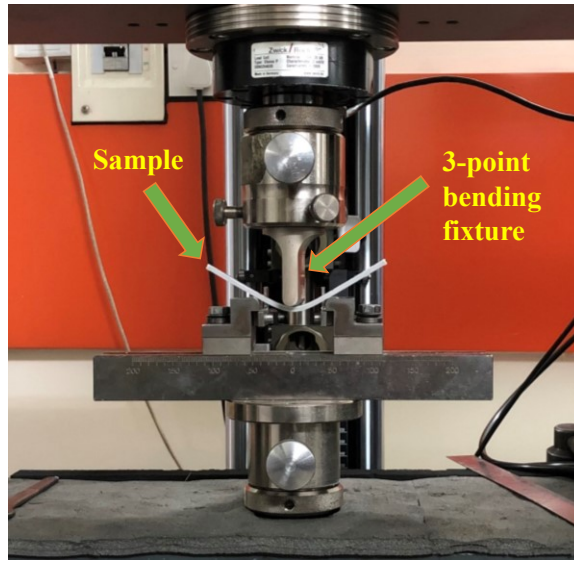


Figure 2.12. Flexural test using 3-point bending configuration.

2.15 Compression test

Compression tests (ASTM D695-15) are carried out on cylindrical samples with \varnothing 12.7 mm and 25.4 mm height at static (strain rate of 1.3 mm/min) and quasi-static (strain rate of 0.001, 0.01 and 0.1 s^{-1} corresponding to cross head movement of 0.001, 0.01 and 0.1 mm/min) conditions. The test is terminated at a maximum load of 20 kN, and the yield strength is calculated at a 0.2% offset method. Analytical methods are also used to determine the yield strength and modulus of the samples (Jayavardhan and Doddamani 2018). A 20 kN loadcell capacity Zwick universal testing machine (Zwick Roell Z020, USA) is used to carry out the compression tests, as shown in Figure 2.13. Compressive stress is the peak stress at the end of the initial linear elastic region, and energy absorption is calculated using the following formula (Swetha and Kumar 2011)

$$\text{energy absorption} = \int_0^{\varepsilon_{40}} \sigma d\varepsilon \quad (2.7)$$

Where ε_{40} is the strain at 40%, and σ is the stress. A minimum of 5 samples are examined, and the mean values with standard deviation are reported.

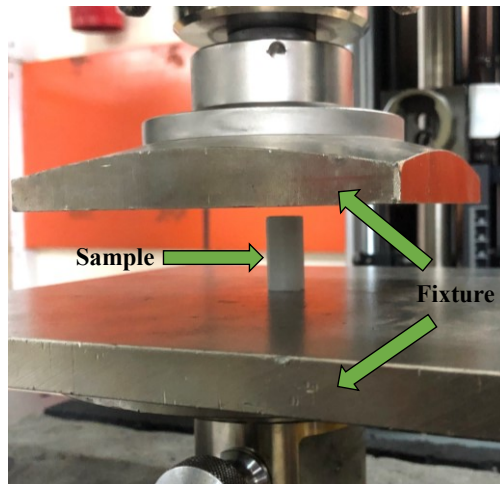


Figure 2.13. Compression test setup.

2.16 Impact

Notched Charpy impact test is carried out (ZWICK ROELL HIT50P, USA) as per ASTM D6110-18. Printed samples of dimension $127 \times 12.7 \times 3 \text{ mm}^3$ are notched to 2.5 mm depth, 45° and 0.25 mm tip radius, and subsequently tested in edgewise direction with a 1 J hammer as shown in Figure 2.14. A minimum of five samples are tested in each composition, and the average value is reported herein.

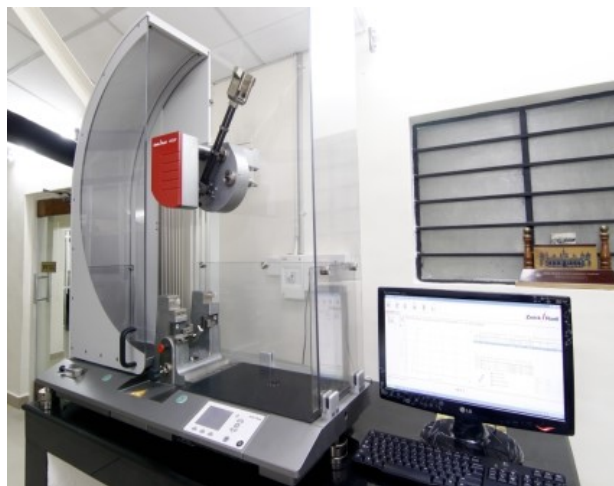


Figure 2.14. Impact test apparatus (ZWICK ROELL HIT50P, USA).

2.17 Dynamic mechanical analysis (DMA)

Dynamic mechanical analysis of printed neat H and H/BAG composites is performed using the DMA apparatus (Netzsch DMA 242 E Artemis, Germany), as shown in Figure 2.15a. Specimen of dimension $50 \times 12 \times 2 \text{ mm}$ as per ASTM D5023-15 is used for the

analysis. Temperature sweep is performed in a three-point bending configuration as shown in Figure 2.15b with the span length of 40 mm. The test is performed for the temperature range of 28 – 120 °C at the frequency of 1 and 10 Hz with a deformation amplitude of 25 μm . The analysis is terminated at a temperature of 120 °C to avoid the melting of the samples. Performance of composites in terms of BAG addition is evaluated using the mechanical parameters like storage modulus (E'), loss modulus (E''), and damping factor ($\tan\delta$). A minimum of five samples are tested, and average values with standard deviation are reported.



Figure 2.15. (a) Dynamic mechanical analyser apparatus and (b) 3-point bending configuration.

2.18 Scanning electron microscopy

Microstructure analysis is carried out by field emission scanning electron microscopy (FESEM) (CARL ZEISS, FESEM, Germany) (Figure 2.16a) and optical microscopy (OM) (Zeiss, Germany) (Figure 2.16b). The samples for FESEM analysis are sputter-coated with gold to improve conductivity.



(a)

(b)

Figure 2.16. (a) Field emission scanning electron microscope (CARL ZEISS, FESEM, Germany) and (b) optical microscope (Zeiss, Germany).

3 COMPOSITE BLENDS AND FILAMENT FEEDSTOCK CHARACTERIZATION

Composite blends obtained from melt compounding are examined using the micrography technique to analyze the dispersion of BAG in HDPE matrix. Similarly, extruded filaments are initially subjected to measurements of diameter, density, and void content. Furthermore, tensile characteristics of the extruded filament are studied to understand printability. Micrography and corresponding elemental mapping are also carried out on the filaments. The results are discussed herein.

3.1 Melt characterization

3.1.1 Micrography of composite blends

Blend obtained from melt compounding forms the vital component for developing effective H/BAG feedstock composites. The melt compounding aims to disperse the BAG filler homogeneously in the HDPE matrix without agglomeration by applying higher shear force and temperature (Abeykoon et al. 2016, da Costa et al. 2007). Process parameters such as barrel and die temperatures and screw speed are selected to yield a premium quality blend with homogeneous BAG dispersion. Micrographic analyses are carried out on the obtained blends to ensure the proper dispersion of BAG in the HDPE matrix. Elemental mapping is carried out for the element silica (Si), which is the prime constituent of BAG. Figure 3.1a, c, e show lower magnification micrography of H₅, H₁₀ and H₂₀ blends, and corresponding elemental mapping are displayed in Figure 3.1b, d, f. Elemental mapping confirms the homogeneous distribution of BAG in the HDPE matrix with no visible aggregates. This clearly indicates exerting sufficiently higher shear force during the melt compounding process. Higher magnification micrography of H₅, H₁₀, and H₂₀ blends (Figure 3.2a, b, c) shows the homogeneous dispersion and poor interface between BAG and HDPE matrix. The obtained H/BAG composite blends are extruded into feedstock filament for subsequent material extrusion additive manufacturing.

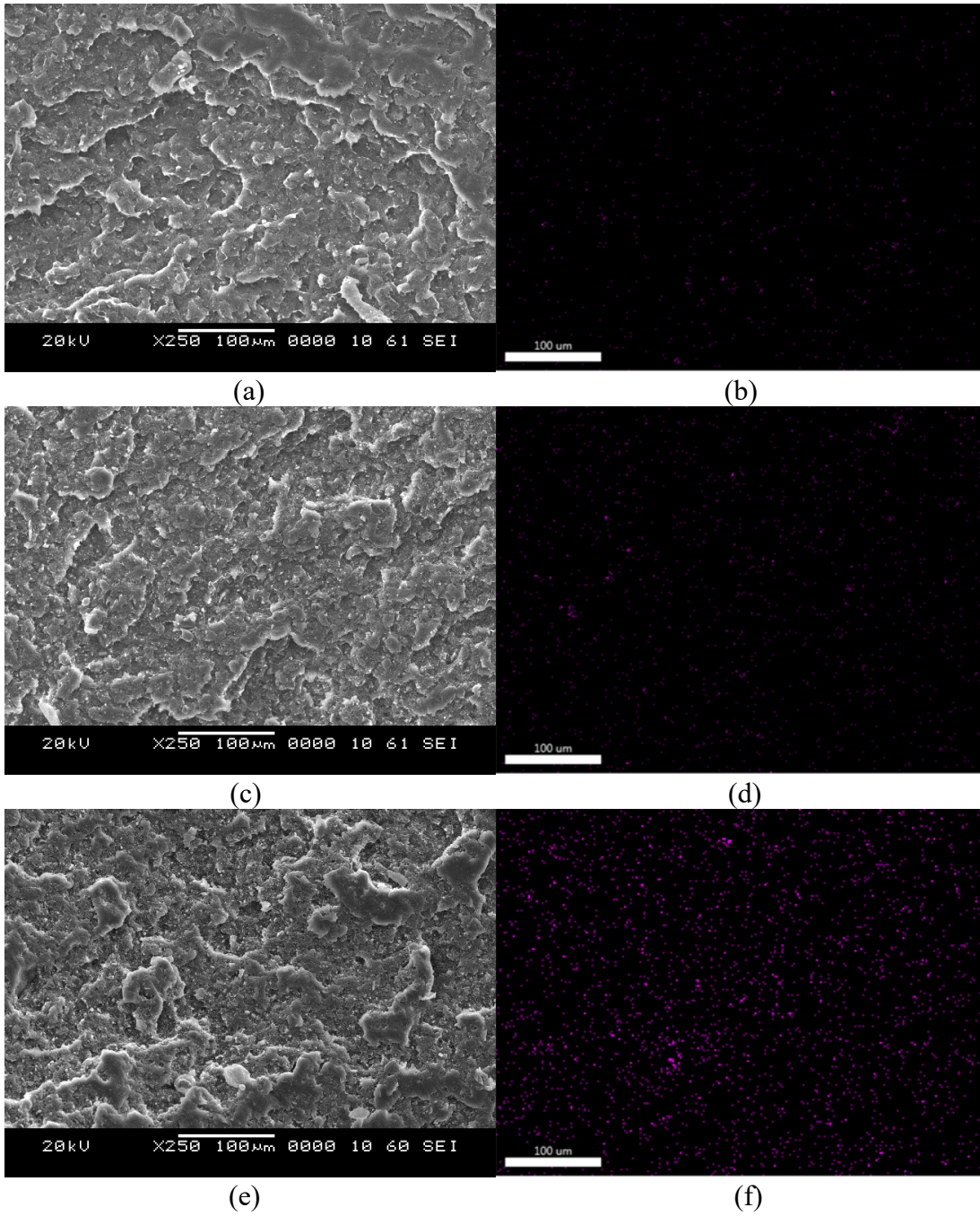


Figure 3.1. BAG distribution (a), (c) and (e) and corresponding elemental mapping (b), (d), and (f) of respective H₅, H₁₀, and H₂₀ blends.

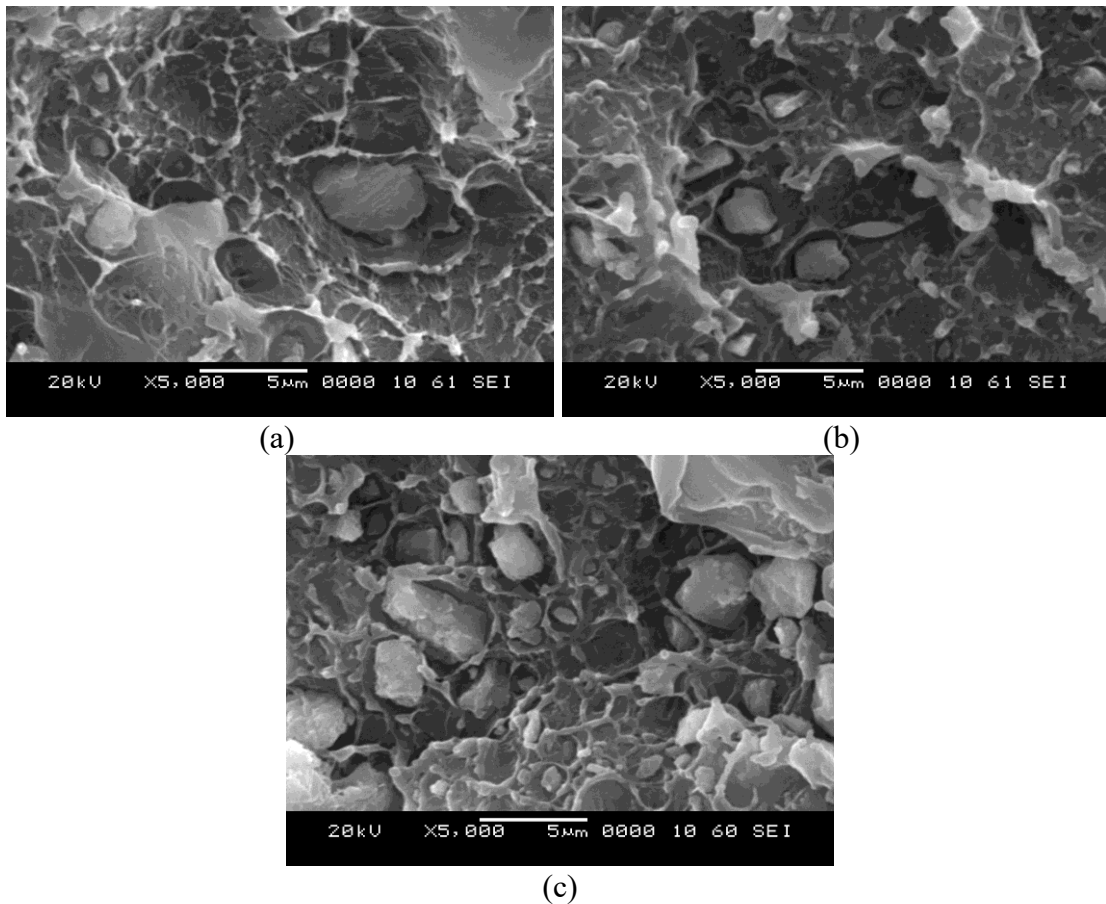


Figure 3.2. BAG distribution and HDPE-BAG interface of (a) H₅, (b) H₁₀ and (c) H₂₀ blends in higher magnification.

3.2 Filament characterization

The diameter of the extruded filaments is measured using a digital vernier calliper. The diameter of the developed filament feedstock is well within the acceptable limit (Singh et al. 2020) of 1.75 ± 0.05 mm, as shown in Figure 3.3a. The pressure variation due to the different sizes and shapes of the BAG leads to wider diameter distribution of H/BAG composites compared to neat H filaments (Singh et al. 2020). Nevertheless, all the developed filament feedstock are found to be perfectly printable.

3.2.1 Density and void content of filament feedstock

Developed neat HDPE and composite filaments are tested for their density and void content and are listed in Table 3.1. The density of the composite is directly proportional to the wt.% of each component (Jayavardhan and Doddamani 2018). The addition of BAG linearly increases the density of the composites. H₂₀ shows an increment of 13.8%

in density compared to neat H filament. The mean particle size of BAG is $3.02 \mu\text{m}$ (Figure 2.1c), and the particles are irregular in shape (Figure 2.1b). Such BAG powder is expected to constrain HDPE matrix chains across BAG particles and increase viscosity (Doddamani 2020). The linear increase in porosity of the developed filaments may be due to the viscosity-induced restricted flowability and non-vacuum-assisted extrusion (Singh et al. 2020, Singh et al. 2020). Neat HDPE filament shows negligible void content owing to the absence of filler, while H₂₀ shows a maximum porosity of 13.31% (Table 3.1).

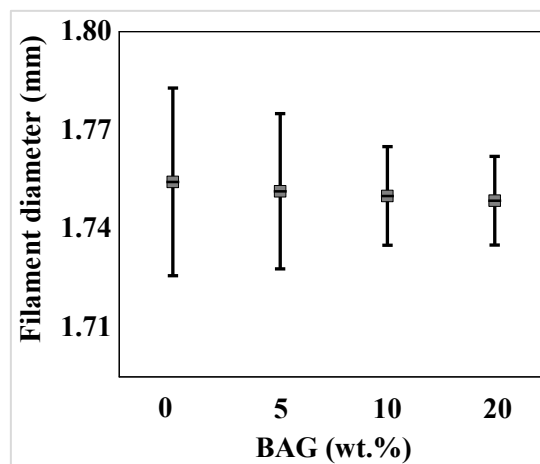


Figure 3.3. Diameter of the extruded filament feedstock.

Table 3.1. Density and void content of the developed filament feedstock.

Sample	Theoretical density (kg/m ³)	Experimental density (kg/m ³)	Void content (%)
H	950	949.22 ± 23.73	0.08
H ₅	1023.92	985.25 ± 24.63	3.78
H ₁₀	1097.84	1019.25 ± 25.48	7.16
H ₂₀	1245.68	1079.84 ± 26.98	13.31

3.2.2 Thermal properties of extruded filaments

Thermal degradation of H_G and filament feedstock are estimated by thermogravimetric analysis. The thermogravimetry (TG) curve, as shown in Figure 3.4a, highlights the single-stage degradation of the filament feedstock in the temperature range of 450 – 500 °C. This corresponds to the structural decomposition of HDPE matrix. Onset degradation temperature (T_{d5}), maximum degradation temperature (T_{dmax}), and char

residue are studied as a relative measure of thermal stability of the H/BAG composites. First derivative TG (DTG), as shown in Figure 3.4b, helps to determine T_{d5} and T_{dmax} . The onset degradation temperature and maximum degradation temperature of H_G are found to be 457.86 ± 1.12 and 479.84 ± 1.57 °C, respectively (Table 3.2). This helps in deciding the processing temperatures to obtain composite blends, extruded filaments, and printed samples without any degradation of the constituents. In addition, the crystallization temperature of BAG is around 600 °C (Khatua et al. 2018), which is very well higher than the maximum degradation temperature (~ 490 °C). This indicates that the BAG filler used in the present work will retain its inherent characteristics during various stages of subsequent thermal processes (melt compounding, filament extrusion, and 3DP).

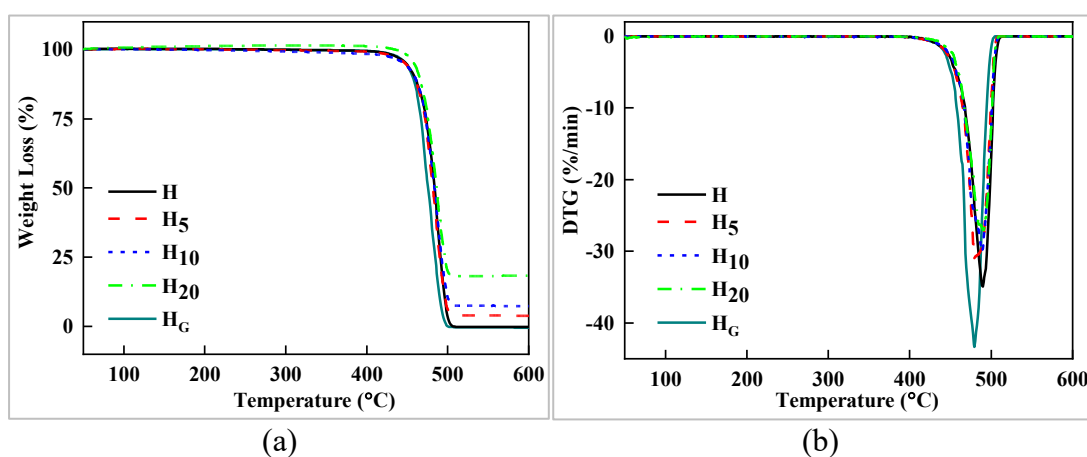


Figure 3.4. Representative (a) TGA and (b) DTG of H_G and filament feedstock.

From Table 3.2, it is evident that the addition of BAG results in a marginal improvement in the thermal stability of the filament feedstock when compared to H_G . Both, T_{d5} and T_{dmax} of the filaments increased marginally compared to HDPE granules. However, with the addition of BAG, there are no significant changes in the thermal stability of the composite feedstock. This behaviour indicates that the thermal stability of the H/BAG composites is as good as the neat H samples. Char residue at complete decomposition (600 °C) indicates the relative measure of the BAG present in the composites. The residual weight of HDPE granule and neat H filament at the end of 600 °C is zero, suggesting the complete decomposition. The BAG based composites

have a proper residual weight corresponding to loaded BAG in HDPE matrix (Table 3.2). Maximum degradation rate at T_{dmax} decreases with BAG addition. This behaviour may be associated with the fact that HDPE is the only constituent undergoing thermal decomposition and the proportion of HDPE decreases with BAG addition (Lu et al. 2016, Samsudin et al. 2016). Both melt compounding and filament extrusion is carried out in the temperature ranges (140~180 °C) lesser than T_{d5} of H_G , resulting in thermally stable composite blends and filament feedstock.

Table 3.2. Thermal degradation properties of H_G and filament feedstock.

Sample	T_{d5} (°C)	T_{dmax} (°C)	Residue (%)	Maximum degradation rate (%/mm)
H_G	457.86 ± 1.12	479.84 ± 1.57	-	44.22 ± 0.79
H	466.77 ± 1.24	491.54 ± 1.94	-	34.91 ± 0.58
H_5	463.59 ± 1.15	490.38 ± 1.83	4.11 ± 0.07	31.34 ± 0.49
H_{10}	466.36 ± 1.18	490.78 ± 2.26	8.21 ± 0.14	29.41 ± 0.50
H_{20}	465.16 ± 0.98	492.40 ± 1.87	18.29 ± 0.31	27.84 ± 0.51

Figure 3.5a, b, show heating and cooling curves obtained from DSC analysis for H_G and filament feedstock. All the samples show well-defined crystallization and melting peaks observed in range of 100 - 115 and 120 - 135 °C, respectively. T_m of H_G is found to be 128.53 ± 1.59 °C (Figure 3.4d). This emphasizes the need for a processing temperature greater than T_m . The neat H and its composites processed at temperatures greater than T_m are found to achieve enhanced shear mixing (composite blending) and better mouldability (filament extrusion and printing) (Patil et al. 2019). Hence, the temperatures of subsequent melt blending, filament extrusion, and sample printing processes are higher than the obtained T_m of H_G . The crystallinity of H_G is estimated as a baseline characteristic for evaluating the effect of BAG addition on crystallinity. From cooling curves (Figure 3.5a), T_c and crystallinity of H_G are found to be 106.45 °C and $50.11 \pm 0.78\%$. T_c , T_m , and $\%X_c$ of H_G and filament feedstock are tabulated in Table 3.3. T_m of the filament feedstock determined from melting curves (Figure 3.5b) is found

to be unaffected by the addition of BAG. This indicates that the addition of BAG does not influence the melting behaviour of the composites.

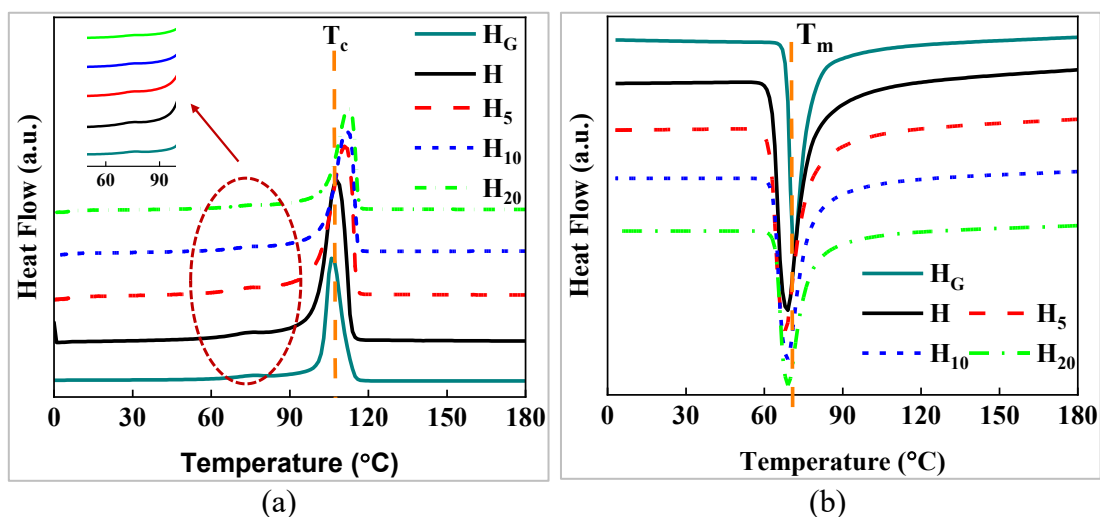


Figure 3.5. Representative (a) cooling (in-sets showing cold-crystallization phenomenon) and (b) heating curves of H_G and filament feedstock.

Table 3.3. Thermal properties and crystallinity of H_G and filament feedstock.

Sample	T_c (°C)	T_m (°C)	% X_c	
			DSC	XRD
H_G	106.45 ± 1.70	128.53 ± 1.59	50.11 ± 11.78	49.61 ± 0.76
H	110.92 ± 1.48	131.29 ± 1.34	59.89 ± 0.93	57.85 ± 0.79
H_5	111.17 ± 1.24	132.09 ± 1.33	55.44 ± 0.81	54.02 ± 0.83
H_{10}	112.07 ± 1.33	131.21 ± 1.32	47.63 ± 0.78	46.81 ± 0.51
H_{20}	112.52 ± 1.33	130.82 ± 1.34	36.88 ± 0.59	35.24 ± 0.85

Furthermore, a small crystallization peak around 75 °C is observed from the crystallization curves (in-sets of Figure 3.5a). This phenomenon is called cold-crystallization, which highlights the side chain branching of a moderate portion of HDPE, which cannot cold-crystallize along the remaining portion at ~110 °C (Fonseca and Harrison 1998). The peak intensity decreases with the BAG addition, indicating the restricted HDPE chain mobility. In addition, filament feedstock shows a slight increase in T_c compared to H_G . This is due to the increased mobility and resulting re-alignment of HDPE chains during filament extrusion (Doddamani 2020). Neat H and H_5 feedstock stock filaments show higher crystallinity than H_G . % X_c of filaments decreases with BAG addition, and H_{20} filaments exhibit 38.43% lower crystallinity than neat H

filaments. This results in H/BAG composite filaments stiffer than the neat H filament. This increased stiffness due to BAG presence changes the composite behaviour from ductile to brittle. Such behaviour is essential for filament feedstock to resist forces developed during printing and retain the circular cross-section without buckling or fracture (Singh et al. 2016).

3.2.3 XRD analysis of extruded filaments

XRD is carried out to study the effect of BAG on HDPE matrix in terms of crystallinity. Figure 3.6a shows the XRD patterns of amorphous BAG and semi-crystalline H_G. Such amorphous BAG is known to dissolve in bodily fluid readily to form a hydroxy apatite layer, thereby increasing the bioactivity (Khatua et al. 2018). XRD patterns of the HDPE show characteristic peaks at the Bragg angle (2θ) of $\sim 21.46^\circ$, $\sim 24.62^\circ$ and $\sim 36.08^\circ$, corresponding to the orthorhombic phase of HDPE (110), (200), and (020) respectively (Butler et al. 1995, Doddamani 2020, Lin et al. 2015). On the other hand, bioglass shows a characteristic amorphous hump at a Bragg angle (2θ) of $\sim 30^\circ$ (Khatua et al. 2018). Compared with H_G, there is an enhancement in the crystallinity of the filaments H and H₅. This is due to the re-arrangement of the HDPE polymer chain upon combined heating and cooling processes of subsequent melt compounding and filament extrusion.

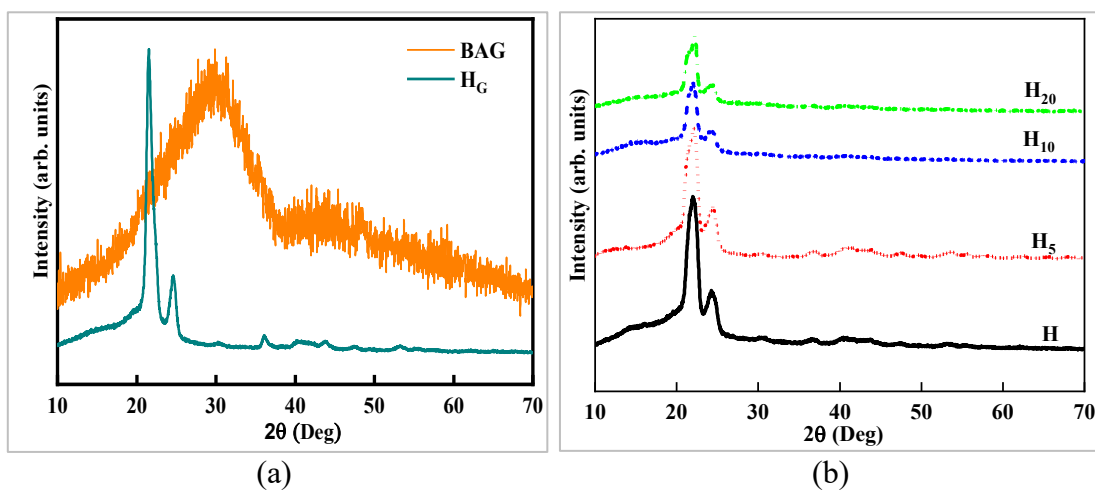


Figure 3.6. Representative XRD pattern of (a) BAG and H_G and (b) filament feedstock.

The crystallinity of the filament feedstock decreases with BAG addition. H₂₀ filaments exhibit 34.55% reduced crystallinity compared with neat H filaments. From Figure 3.6b, it is evident that the diffraction position of the HDPE does not shift with the addition of bioglass and the composites are semi-crystalline. Diffraction peaks of all composites are contributed by the matrix HDPE rather than amorphous BAG. The adverse effect on the crystallinity of the composites by the filler addition is underlined by the reduction in the diffraction peak intensity (Patil et al. 2019). The XRD results are summarized in Table 3.3. The percentage of crystallinity estimated from the XRD analysis agrees with the DSC results.

3.2.4 Tensile properties of filament feedstock

Filament feedstock must possess certain qualities that enable it to easily be used in 3D printing. The filament feedstock must retain the circular cross-section without buckling while the pinch rolls or pressurized drivers feed them into the nozzle. This can be ensured by making the filament feedstock stronger and stiffer. Stiffer filaments can resist the forces acting at the driver end to maintain the circular cross-section and resist the forces at the printer head end to avoid buckling and fracture (Singh et al. 2020, Vaes and Van Puyvelde 2021). Additionally, composite filaments are expected to be flexible enough to be spooled and stored. However, the addition of stiffer BAG is known to have an adverse effect on the ductility of the composite filaments. The tensile test on developed filaments reveals that neat H and H₅ exhibit elongation more significant than 500%. However, increasing the BAG concentration beyond 5 wt.% reduced the fracture strain by less than 250% (Table 3.4). Therefore, for better clarity, the stress-strain data up to 100% is presented in Figure 3.7a. The developed composite filaments are circular in cross-section (Figure 3.7b) and are flexible enough to be spooled effortlessly (Figure 3.7d), and they are found to endure forces exerted at the printer head. Consequently, the filaments during printing resist buckling or fracture while retaining the circular cross-section. The increase in turbidity of H/BAG composite filaments with BAG addition is shown in Figure 3.7e.

Table 3.4. Tensile properties of filament feedstock.

Sample	Modulus (MPa)	UTS (MPa)	Elongation at UTS (%)	Fracture strength (MPa)	Fracture strain (%)
H	623.36 ±11.53	16.25 ±0.41	18.7 ±0.49	-----	-----
H ₅	721.54 ±18.45	15.43 ±0.36	9.3 ±0.27	-----	-----
H ₁₀	926.44 ±24.91	14.06 ±0.39	7.9 ±0.12	11.2 ±0.29	239.2 ±6.28
H ₂₀	973.13 ±24.99	13.82 ±0.31	7.3 ±0.19	5.43 ±0.15	246 ±6.37

3.2.5 Micrography of filament feedstock

The extruded filaments are cold mounted in epoxy and fine polished Figure 3.7b. From the micrographs (Figure 3.8a, c, e) and corresponding elemental mapping of silica (Si) (Figure 3.8b, d, f), it is evident that the BAG fillers are dispersed in the HDPE matrix homogeneously without any agglomeration. Due to the second cycle of melting and shearing during the extrusion process, the degree of dispersion is higher for filaments when compared with their blend counterparts. Furthermore, the uniform distribution of BAG aids in improving the mechanical properties of the developed feedstock composites. This results in a linear increase in the modulus of the composite filament. H₂₀ samples show a 1.56 times higher modulus than neat H filaments (Table 3.4). The addition of BAG restricts the HDPE chain mobility; hence, the ultimate tensile strength (UTS) and elongation at UTS decrease linearly with BAG addition. H₂₀ exhibits 14.95 % and 60.91% reduction in UTS and elongation at UTS compared to neat HDPE filament (Table 3.4).

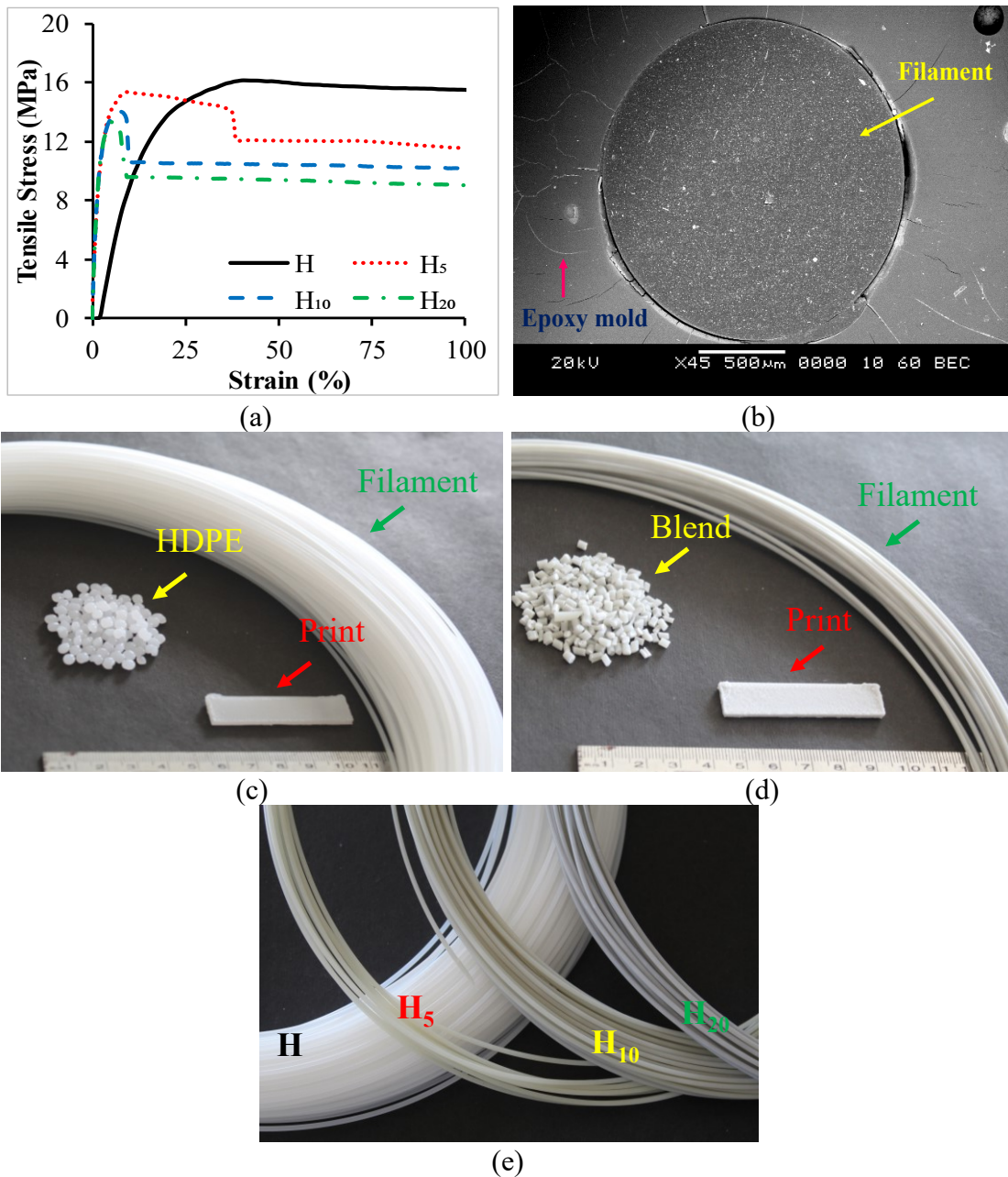


Figure 3.7. (a) Tensile response of the developed neat H and H/BAG composite feedstock and (b) circular cross-section of the extruded filaments. Representative feedstock, filaments and print of (c) H, (d) H₂₀ composites and (e) show an increase in turbidity of filaments with BAG addition.

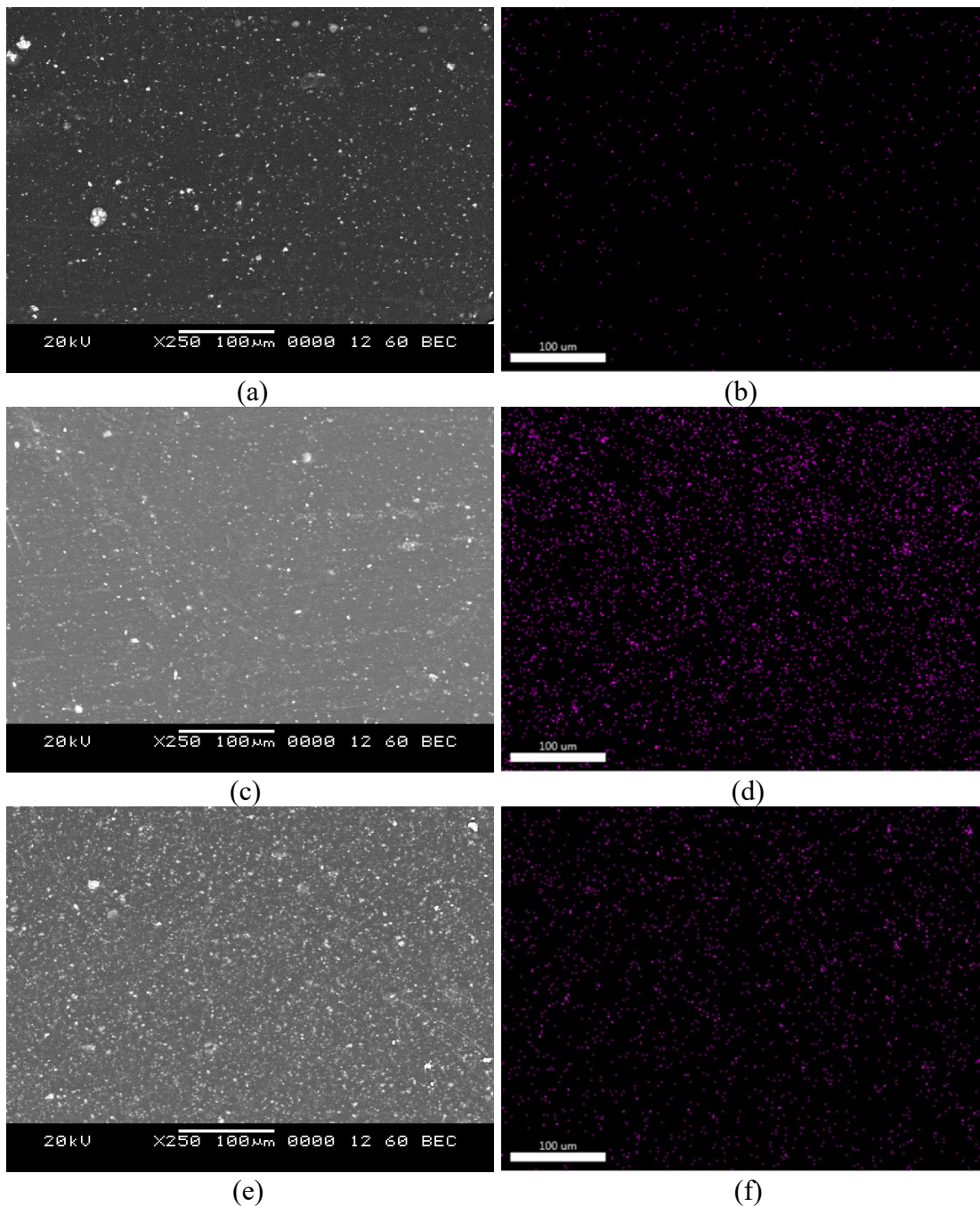


Figure 3.8. BAG distribution (a), (c) and (e) and corresponding elemental mapping (b), (d), and (f) of respective H₅, H₁₀, and H₂₀ filaments.

3.3 Conclusions

The composite blends are evaluated for the homogeneous dispersion of BAG in HDPE matrix. Neat H and composite H/BAG composites are extruded into filaments, and the filament feedstock is investigated for density, porosity (void content), and tensile

properties. The viability of the developed filament as feedstock for the FFF process is evaluated, and the results are summarised as follows:

- Micrography and elemental mapping of composite blends show homogeneous dispersion of BAG in the HDPE matrix.
- The developed filament feedstock is circular in cross-section, and the average diameter is found to be 1.75 ± 0.05 mm, which is well within the acceptable limit for printability.
- Density and void percentage increase with BAG addition. H₂₀ filaments show a 13.8% and 13.31 % higher density and porosity, respectively, than neat H filaments.
- The dispersion of BAG in HDPE is found to be homogeneous and suitable for enhancing mechanical properties.
- T_{d5} and T_{dmax} of filament feedstock are higher than H_G. Residual weights corresponding to the BAG content of the composites obtained from TG curves are within the appreciable limit.
- T_{d5} and T_{dmax} are found to be unaffected by BAG addition. This highlights that the thermal stability of the developed composites is as good as neat H counterparts.
- T_c of the filament feedstock increases concerning H_G. In contrast, T_m of the filament feedstock remains comparable with that of H_G.
- Crystallinity decreases with BAG addition, and H₂₀ exhibits 38.43% reduced crystallinity.
- Crystallinity estimated from XRD data is in agreement with the DSC investigation.
- The matrix HDPE can be processed within the temperature range of 130 – 460 °C without any degradation of the HDPE matrix and for enhanced shear mixing of filler and mouldability (filament extrusion and 3DP).
- Ultimate tensile strength and elongation at ultimate tensile strength decrease with BAG addition. H₂₀ samples show 14.95 and 60.91% lower ultimate tensile strength and elongation at ultimate tensile strength, respectively, compared to neat H filaments.

- Tensile modulus increases with BAG addition, and H₂₀ filaments show a 1.56 times higher modulus than neat H filaments.

The developed neat H and composite H/BAG filaments exhibit homogeneous dispersion of BAG, favouring enhancement of mechanical properties. Composite filaments are flexible enough to be spooled and stiffer to resist forces exerted at the printer head without slipping or fracturing while printing.

4 PRINTABILITY

The printability of the developed neat H and H/BAG composites is collectively evaluated based on substrate selection, thermal and melt behaviour, dimensional stability, and their associated print parameters. The optimization of relevant print parameters in terms of thermal and melt behaviour to obtain dimensionally stable defect-free prints is discussed herein.

4.1 Substrate and print adhesion

The proper substrate selection is the prime prerequisite for the FFF of the developed filament feedstock. The function of the substrate is to provide proper adhesion to the samples while printing. Also, the substrate should detach the prints after printing without affecting their dimensions and negate the necessity for secondary finishing. Improper selection of substrate and adhesives often leads to peeling, delamination and interrupted prints with undesirable dimensionality. For printing neat H, widely used substrates such as glass and adhesive sprayed glass are ineffective regardless of print parameters (Schirmeister et al. 2019). HDPE plates as substrates result in the diffused first layer of the plate (Figure 4.1a). This renders the detachment of the final prints intricate (Bonthu et al. 2020, Patil et al. 2019, Schirmeister et al. 2019). Excellent adhesion and easy detachment of the neat H prints are achieved while printing over the plates made of SEBS (Figure 4.1b) (Schirmeister et al. 2019). However, preparing such plates incurs additional costs, and the plates lose their dimensional integrity throughout usage. In the present work, SEBS adhesive is prepared and applied over a Kapton tape stuck onto a heated glass substrate. The applied adhesives are observed to resist the crystallization-induced peeling or debonding of the first layer from the substrate (Figure 4.1c). This leads to effective adhesion of the samples while printing and successful detachment of dimensionally stable samples. Hence, all the samples (H, H₅, H₁₀, and H₂₀) are printed over Kapton tape applied with SEBS adhesives glued over the heated glass plate.

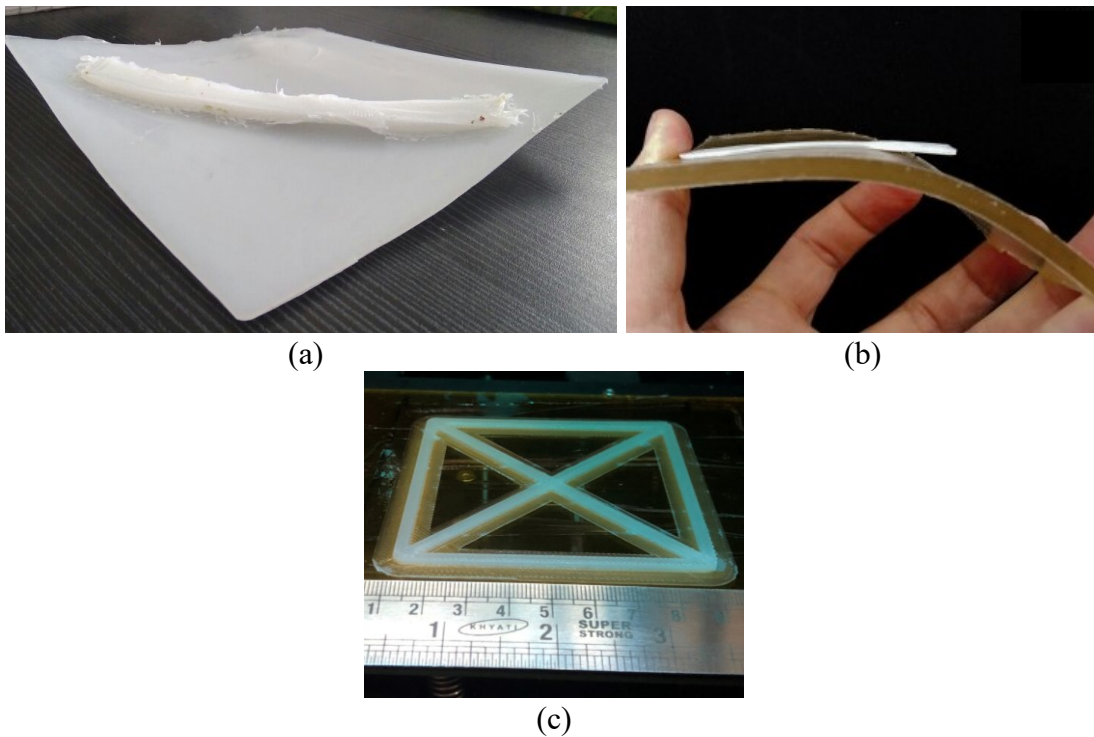


Figure 4.1. Substrates used to print HDPE. (a) HDPE plates (HS et al. 2020, Patil et al. 2019) (b) SEBS plates (Schirmeister et al. 2019) and (c) SEBS adhesives applied over Kapton tape struck on to the heated glass plate (present work).

4.2 Thermal behaviour analysis

4.2.1 Thermal gravimetric analysis (TGA)

The thermal stability of the printed samples is evaluated using TGA. TG and DTG curves are represented in Figure 4.2a, b, respectively, which shows single-stage degradation of HDPE matrix in the temperature range of 450 – 500 °C. This represents the structural decomposition of HDPE matrix. From Table 4.1, it is evident that the addition of BAG does not result in a significant change in T_{d5} and T_{dmax} . However, there is a significant decrease in T_{d5} and T_{dmax} of prints compared to corresponding filaments. T_{d5} of printed samples decreased by 2.11, 2.34, 1.8, and 2.34 %, respectively, compared to H, H₅, H₁₀, and H₂₀ filament counterparts. Similarly, T_{dmax} of printed samples decreased by 1.76, 2.27, 2.60, and 3.27 %, respectively, compared with H, H₅, H₁₀, and H₂₀ filament counterparts. Such a significant difference may be attributed to the processing temperature and the distinct thermal cycles involved during subsequent extrusion and 3DP processes (Aktitiz et al. 2020, Tjong 2012). Neat H printed samples leave no char residue indicating the complete decomposition. Whereas H/BAG

composite printed samples leave char residue, whose residual weight corresponds to BAG in the composition (Table 4.1). However, there is a minimal rise in the residual weight of printed samples compared to filaments due to shearing involved in the subsequent printing process. The maximum degradation rate at T_{dmax} of the printed samples is analogous to its respective filaments and follows a similar trend. The decreases in maximum degradation rate at T_{dmax} with BAG addition, proportional decomposition of HDPE matrix in the H/BAG composites (Lu et al. 2016, Samsudin et al. 2016). From Table 4.1, it is evident that the printed neat H and H/BAG composites are thermally stable as the printing temperature ($< 240\text{ }^{\circ}\text{C}$) is lesser than the T_{d5} of H_G ($\sim 460\text{ }^{\circ}\text{C}$). As the crystallization temperature of BAG is $600\text{ }^{\circ}\text{C}$, the printed samples are found to retain BAG filler with its intrinsic properties (Figure 2.1b).

Table 4.1. Thermal degradation of printed samples.

Sample	T_{d5} ($^{\circ}\text{C}$)	T_{dmax} ($^{\circ}\text{C}$)	Residue (%)	Maximum degradation rate (%/mm)
H	456.9 ± 1.35	482.87 ± 1.57	-	35.16 ± 0.60
H ₅	452.71 ± 1.43	479.24 ± 1.82	4.61 ± 0.09	31.15 ± 0.53
H ₁₀	457.83 ± 1.67	478.04 ± 2.43	8.87 ± 0.16	30.35 ± 0.57
H ₂₀	454.26 ± 1.47	476.27 ± 2.03	18.83 ± 0.33	27.88 ± 0.43

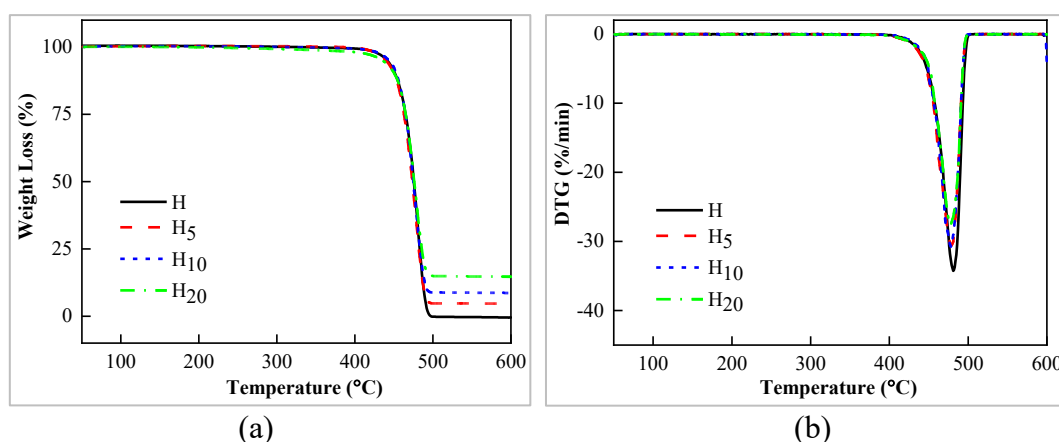


Figure 4.2. Representative (a) TGA and (b) DTG curves of printed samples.

4.2.2 Differential scanning calorimetry (DSC)

The aspects of cooling and melting curves of the printed samples are analogous to that of their respective filaments. Single precise crystallization and melting peaks are observed in the range of 100 - 115° and 120 - 135 °C, respectively (Figure 4.3). There are no significant changes in T_c and T_m of printed samples compared to their respective filaments. H/BAG printed samples exhibit marginal increment in T_c compared to neat H printed samples. Formation of thicker crystal lamellas as the melt nucleates on the BAG surface while cooling results in early crystallization leading to an increase in T_c of the composites (Daver et al. 2018, Patil et al. 2019). In addition, T_m of the printed samples is unaffected by the BAG addition (Figure 4.3b).

The degree of crystallization of composites depends on the concentration of the filler and the thermal processing used while preparing these composites. Table 4.2 shows that the % X_c decreases with BAG addition, which agrees with studies on compression moulded (Doddamani 2020) and printed HDPE samples. The reduction is due to HDPE being the only constituent contributing to the crystallinity peak. Also, the presence of BAG increases the hindrance of the matrix chain mobility and flexibility of the chain to fold, resisting the crystallization growth. % X_c of the printed samples decreases with the addition of BAG, and H₂₀ printed samples show 34.25% lower % X_c than the respective neat H printed samples (Figure 4.3a). Nevertheless, the printed samples show more % X_c than the respective filaments. H₂₀ printed samples exhibit 1.13 times higher % X_c than the filament counterparts. The difference in the crystallinity of the filaments and corresponding prints may be attributed to the distinct thermal history associated with extrusion and subsequent printing (Patil et al. 2019). In general, the thermal process with slower cooling rates promotes a higher possibility of crystallization (Bonthu et al. 2020). Filaments, while extrusion, is passed through a water bath, which acts as a quenching medium. This quenching process restricts the time available for the melt to recrystallize, leading to random order alignment. Whereas in 3DP, samples are printed in a heated environment and allowed to cool by natural convection. Such conditions enhance interfacial bonding through molecular diffusion and re-entanglement, thereby augmenting % X_c (Gao et al. 2020).

Table 4.2. Thermal properties of printed samples.

Sample	T_c (°C)	T_m (°C)	% X_c	
			DSC	XRD
H	109.79 ± 1.49	129.97 ± 1.29	63.32 ± 0.98	64.52 ± 0.98
H ₅	112.21 ± 1.30	130.64 ± 1.28	58.46 ± 0.91	59.54 ± 1.04
H ₁₀	112.49 ± 1.39	131.11 ± 1.29	50.69 ± 0.75	48.80 ± 0.78
H ₂₀	113.14 ± 1.41	129.71 ± 1.37	41.64 ± 0.65	42.57 ± 0.69

Furthermore, printed samples exhibit a slightly distinct cold-crystallization phenomenon compared to their filament counterparts (Figure 4.3a). This signifies the slower cooling rates in 3DP with sufficient time for crystallization and subsequent increase in the % X_c of the prints. The peak intensity decreases with the BAG addition, indicating the restricted HDPE chain mobility. The association between the thermal properties (T_c and T_m) and print parameters (T_p , T_b and T_e) and how they affect the final print quality in terms of dimensional stability and print-induced defects are discussed later.

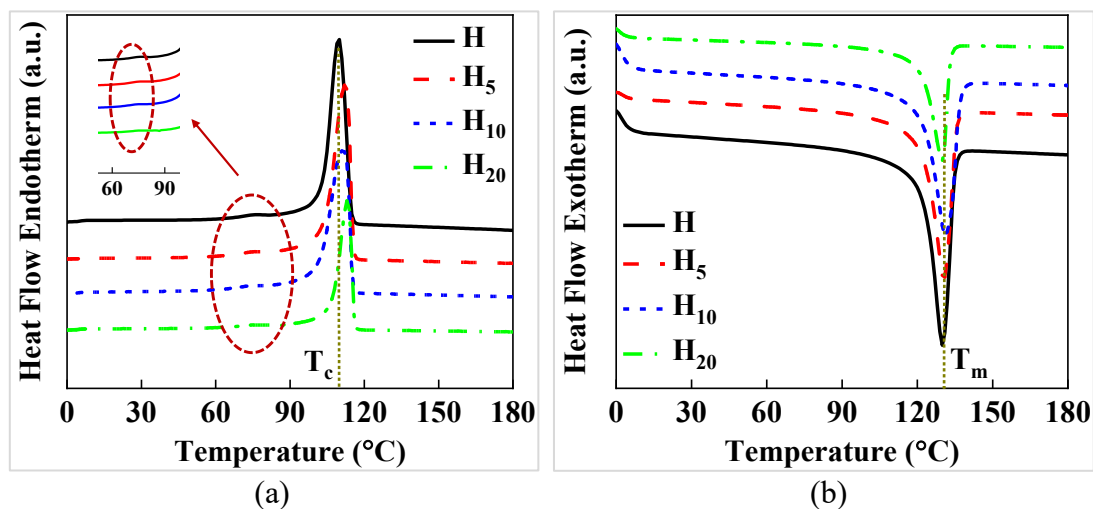


Figure 4.3. DSC curves for (a) cooling cycle with in-sets showing cold-crystallization phenomenon and (b) second heating cycle print samples.

4.2.3 X-ray Diffraction

Printed samples are subjected to XRD analysis to correlate with the crystallinity values obtained from DSC analysis. Figure 4.4 shows the XRD pattern of the printed samples. Table 4.2 shows that the crystallinity decreases with BAG addition, and H₂₀ printed samples show 30.92% decreased crystallinity than neat H printed samples. This is highlighted by the reduction in the intensity of the peaks of composites samples. The

intensity of the sharp and narrow characteristic peaks decreased, widened, and even disappeared as the filler content increased (Takahashi et al. 1988, Xiang et al. 2017). However, the crystallinity of printed samples is higher than the respective filaments. Printed samples H, H₅, H₁₀, and H₂₀ exhibit 17.17, 10.21, 14.68 and 22.73% higher crystallinity than their respective filaments. The diffraction pattern of the printed samples is sharper than its filament counterpart (Figure 3.6b and Figure 4.4). This is attributed to the additional thermal cycle involving higher temperatures and long process time during the printing process (Schirmeister et al. 2021, Spoerk et al. 2017). The results estimated from XRD data are in agreement with the DSC results. Estimating the crystallinity is essential in determining the printing parameters of semi-crystalline composites. Properties such as polymerization-induced shrinkage and its associated warpage are estimated in terms of crystallinity (Spoerk et al. 2020, Spoerk et al. 2019, Zhao et al. 2008), and countermeasures are formulated to achieve dimensionally stable printed parts. The effects of printing parameters and their influence on dimensional stability and quality of the printed final parts are discussed in the coming sections.

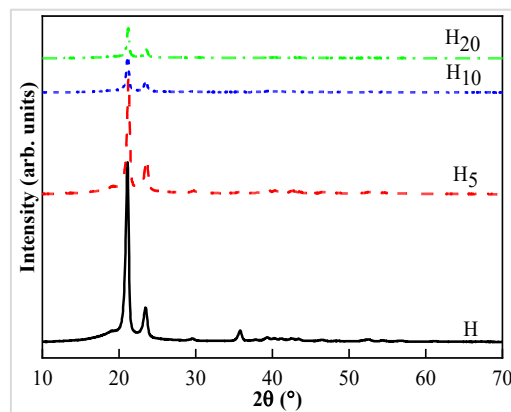


Figure 4.4. XRD of printed samples.

4.2.4 Coefficient of thermal expansion (CTE)

Semicrystalline neat H and H/BAG composites undergo polymerization-induced shrinkage upon re-melting and cooling during 3DP process. This distinct behaviour significantly influences the dimensional stability of the printed samples and can be better comprehended by studying the linear thermal expansion. Adding low CTE BAG ($13.84 \times 10^{-6}/^{\circ}\text{C}$) (Zhao et al. 2008) to HDPE matrix acts as a shrinkage inhibitor. This results in the restriction of stretched polymer chain shrinkage along the contraction

direction (Spoerk et al. 2017, Spoerk et al. 2019). Figure 4.5 shows that CTE decreases with BAG addition. Table 4.3 shows that the reduction in CTE is maximum for composites and H₂₀ samples show 50.62% lower CTE than neat H samples. Furthermore, the CTE of the composites is directly proportional to print-induced thermal stresses (Kousiatza et al. 2019). As the composites exhibit lower CTE, they are observed to acquire minimum thermal stress leading to dimensionally stable H/BAG composite samples. Such qualities are essential to printing complex, integrated, functional composite implants/scaffolds.

Table 4.3. CTE and % reduction in CTE values of printed samples.

Sample	CTE ($\times 10^{-6}/^{\circ}\text{C}$)	% reduction in CTE wrt H
H	114.02 \pm 2.73	-
H ₅	72.12 \pm 2.67	36.75
H ₁₀	61.31 \pm 2.42	46.23
H ₂₀	54.98 \pm 1.90	61.31

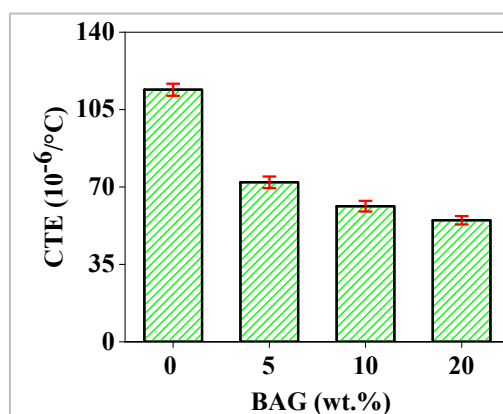


Figure 4.5. CTE values printed samples.

4.2.5 Thermal behaviour and printability of H/BAG composites

Peeling or debonding of the printed first layer is the property significantly influenced by the thermal behaviour. The innate nature of the HDPE matrix to pack together while cooling leads to peeling the printed first layer (Figure 4.6a) (Gao et al. 2020, Singh et al. 2020). This crystallization behaviour can be tailored to print parameters such as T_b, T_p, and T_e to avoid such peelings. Increasing T_b from ambient to near T_c of feedstock is

proven to slow the crystallization rates (Lu et al. 2016, Zhao et al. 2008), thereby enabling the prints to be at elevated temperatures during the printing process. Prints with an additional raft of 8 mm and T_b of 110 °C are observed to minimize the solidification-induced shrinkage. This leads to improved adhesion of the printed first layer leading to dimensionally stable prints (Figure 4.7a, b). Insufficient T_p often results in defective prints with insufficient diffusion and print-induced voids leading to poor mechanical performances (Economidou and Karalekas 2016). Figure 4.6b shows a sample printed at 200 °C (T_p) exhibiting insufficient diffusion and print-induced voids (Figure 4.6d) (Diederichs et al. 2019, Gao et al. 2020). To negate this, the samples are printed at elevated T_p (240 °C), leading to adequately diffused rasters with zero print-induced voids. Such elevated T_p also improves the feedstock's flowability and wettability, leading to dimensionally stable prints (Mummareddy et al. 2020, Spoerk et al. 2018).

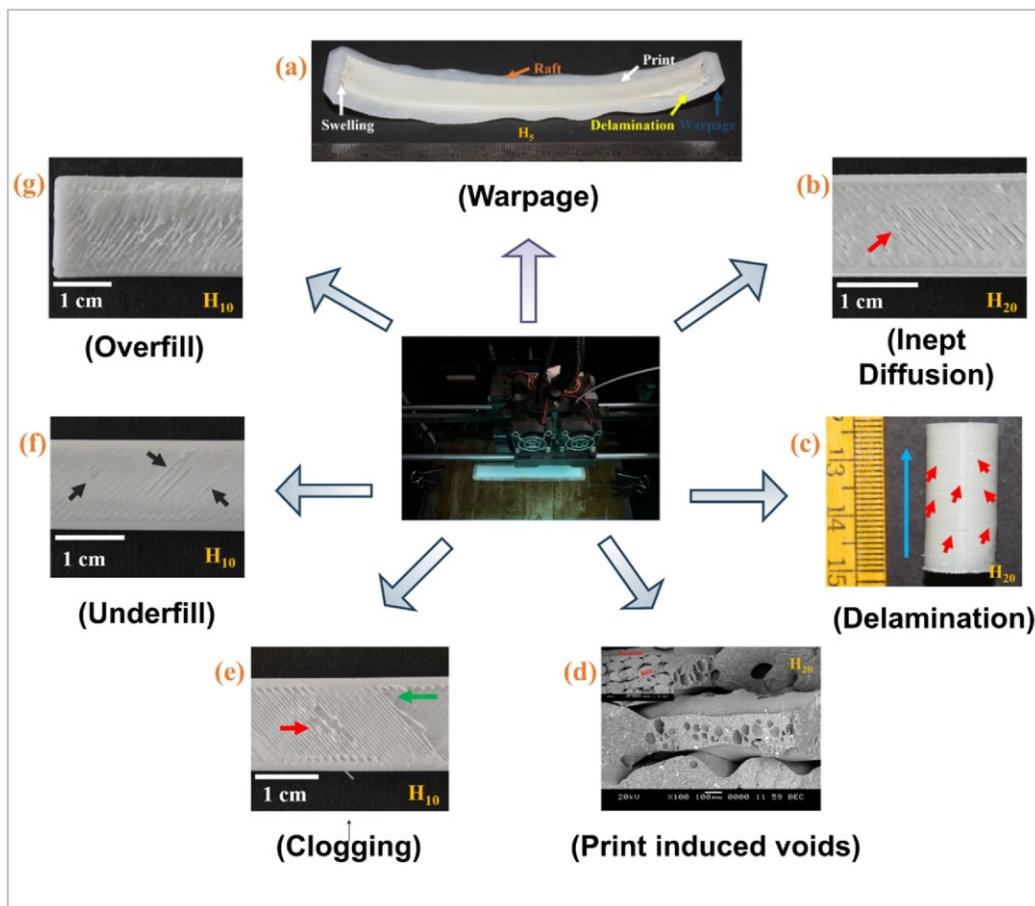


Figure 4.6. Representation of printing defects such as (a) warpage, (b) inept diffusion, (c) delamination, (d) print induced voids, (e) clogging, (f) underfill and (g) overfill.

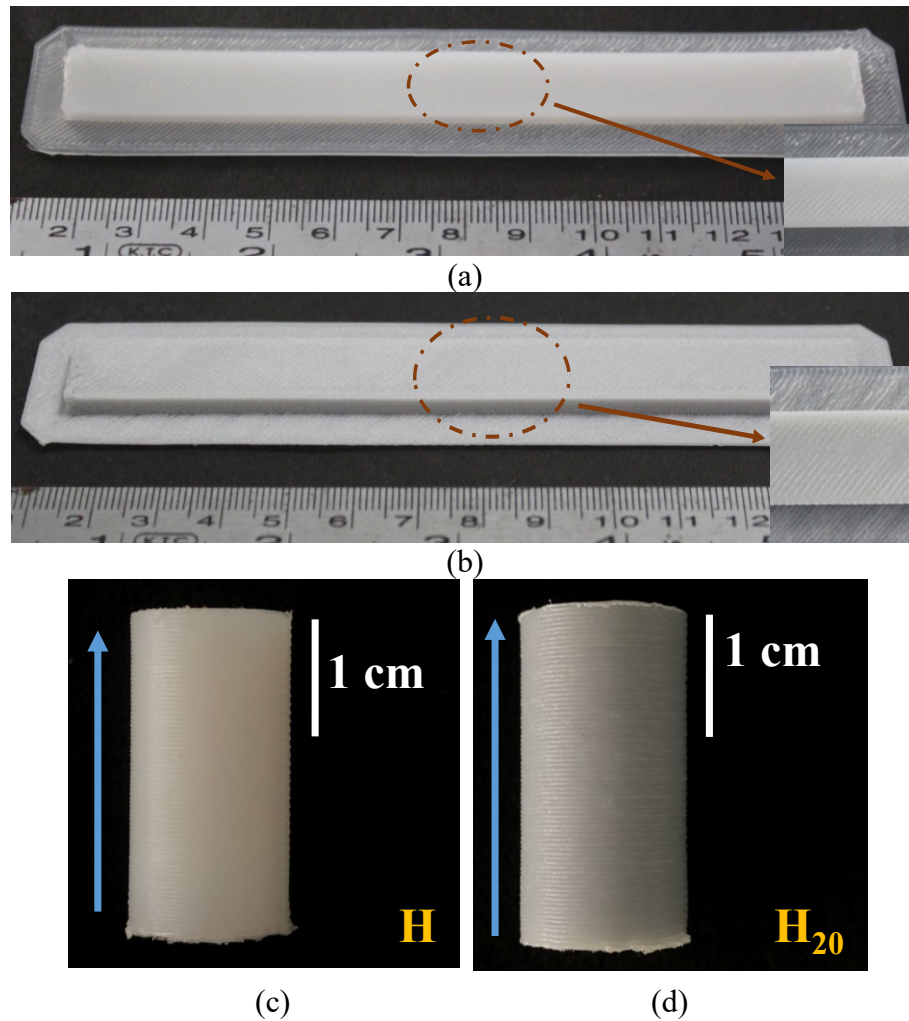


Figure 4.7. Representative dimensionally stable neat H (a,c) and H₂₀ samples (b,d). (Arrow indicating build direction)

Thermal gradient across the Z-direction of the prints can lead to delamination, shrinkage, and warpage (Liu et al. 2019, Peñas et al. 2020). Figure 4.6c shows delaminated layers along Z-directions away from the print bed. This effect can be minimized by increasing T_e to facilitate uniform temperature distribution (Kousiatza et al. 2019, Liu et al. 2019). Samples printed at elevated T_e of 70 °C are found to be dimensionally stable with negligible warpage and delamination (Figure 4.7c, d). Furthermore, thermal stresses, warpage, and delamination are directly proportional to CTE values (Economidou and Karalekas 2016, Kumar et al. 2020, Samsudin et al. 2016). This signifies that the composites are easily printed compared to neat H samples (Cao et al. 2015). In addition to T_b , T_p , T_e , and CTE, post-print cooling also affects

dimensional stability. The prints, upon completion, are cooled down uniformly inside the print envelope to minimize the thermal stresses and associated dimensional instability (Balla et al. 2020). Such enhanced temperature setting (T_p - 240 °C, T_b - 110 and T_e - 70 °C) and post-print natural cooling help in controlling the crystallization kinetics. The enhanced temperatures result in increased cross-flow of low viscosity melt, which leads to a higher degree of interfacial diffusion (Sinha and Meisel 2020). The resultant cohesion from such interfacial diffusion improves the possibility of polymer chains diffusing across the interface and re-entangle. Prolonged heat retention at higher T_p and T_e enables the entangled polymer chains to have sufficient time to crystallize (de Carvalho et al. 2020). These crystallographic changes lead to dimensionally stable prints with reduced warpage and voids (Figure 4.7). Furthermore, uniform distribution of thermal stresses and improved mechanical properties are obtained from these elevated temperatures (Sinha and Meisel 2020). All the prints are printed with the same temperature parameters, thereby nullifying the thermal effects, if any.

4.2.6 Warpage analysis

The warpage primarily determines the dimensional stability of the printed semicrystalline H/BAG composites due to volumetric shrinkage leading to thermal stresses. Samples are printed as per dimensions depicted in Figure 2.9a, using the print parameters listed in Table 2.2. The warpage results of the developed neat H and H/BAG composites are summarized in Figure 4.8. The dimensional deviation of the prints from the actual CAD model due to thermal stress is represented in millimeters via color code. The printed first layer is visible as the scanned surface. Hence, the negative values (red area) indicate the warpage pointing away from the bed. The positive values (blue area) indicate the combined warpage and shrinkage effect. The green area represents the CAD model's ideal no deviation (0.0 mm). Horizontal dark lines are marked in the color code to give the range of displacement distribution and histograms beside the color code to understand the warpage better. The deviation range is reduced from 2.0 to 0.9 mm with the addition of BAG. This highlights the fact that the addition of stiffer BAG results in minimized warpage, as observed in the earlier studies on printed cenosphere-filled composites (Patil et al. 2019), and pearlite-filled composites (Economidou and

Karalekas 2016), and injection moulded solid glass bead composites (Schirmeister et al. 2019). This is because the addition of BAG results in a decrease of %X_c, leading to the enhanced dimensional stability of the composites, as observed by (Schirmeister et al. 2021). Some portions of the first layer adhere better than the rest because the printing surface is never ideally flat. This contributes to the varying degree of warpage (Bonthu et al. 2020, Spoerk et al. 2017). The color change observed along the particular corner of neat H, and H₅ (Figure 4.8a, b) samples are due to such a difference in the degree of adhesion. Similar changes are not observed in H₁₀ and H₂₀ samples (Figure 4.8c, d), as differences in the degree of adhesion are compensated by reduced %X_c and CTE. The combined effect of warpage and shrinkage represented by blue color lies in the close range of 0.7 to 0.9 mm, which compliments the current print parameters. The enhanced material flow rate and temperature setting are used to print the samples, and post-print natural cooling helps achieve dimensionally stable prints (Singh et al. 2018).

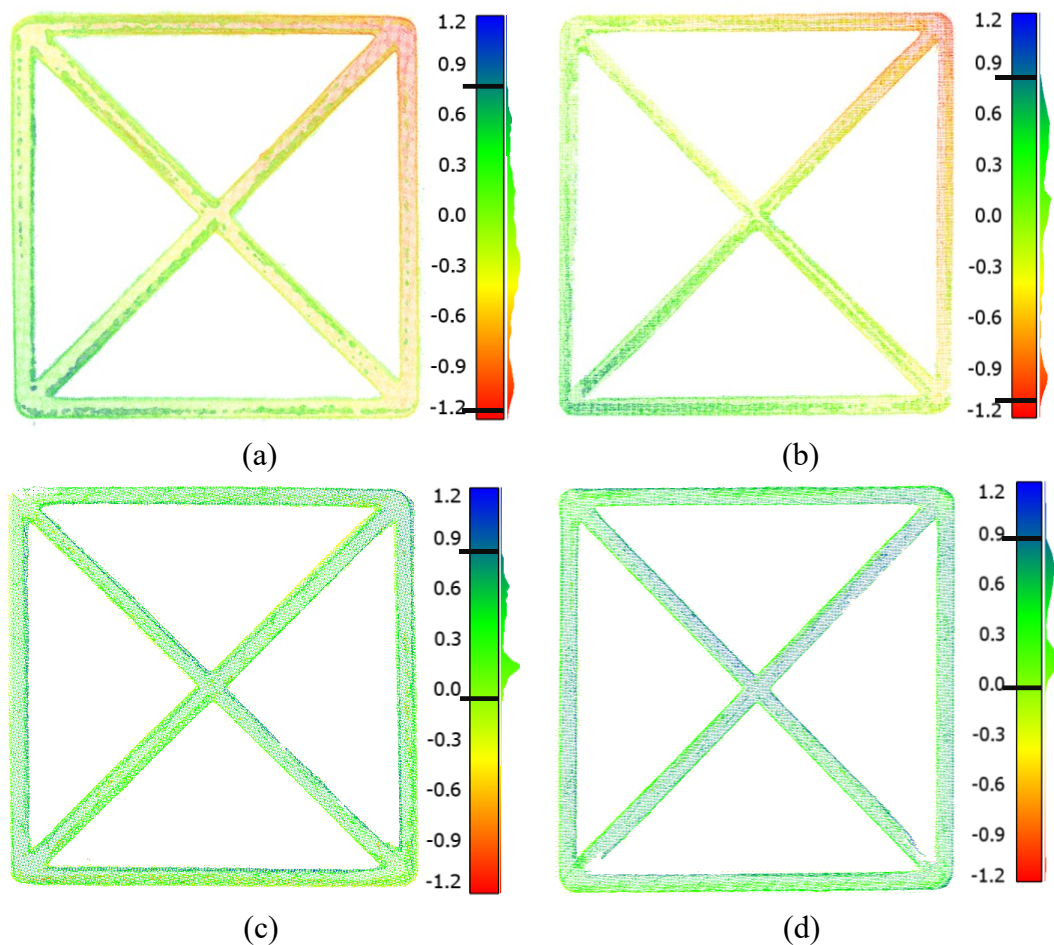


Figure 4.8. Optical warpage analysis of (a) neat H, (b) H₅, (c) H₁₀, and H₂₀ printed samples. All dimensions are in mm.

4.3 Melt behaviour analysis

Understanding the melting behaviour of the composites is essential to predict and control printability. To ascertain that, MFI and rheological properties of the feedstock are studied.

4.3.1 Melt flow index (MFI)

MFI determines the fluidity of the neat H and H/BAG composites under constant load. Stiffer BAG hinders the mobility of the HDPE chain, and the resistance to chain mobility increases with BAG addition (Doddamani 2020, Xiang et al. 2017). This results in a decrease in the MFI of composites with BAG addition (Figure 4.9). Neat H samples reported the highest MFI compared to H/BAG composites (Table 4.4). A decrease of 12.38, 18.88, and 37.15 % is obtained by adding BAG at 5, 10, and 20 wt.%, respectively. Predicting the printability of composites based on MFI is not adequate as the effect of shear rate on the rheological properties during the actual printing is not considered. Hence, rheology studies are carried out for a better understanding of the flow behaviour of these composites.

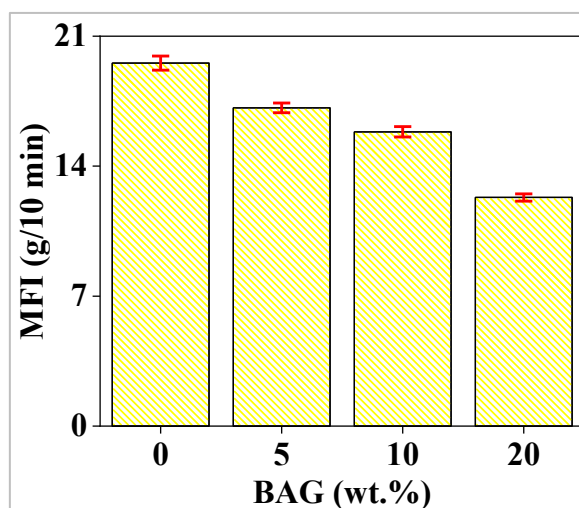


Figure 4.9. MFI of feedstock composites.

Table 4.4. MFI and percentage reduction MFI of feedstock composites.

Sample	MFI (g/10 min)	% reduction in MFI wrt to H
H	19.55 ± 0.17	-
H ₅	17.14 ± 0.11	12.32
H ₁₀	15.85 ± 0.12	18.93
H ₂₀	12.31 ± 0.09	37.03

4.3.2 Rheology

Understanding the melting behaviour of the composites is essential to control printability. To ascertain that, the rheological properties of the feedstock are studied. The results of dynamic rheological studies at three distinct frequencies (0.0628 (0.01 Hz), 6.28 (1 Hz), and 628 rad/s (100 Hz)) are listed in Table 4.5. Figure 4.10a, b show that the storage (G') and loss (G'') modulus of the samples increases with an increase in angular frequency and the concentration of BAG. This behaviour may be due to the formation of a network-like structure by extensive restriction of polymer chain mobility (Stolz et al. 2020). However, both G' and G'' composites approach neat H values at higher angular frequencies due to increased inflexibility and rigidity of HDPE structure (Economidou and Karalekas 2016). All the samples are predominately viscous as G'' value is more significant than G' across the entire angular frequency (Zeltmann et al. 2016). H₂₀ displays 10.78 and 3.71 times higher G' and G'' respectively than neat H at 0.0628 rad/s. Figure 4.10c shows the complex viscosity (η^*) of the samples decreases with an increase in angular frequency. Neat H samples display Newtonian plateau at lower frequencies and shear thinning at higher frequencies. The addition of BAG beyond 5% results in the disappearance of the Newtonian plateau at a lower frequency, and all samples exhibit prominent shear thinning at higher frequencies. BAG – H interaction increases with BAG inclusion, impeding H chain mobility and increasing η^* at lower frequencies (Economidou and Karalekas 2016, Mummareddy et al. 2020). η^* of H₂₀ is increased by 0.73 times that of neat H at 0.0628 rad/s. As a result of intense shearing at higher angular frequencies, η^* of composites approach neat H values (Kumar et al. 2020).

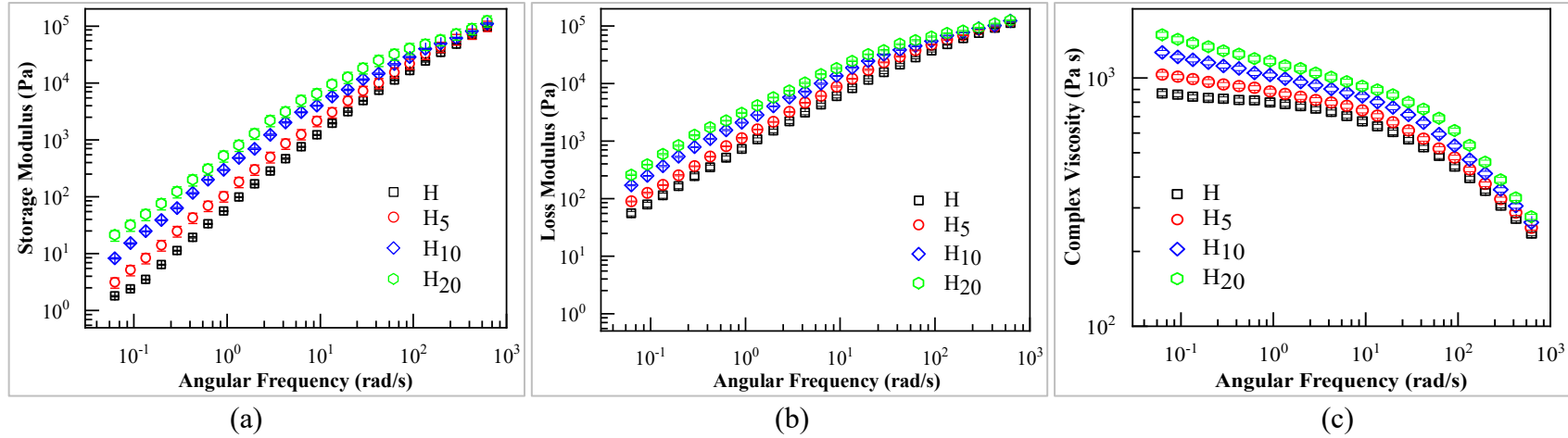


Figure 4.10. (a) Storage modulus, (b) loss modulus and (c) complex viscosity of printed samples at 240 °C frequency sweep.

Table 4.5. Rheological properties of the printed samples.

Sample	Frequency (rad/s)								
	0.0628			6.28			628		
	G' (Pa)	G'' (Pa)	η^* (Pa s)	G' (Pa)	G'' (Pa)	η^* (Pa s)	G' (Pa)	G'' (Pa)	η^* (Pa s)
H	1.80 ± 0.03	54.99 ± 1.15	865.74 ± 17.75	754.01 ± 15.08	4285.57 ± 89.82	701.54 ± 12.61	95966.37 ± 2015.11	113180.22 ± 2377.47	236.17 ± 4.96
H ₅	3.11 ± 0.07	89.11 ± 1.73	1033.30 ± 23.77	1250.51 ± 24.39	6095.94 ± 146.21	772.23 ± 15.45	100223.64 ± 2104.24	121993.65 ± 2317.11	249.11 ± 4.86
H ₁₀	8.26 ± 0.15	169.99 ± 3.73	1266.10 ± 24.06	3043.33 ± 63.91	9992.32 ± 209.83	871.64 ± 20.92	110356.54 ± 2097.21	118842.84 ± 2020.37	261.52 ± 5.26
H ₂₀	21.10 ± 0.57	258.42 ± 5.95	1493.80 ± 31.35	4925.12 ± 103.42	14546.37 ± 392.81	967.39 ± 20.32	122710.33 ± 2515.84	120896.74 ± 2538.91	276.03 ± 5.70

4.3.3 Melt behaviour and printability of H/BAG composites

In addition to thermal behaviour, melt behaviour plays a predominant role in determining the print quality in terms of interfacial diffusion, print-induced voids, and warpage (Mummareddy et al. 2020). Regardless of exhibiting higher η^* , H₂₀ filament feedstock is effortlessly spooled without any degree of shattering (Figure 3.7c). However, the higher η^* of the composite feedstock often leads to a clogged nozzle resulting in incomplete material deposition (Figure 4.6e) and poor wettability (Figure 4.6f) (Lee et al. 2020). CTE values of the developed feedstock also complement the observed poor wettability (Figure 4.6d). Lower CTE values result in restricted material flow (Diederichs et al. 2019, Economidou and Karalekas 2016), leading to partial diffusion of individual rasters rendering printed samples with print-induced voids (Figure 4.6d). The defects associated with melt flow rate can be compensated by increasing the material flow rate (Patil et al. 2019, Singh et al. 2020), as the material flow rate is inversely proportional to the η^* of the feedstock (Zeltmann et al. 2016). Such conditions decrease η^* , thereby improving the material flow and leading to sufficient interfacial diffusion and wetting. Figure 4.6f, g show the samples printed with the extruder multiplier of 1x and 1.2x, leading to underfilled and overfilled prints, respectively. Based on visual inspections, the extruder multiplier is altered to 1.05x and 1.1x for printing H₁₀ and H₂₀, respectively. Printing at an increased material flow rate leads to pressure drop at the nozzle resulting in slippage or shear of the feedstock (Kumar et al. 2020). However, the developed H/BAG composite feedstock is printed effortlessly exhibiting their ability to resist such slippage. Thus, the extruder multiplier is increased in association with elevated temperature parameters (T_b , T_p and T_e) to account the difference in rheological behaviour of the developed feedstock to achieve seamless material flow leading to dimensionally stable, defect-free prints (Figure 4.7).

4.4 Surface and microstructural features of printed samples

The samples are printed at elevated temperature conditions and modified melt parameters. The resulting samples are dimensionally stable with improved layer adhesion due to uniform temperature distribution and annealing of the printed samples. The seamless interface between layers exhibits the proper selection of printing parameters (Figure 4.11a). Such seamless diffusion improves mechanical properties

and eliminates anisotropy (Schirmeister et al. 2019). Figure 4.11b, c show no weld line defects across the freeze fractured surface along the thickness direction. Similarly, there are no inter/intra layer air gaps in both neat H and H/BAG composite samples. Hence there is no delamination of the layers leading to dimensionally stable printed samples (Barbieri et al. 2013, Lee et al. 2020). This helps in obtaining the high repeatability of measured responses. Figure 4.11d shows freeze fractured H₂₀ prints with the uniform BAG distribution throughout the HDPE matrix.

From Figure 4.11b, it is evident that freeze fractured neat H printed samples have no voids. The micrograph of freeze fractured H₂₀ sample shows uniform distribution of voids (Figure 4.11c) and BAG (Figure 4.11d) throughout the printed sample. From Table 4.6, it is evident that the density of the printed samples increases linearly with the addition of BAG. H₂₀ exhibits a density that is 1.15 times higher than neat H samples. Similarly, the porosity of the composites increases linearly with BAG addition. H₂₀ samples show a maximum porosity of 12.23%. Such prints with a three-phase structure facilitate better energy absorption and localized osteoblast activity (Bose et al. 2013, Doddamani 2019). The porosity of the printed samples is marginally less (5~8%) compared to their respective filament (Table 3.1). The marginal difference is due to increased printing temperature (240°C) as compared to the extrusion temperature (average 150°C). This temperature difference would have reduced the viscosity, thereby improving the matrix flow during the printing process.

The printing parameters (T_p , T_b , T_e , extrusion multiplier, LT, and printing speed) chosen in this work did not induce any print-associated defects leading to dimensionally stable prints. Significantly, higher printing temperatures result in excellently diffused layers leading to enhanced mechanical properties. Complex geometries such as human mandible and partial cranial bones are printed at optimized parameters using the developed neat H and H₂₀ feedstock composite (Figure 4.11e, f)

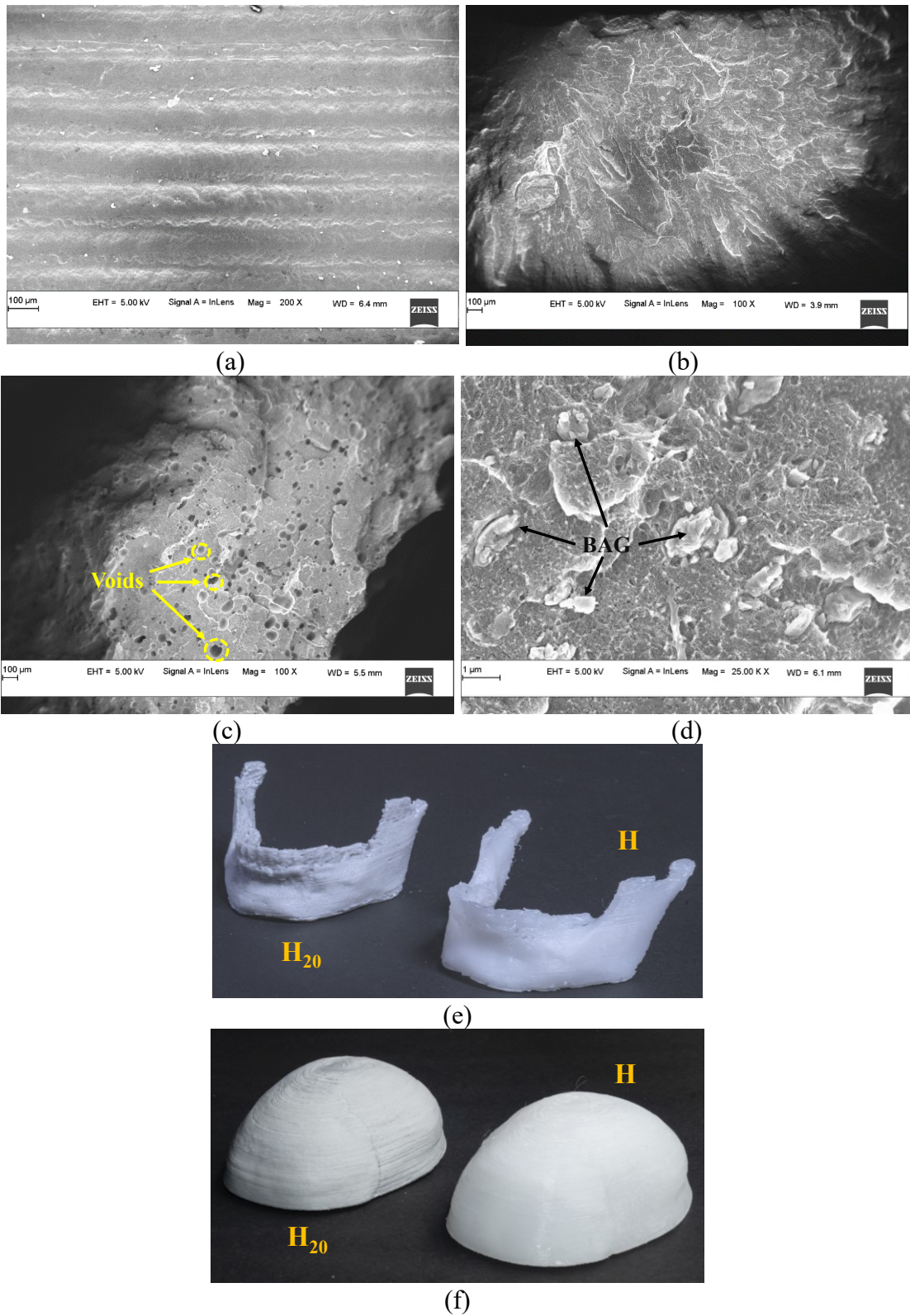


Figure 4.11. Micrographs of (a) surface topography and seamless layer interface and (b) freeze fractured neat H printed samples. (c) Freeze fractured and (d) BAG distribution in H₂₀ printed samples. Printed (e) human mandible and (f) segment of cranium.

Table 4.6. Density and void content of printed samples.

Sample	Theoretical density (kg/m ³)	Experimental density (kg/m ³)	Void content (%)
H	950	949.50 ± 24.68	0.05
H ₅	1023.92	987.24 ± 25.69	3.58
H ₁₀	1097.84	1024.87 ± 26.65	6.65
H ₂₀	1245.68	1093.37 ± 28.43	12.23

4.5 Conclusions

The printability of the developed neat H and H/BAG feedstock composites are evaluated in terms of substrate selection, thermal and melt behaviour. The resulting printed samples are evaluated in terms of print-induced defects such as warpage, delamination, voids, underfilling and overfilling. The significant findings are as follows:

Substrate and print adhesion

- The proposed SEBS adhesives provide excellent adhesion to the first layer leading to dimensionally stable printed samples.
- Detachment of the printed samples from the substrate is easier without any necessity for secondary finishing operations.
- SEBS adhesives are found to be stable at prolonged and elevated temperature conditions.

Thermal behaviour analysis

- The coefficient of thermal expansion decreases with BAG addition. H₂₀ samples show a 50.62% reduced coefficient of thermal expansion than neat H samples.
- On-set and maximum degradation temperatures are found to be unaffected by BAG addition. This highlights that the thermal stability of the developed composites is as good as neat H counterparts.
- On-set and maximum degradation temperature of prints are lower than their filament counterpart. On-set and maximum degradation temperature of H₂₀

printed samples are decreased by 2.34 and 3.27%, respectively, compared to their filament counterpart.

- The degree of crystallinity decreases with BAG addition. H₂₀ shows a 38.43 and 34.25% reduced degree of crystallinity than neat H filaments and printed samples, respectively. XRD evaluation of crystallinity is analogous to DSC estimation.
- Due to cold-crystallization, printed samples' crystallinity is higher than their filament counterparts.
- Crystallization temperature increases marginally with the addition of BAG. Melting temperature is found to be unaffected by BAG addition.
- Solidification-induced shrinkage is reduced by increasing T_b to 110 °C and providing a raft of 8mm.
- T_p is increased to 240 °C to render printed samples with zero print-induced defects.
- T_e is elevated to 70 °C to minimize thermal gradient along Z-axis, leading to dimensionally stable printed samples with negligible warpage and delamination.
- Printed samples are cooled to room temperature inside the build chamber via natural convection.

Melt behaviour analysis

- MFI decreases with BAG addition. H₂₀ samples show 37.15% reduced MFI than neat H samples.
- Neat H and H₅ samples exhibit Newtonian plateau at a lower frequency. Addition of BAG beyond 5% results in the disappearance of the Newtonian plateau. All the samples exhibit shear-thinning at higher frequencies.
- Storage and loss modulus increases with BAG addition. At low frequency (0.0628 rad/s), H₂₀ samples display 10.78 and 3.71 times higher storage and loss modulus, respectively, than neat H samples.
- The complex viscosity of the composite feedstock increases with BAG addition. H₂₀ shows 1.73 times higher complex viscosity than neat H samples at a lower frequency of 0.0628 rad/sec.

- Higher complex viscosity of composite feedstock leads to incomplete deposition of material. Material flow rate (extruder multiplier) is enhanced to 1.05x and 1.1x for H₁₀ and H₂₀ samples to get essential interfacial diffusion and wetting.
- The developed feedstock is printed at an increased material flow rate without any slippage or breakage at the entry of the nozzle.

Surface and microstructural features of printed sample

- Optimized print parameters result in seamless diffusion of layers. This leads to samples with zero weld line defects resulting in enhanced mechanical properties.
- Samples printed with the optimized parameters are dimensionally stable and free of delamination and swelling.
- The porosity of the samples increases with BAG addition, and the values are close to that of their respective filaments.

A representative human mandible and a segment of the human cranium are printed to demonstrate the printability of developed neat H and H/BAG composite feedstock. This shows the potential of the developed feedstock to manufacture patient-specific implant/scaffolds.

5 TENSILE PROPERTIES

5.1 Tensile properties of neat H and H/BAG prints

Mechanical properties of the composite mainly depend on filler size, shape, homogeneous dispersion, interaction with the matrix as well as the inherent properties of the matrix (Ponnamma et al. 2019, Victor and Muthu 2014). Figure 5.1 illustrates the tensile response of the printed samples in terms of the stress-strain curve. It is evident that the initial linear response of the prints is similarly followed by a distinct tensile response (Figure 5.2). Neat H and H₅ samples undergo yielding with increasing load prior to fracture (Figure 5.1 and Figure 5.2). The observed broom-like fibrous end indicates fibrillation of individual raster (Singh et al. 2018) and is represented by the necking region (Figure 5.2). H₁₀ and H₂₀ exhibit brittle fracture without indicating macroscopic ductility (Figure 5.2). With the addition of the BAG, the availability of matrix volume to deform gets reduced. Hence, sample failure is initiated by the microscopic plastic deformation of the HDPE in the presence of stiffer BAG (Figure 5.2).

Table 5.1 documents the tensile response of the printed samples. It is interesting to note that the tensile response of prints is distinguishably different from their respective filament counterparts (Figure 3.3b and Figure 5.4). Printed neat H and composite samples exhibit 1.09, 1.26, 1.19, and 1.27 times better modulus than the respective filament feedstock (Table 3.4 and Table 5.1). This may be due to the cross-linking and realignment of polymer chains during printing (Patil et al. 2019).

The modulus of the prints increases linearly with the addition of BAG. H₂₀ samples exhibit a 1.82 times higher value than neat H samples. This improvement is due to a stiffer BAG that is homogeneously distributed. Particles of BAG act as stress concentrators and facilitate brittle fracture of the prints resulting in reduced UTS and elongation at UTS (Pahlevanzadeh et al. 2018, Paspali et al. 2018). H₂₀ shows 12.9% and 52.62% lesser UTS and elongation at UTS, respectively, compared to neat H prints. The flexibility of the developed composites is found to be decreasing significantly with filler addition. Neat H samples display a higher elongation (1.93 times that of H₂₀) at

fracture than the H/BAG composites. The fracture strain of H/BAG composites decreases with the addition of BAG. H₂₀ samples show 92.53% reduced fracture strain compared with neat H samples. However, fracture strength increases with the addition of BAG. H₂₀ samples exhibit 1.48 times higher fracture strength than neat H samples. The modulus and UTS of the printed neat H samples are compared with the injection-moulded counterpart. The printed neat H samples display 26% higher modulus values and comparable UTS with respect to injection moulded samples (Bharath Kumar et al. 2016).

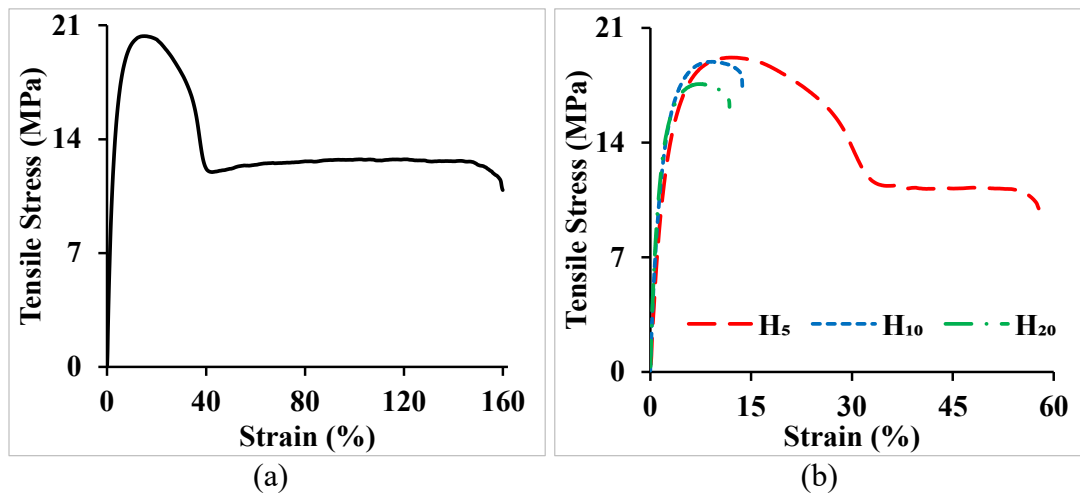


Figure 5.1. Stress – strain curves of (a) neat H and (b) H/BAG printed samples.

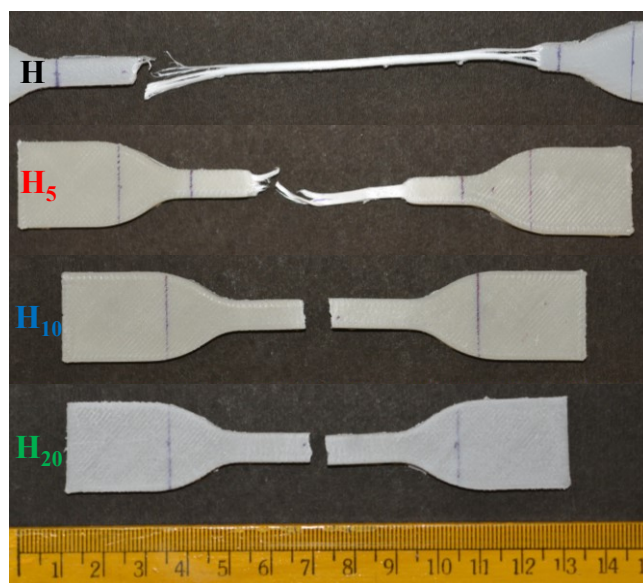


Figure 5.2. Photograph showing failure of tensile samples.

Table 5.1. Tensile response of printed samples.

Sample	Modulus (MPa)	UTS (MPa)	Elongation at UTS (%)	Fracture strength (MPa)	Fracture strain (%)
H	677.27 ± 9.35	20.31 ± 0.32	15.28 ± 0.22	10.87 ± 0.16	159.12 ± 2.39
H ₅	907.52 ± 11.17	19.12 ± 0.24	12.23 ± 0.17	9.98 ± 0.17	57.68 ± 0.85
H ₁₀	1101.54 ± 13.21	18.93 ± 0.21	9.37 ± 0.18	17.14 ± 0.22	13.74 ± 0.30
H ₂₀	1230.32 ± 14.16	17.69 ± 0.24	7.24 ± 0.14	16.06 ± 0.20	11.88 ± 0.24

5.2 Micrographic analysis of fractured samples

The fractured samples are subjected to electron microscopy to understand the failure mechanism, which aids in better designing the components. Neat H and H₅ samples display ductile failure, whereas H₁₀ and H₂₀ samples exhibit brittle failure. Hence micrography is performed on fractured surfaces of H₁₀ and H₂₀ samples. From the images (Figure 5.2 and Figure 5.3), fracture of H/BAG composites occurs in three stages (Arencón and Velasco 2009). Upon application of tensile load, BAG will debond from the HDPE matrix, leaving voids (Stage I). This is facilitated by the fibrils formed during microscopic ductile formation. As the deformation progresses, voids will enlarge in the stress direction resulting in dimples around the BAG particles (stage II). The formed dimples will coalesce, leading to microscopic ductile deformation and macroscopic brittle failure (stage III). Submicron voids are formed during coalescence (Wang et al. 2018). Features such as coalesces, dimples, sub-microscopic voids, and fibrils formed during the stages of tensile failure are depicted in Figure 5.3. BAG size, distribution, and quantity determine the strain level in stages II and III. Thus, adding homogeneously distributed fine BAG particles decreases the strain of composite samples (Figure 5.2), leading to a ductile-brittle transition.

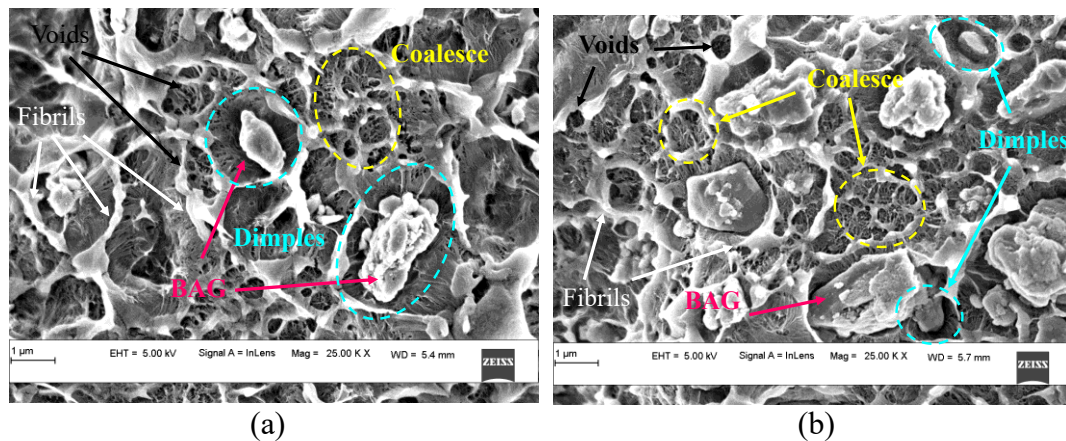


Figure 5.3. Micrography of fractured (a) H₁₀ and (b) H₂₀ tensile samples showing stiffer BAG and deformation features such as fibrils, voids and coalesce.

5.3 Property map

Tensile strength and tensile modulus of various biocompatible thermoplastic polymer composites reinforced with various bioactive fillers are plotted against each in Figure 5.4 (Ang et al. 2007, Dahl et al. 2018, Fouad and Elleithy 2011, Jaggi et al. 2012, Kaur et al. 2019, Keothongkham et al. 2017, Li et al. 2017, Maroulakos et al. 2019, Martin et al. 2019, Roy and Sailaja 2015, Senatov et al. 2016, Shuai et al. 2013, Wang et al. 2016, Wang et al. 2015). The information is extracted from the published literature on composites processed via conventional manufacturing processes and compared with the present study's results. The developed BAG based composites are compared with graphene, HAp, zirconia, and tricalcium phosphate-based composites. It is observed from Figure 5.4 that the tensile strength of the developed composites is comparable with the other particulate reinforced composites. However, the tensile modulus of the developed BAG composites is higher than the graphene, HAp, zirconia, and TCP-based composites.

The primary objective of the developed feedstock is to be used as implant materials. Hence, the obtained properties are compared with the properties of the human bone. The properties of the cortical bone are higher than the trabecular bone owing to its inherent degree of porosity (Figure 5.4). Hence, the properties of the developed composites are also compared with trabecular bone properties. These trabecular bones exhibit tensile strength and modulus in the range of 1 ~ 20 MPa and 50~520 MPa,

respectively (Kaur et al. 2019). It can be observed from Figure 5.4 that the strength of the developed composites is in close range of that of the trabecular bone. Whereas modulus values are higher than trabecular bone. By carefully manipulating the infill density (controlled porosity) and print temperatures, the tensile strength and tensile modulus can be tailored to match the trabecular bone properties. This highlights the potential of the FFF of developed H/BAG feedstock to produce patient-specific implants.

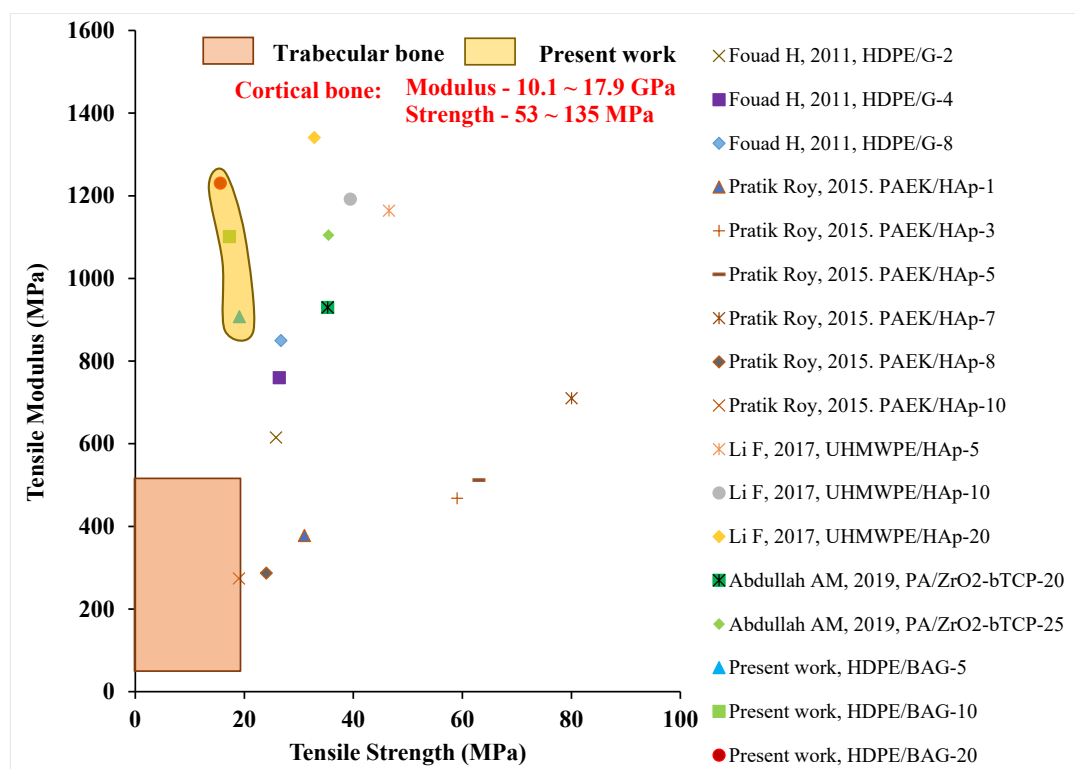


Figure 5.4. Tensile properties of the developed composites are compared with properties of biocompatible composites from the available studies.

5.4 Conclusions

Tensile properties of the developed neat H and H/BAG composites are experimentally investigated. The obtained results are compared with the properties of trabecular bones for potential implant fabrication. Results are summarized as follows:

- Tensile modulus increases with BAG addition. H₂₀ samples display 1.82 times higher modulus than near H samples.

- Ultimate tensile strength decreases with BAG addition. H₂₀ shows a 12.9% reduced ultimate tensile strength compared to neat H samples.
- The fracture strength of the samples increases with BAG addition. And H₂₀ samples exhibit 1.48 times higher fracture strength than neat H samples.
- Printed neat H and H/BAG samples exhibit 1.09, 1.26, 1.19, and 1.27 times better modulus than the respective filament feedstock. The printed neat H samples display a 26% higher modulus than injection moulded samples.
- The tensile strength of the developed composites is comparable to trabecular bone's tensile strength. Whereas the tensile modulus of the H/BAG composite is found to be higher than trabecular bone.
- Properties of the developed H/BAG composites can be tailored via controlled porosity to mimic the tensile properties of the trabecular bone. This shows the feasibility of developing patient-specific H/BAG implants.

6 FLEXURAL PROPERTIES

6.1 Flexural properties of neat H and H/BAG composites

Flexural behaviour of the developed neat H and H/BAG feedstock are studied to evaluate the rigidity of the materials. The representative stress-strain curve is presented in Figure 6.1. The test is concluded at 10% strain as the samples did not show failure indication. There are no detectable macroscopic fractures on the samples at the end of the test. Figure 6.1 shows the yielding of the prints under a flexural load, resulting in improved flexural properties with the filler addition (Table 6.1). Flexural modulus increases linearly with the addition of the BAG. H₂₀ samples display 1.45 times higher modulus among the composites than neat H samples. Similarly, flexural strength also increases linearly with filler addition. H₂₀ samples show 1.20 times higher strength than neat HDPE print. The printed neat H samples show 1.85 times higher flexural modulus when compared with the injection-moulded counterpart. The flexural strength of the neat H samples is comparable to that of injection moulded counterparts (Bharath Kumar et al. 2016).

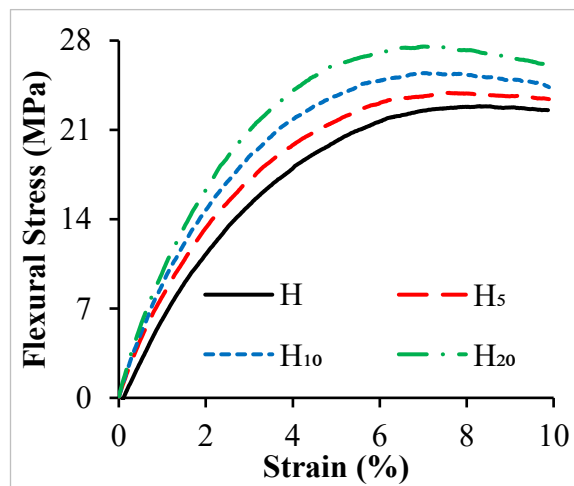


Figure 6.1. Flexural response of the printed samples.

Table 6.1. Flexural properties of the printed samples.

Samples	Modulus (MPa)	Strength (MPa)
H	774.24 ± 11.20	22.87 ± 0.34
H ₅	945.59 ± 11.73	23.90 ± 0.33
H ₁₀	1050.12 ± 13.11	25.74 ± 0.30
H ₂₀	1121.37 ± 15.12	27.53 ± 0.32

6.2 Micrographic analysis

Flexural samples after the flexural testing are freeze fractured using liquid nitrogen as the samples did not show any macroscopic fractures. The fractured samples are subjected to electron microscopy to understand the failure mechanism, which aids in better designing the components. The semi-crystalline HDPE matrix undergoes shrinkage upon cooling after printing. Thereby BAG particles are completely entrapped and squeezed into the matrix. This leads to circumferential compressive stress around the H/BAG interface. Thus, the developed Hoop stress acts as a stress concentrator and prevents crack propagation by inducing the surrounding HDPE to yield and absorb more strain energy (Paspali et al. 2018). The absence of BAG as stress concentrators in neat H samples leads to zero resistance when applied flexural load. Figure 6.2a shows unrestricted propagation of applied strain energy resulting in the least flexural modulus and strength. The freeze fractured post flexural test of H₂₀ sample (Figure 6.2b) shows homogeneous BAG distribution with no agglomerates. Such BAG as stress concentrators resists the applied strain energy resulting in enhanced flexural modulus and strength.

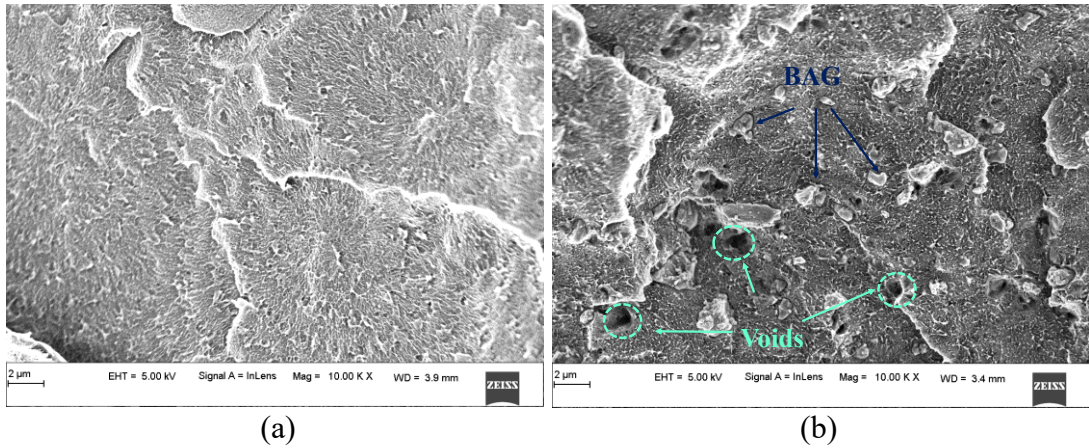


Figure 6.2. Micrography of the freeze fracture post flexural (a) neat H and (b) H₂O samples.

6.3 Property map

Flexural strength and flexural modulus of various biocompatible thermoplastic polymer composites reinforced with various bioactive fillers are plotted against each in Figure 6.3 (Ang et al. 2007, Dahl et al. 2018, Fouad and Elleithy 2011, Jaggi et al. 2012, Kaur et al. 2019, Keothongkham et al. 2017, Li et al. 2017, Maroulakos et al. 2019, Martin et al. 2019, Roy and Sailaja 2015, Senatov et al. 2016, Shuai et al. 2013, Wang et al. 2016, Wang et al. 2015). The information is extracted from the published literature on composites processed via conventional manufacturing processes and compared with the present study's results. The developed H/BAG composites are compared with composites of conventionally manufactured HDPE, PAEK, and PA composites. It is observed from Figure 6.3 that the flexural strength of the developed composites is lower than the other particulate reinforced composites. However, the tensile modulus of the developed BAG composites is comparable with HDPE, PAEK, and PA based composites.

The primary objective of the developed feedstock is to be used as implant materials. Hence, the obtained properties are compared with the properties of the human bone. The properties of the cortical bone are higher than the trabecular bone owing to its inherent degree of porosity (Figure 6.3). Hence, the properties of the developed composites are also compared with trabecular bone properties. These trabecular bones exhibit flexural strength and modulus in the range of 1 ~ 22 MPa and 50~570 MPa,

respectively (Kaur et al. 2019). It can be observed from the property map (Figure 6.3) that the flexural strength of the developed composites is in close range of that of the trabecular bone. Whereas flexural modulus is higher than trabecular bone. By carefully manipulating the infill density (controlled porosity) and print temperatures, the flexural strength and modulus can be tailored to match the trabecular bone properties. This highlights the potential of the FFF of developed H/BAG feedstock to produce on-demand patient-specific implants.

6.4 Conclusions

Flexural properties of the developed neat H and H/BAG composites are experimentally investigated. The obtained results are compared with the properties of trabecular bones for potential implant fabrication. Results are summarized as follows:

- The flexural modulus of the composites is higher than the neat H samples. H₂₀ shows 1.45 times higher modulus than neat H samples.
- Flexural strength increases with an increase in BAG addition. H₂₀ shows 1.20 times higher strength than neat H samples.
- The printed neat H samples show 1.85 times higher flexural modulus when compared with the injection-moulded counterparts.
- The flexural strength of the developed composites is comparable with the flexural strength of trabecular bone. In contrast, the flexural modulus of the H/BAG composite is found to be higher than trabecular bone.
- Properties of the developed H/BAG composites can be tailored via controlled porosity to mimic the flexural properties of the trabecular bone. This shows the feasibility of developing on-demand patient-specific H/BAG implants.

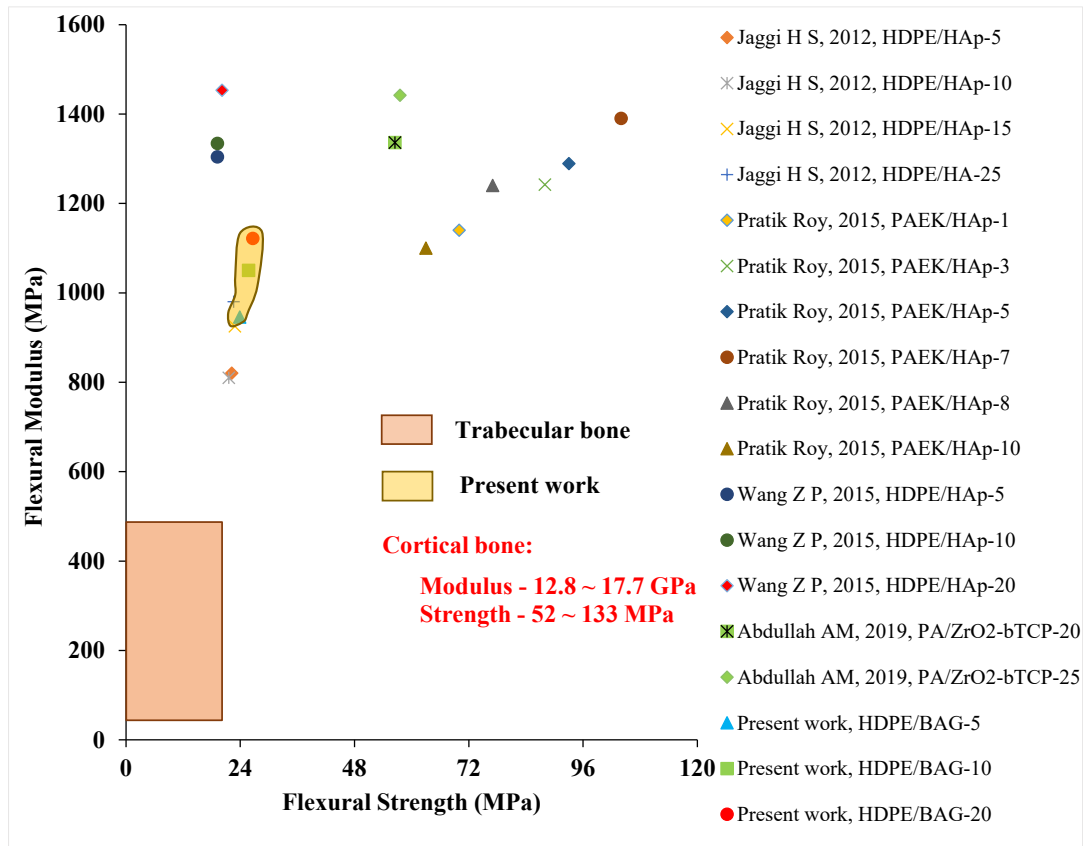


Figure 6.3. Flexural properties of the developed composites are compared with properties of biocompatible composites from the available studies.

7 COMPRESSION PROPERTIES

7.1 Compression properties of neat and H/BAG composites

The primary direction of load on most orthopaedic implants (craniomaxillofacial, spine cage, etc.) is compression in nature. Therefore, it is crucial to ascertain the compression behaviour of developed H/BAG composites. The compressive response of the neat H sample is displayed in Figure 7.1. Typically, the deformation behaviour of particulate reinforced thermoplastic samples under compression load is grouped into three distinct regions (Figure 7.1) (Jayavardhan and Doddamani 2018). Region I defines the initial linear elastic zone combined with non-linear global yielding. The large deformation under high plateau stress is characterized by region II. Region III signifies the densification with rapid stress rise resulting in unloading/fracture of the sample (Bharath Kumar et al. 2016, Jayavardhan and Doddamani 2018).

In region I, it is observed that the compressive stress increases with an increase in strain, and elasticity appears at a very low strain. The compressive modulus is calculated from this linear region. Deformation in the elastic region is homogeneous. The initial elastic region is followed by a distinct knee identified by a small positive slope, which is used to calculate the compressive yield strength. Densification stress and strain are calculated from region III. The present study analyzes compression behaviour for static and quasi-static conditions to better understand the developed H/BAG feedstock for biomedical applications.

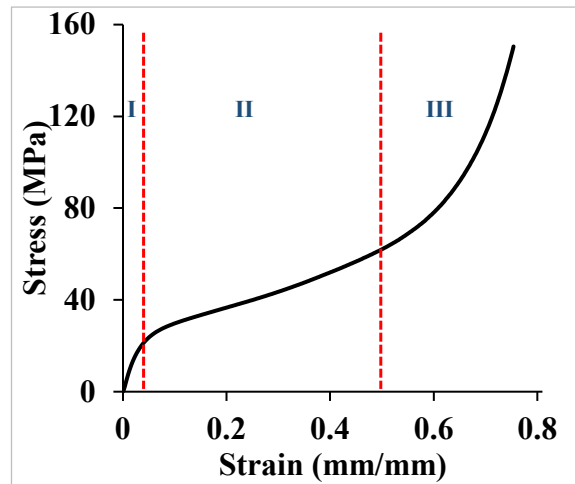


Figure 7.1. Schematic of stress-strain response of neat H samples showing three distinct regions (I - elastic, II - plateau and III – densification regions).

7.2 Static compression

The compressive response of the printed samples is presented in Figure 7.2. It is observed that the responses of the neat H and H/BAG composites follow a similar trend, and all samples withstood the maximum load of 20 kN without any macroscopic fracture. Various compression responses are documented in Table 7.1. Compressive properties follow the same trend as that flexural properties. Compressive modulus tends to increase linearly with the addition of BAG. H₂₀ samples show a 22.87% increased modulus than its neat H counterpart. Similarly, the compressive strength of the developed H/BAG composites increased linearly with BAG addition. H₂₀ samples show 18.04 % higher compressive strength than their neat H counterparts. Yield strain reduces linearly with the BAG addition. H₂₀ registered a 41.80% reduced yield strain compared to neat H samples. Energy absorption of the developed composites improved with BAG addition. H₂₀ exhibited 1.18 and 1.05 times better energy absorption than H₅ and neat H samples, respectively. Densification stress and its corresponding strain depend on matrix porosity collapse. Porosity increases with filler addition, leading to a decrease in densification strain. H₂₀ samples exhibit a 4% reduced densification strain than H₅ samples.

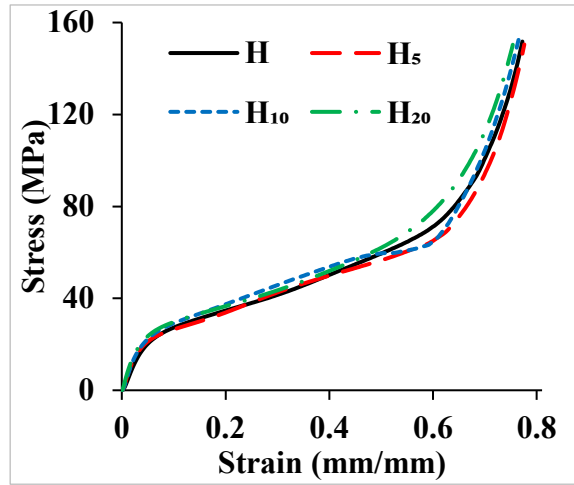


Figure 7.2. Compressive response of printed samples.

Table 7.1. Compressive properties of printed samples.

Samples	Modulus (MPa)	Strength (MPa)	Yield strain (%)	Energy absorption to 40% strain (MJ/m ³)	Densification stress (MPa)	Densification strain (MPa)
H	519.63 ± 9.87	22.34 ± 0.44	5.12 ± 0.94	16.88 ± 0.30	-----	-----
H ₅	546.82 ± 10.39	23.67 ± 0.46	4.45 ± 0.82	14.62 ± 0.26	63.08 ±1.24	58.98 ±1.13
H ₁₀	597.27 ± 11.35	25.12 ± 0.41	3.52 ± 0.65	15.54 ± 0.27	62.1 ±1.22	58.19 ±1.12
H ₂₀	638.49 ± 12.13	26.37 ± 0.51	2.98 ± 0.55	17.77 ± 0.32	70.86 ±1.40	56.6 ±1.09

7.2.1 Micrography analysis

All the samples underwent macroscopic ductile deformation without any visible brittle fracture. Hence, the samples after compression tests are freeze fractured using liquid nitrogen to carry out micrography. The fractured samples are subjected to electron microscopy to understand the failure mechanism, which aids in better designing of the components.

The yielding behaviour of HDPE is attributed to the deformation of the entangled network set up by high internal viscosity leading to inter and intra-laminar shear processes (Fan and Wang 2018, Omar et al. 2012, Ponnamma et al. 2019). This

phenomenon leads to enlarged voids and elongated fibrils, as depicted in Figure 7.3a. These voids will continuously grow under the applied load. This local deformation corresponds to the region I. This ductile deformation (in elongating the voids) forbids crack formation. Instead, it leads to the formation of fibrils (Figure 7.3a), which eventually becomes slender before rupture (Figure 7.3b, c). The elongation of the fibrils indicates the crosslink microstructure of the polymer chain (Fan and Wang 2018).

After yielding, the plateau region results from plastic collapse through axial and lateral shear (Region II). This indicates that even after the material lost its structural integrity, it still can withstand higher loads resulting in increased stress. The dense wrinkle structure formed in the matrix supports energy absorption by transmitting the stress locally (Figure 7.3a). Thus, the localized stress/strain is relaxed by ductile deformation inducing matrix softening post yielding (Fan and Wang 2018, Ponnamma et al. 2019). This is the underlying cause of long deformation strain under plateau stress. Macroscopic extended straining accompanied by the microscopic extension of fibrils is correlated to region II. The densification region (Region III) begins at the end of the plateau region, which is characterized by a sharp rise in stress. As the strain increases, the sample undergoes extensive deformation without any macroscopic fracture leading to peak stress. Under compression load, internal friction generally rearranges the whole lamellar structure, followed by breaking the formed lamellar structure. This leads to the formation of fibrils, followed by disentanglement, which ultimately leads to fracture (Fan and Wang 2018). Figure 7.3d correlates the formation of deformation bands in the direction of ductile elongation. The fracture of deformation bands occurs when the local tensile stress/strain is sufficient to facilitate crack propagation in the direction perpendicular to ductile elongation. These cracks are brittle with accelerated propagation (Figure 7.3d, e). Thus, the ductile deformation under high plateau stress is transitioned into microscopic brittle failure accompanied by rapid crack propagation and is attributed to region III (Figure 7.3f). A considerable amount of energy is absorbed during this transition and can be estimated from the area under region II. (Jayavardhan and Doddamani 2018, Omar et al. 2012). The formation of well-developed crazes during this transition aids in dissipating more strain energy (Figure 7.3d, e). Thus, the developed crazes increase the damage range by toughening the

polymer composite resulting in an improved strain energy absorption. Figure 7.3e shows the H/BAG interaction under extensive compressive loading.

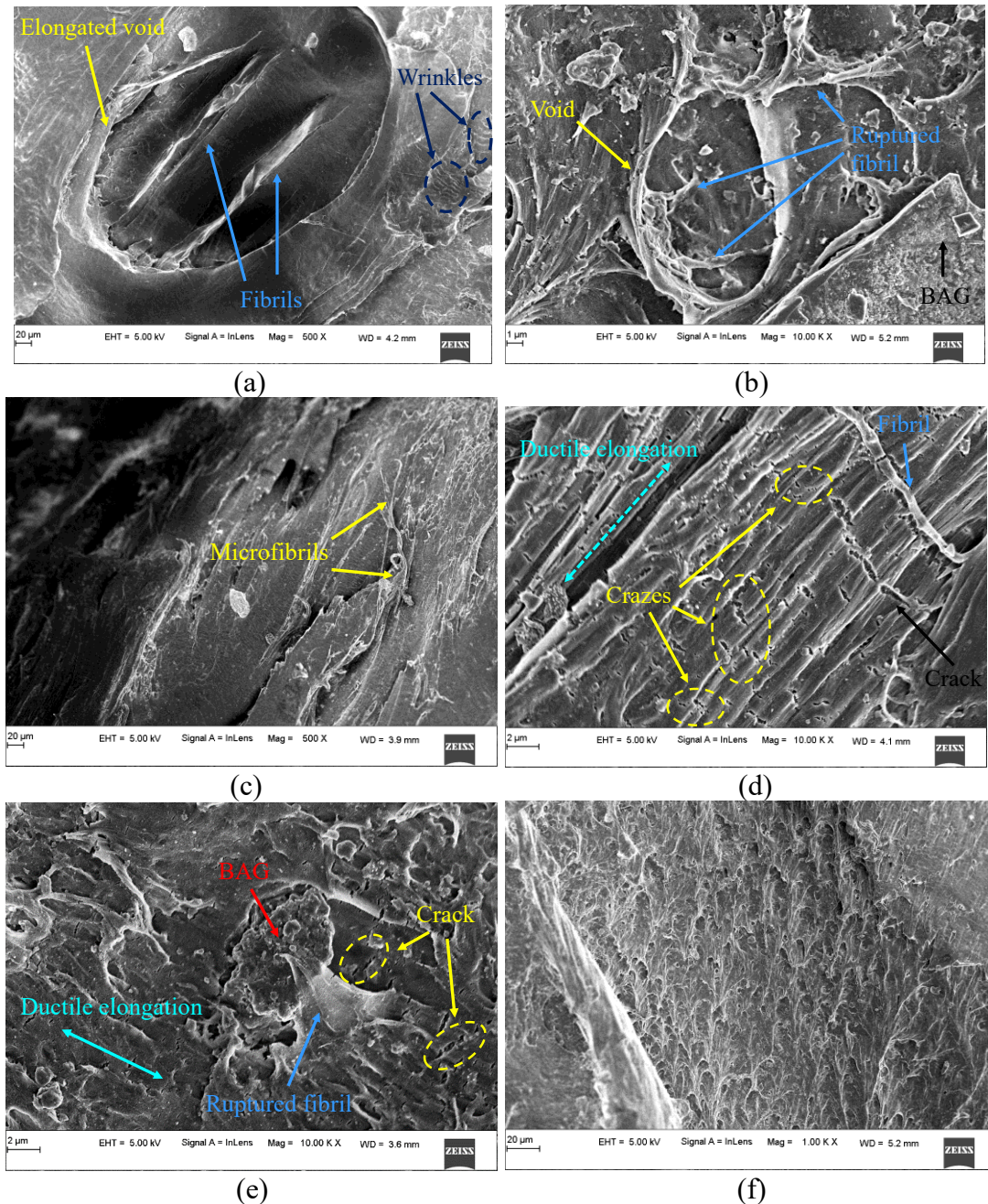


Figure 7.3. Micrography showing ductile damage under compression load: (a) fibril formation and void elongation of neat H sample (Region – I), (b) ruptured fibrils due to void elongation of H₅ samples, (c) slender microfibril of H₁₀ sample (Region – I), formation crazes and crack propagation normal to the elongation direction of (d) neat H and (e) H₂₀ sample (Region – II), and (f) severe plastic collapse of H₂₀ sample (Region – III).

7.2.2 Property map

Compression strength and compression modulus of various biocompatible thermoplastic polymer composites reinforced with various bioactive fillers are plotted against each in (Figure 7.4) (Ang et al. 2007, Dahl et al. 2018, Fouad and Elleithy 2011, Jaggi et al. 2012, Kaur et al. 2019, Keothongkham et al. 2017, Li et al. 2017, Maroulakos et al. 2019, Martin et al. 2019, Roy and Sailaja 2015, Senatov et al. 2016, Shuai et al. 2013, Wang et al. 2016, Wang et al. 2015). The information is extracted from the published literature on composites processed via conventional manufacturing processes and compared with the present study's results. The developed H/BAG composites are compared with composites of conventionally manufactured PCL, PLGA, PLA, and PCL-PVA based composites. It is observed from Figure 7.4 that the compression modulus strength of the developed composites is higher than the other particulate reinforced composites.

The primary objective of the developed feedstock is to be used as implant materials. Hence, the obtained properties are compared with the properties of the human bone. The properties of the cortical bone are higher than the trabecular bone owing to its inherent degree of porosity (Figure 7.4). Hence, the properties of the developed composites are also compared with trabecular bone properties. These trabecular bones exhibit compression strength and modulus in the range of 1 ~ 8 MPa and 50 ~ 600 MPa, respectively (Kaur et al. 2019). It can be observed from Figure 7.4 that the compression strength and modulus of the developed composites are higher than trabecular bone. By carefully manipulating the infill density (controlled porosity) and print temperatures, the compression strength and modulus can be tailored to match the trabecular bone properties. This highlights the potential of the FFF of developed H/BAG feedstock to produce patient-specific implants.

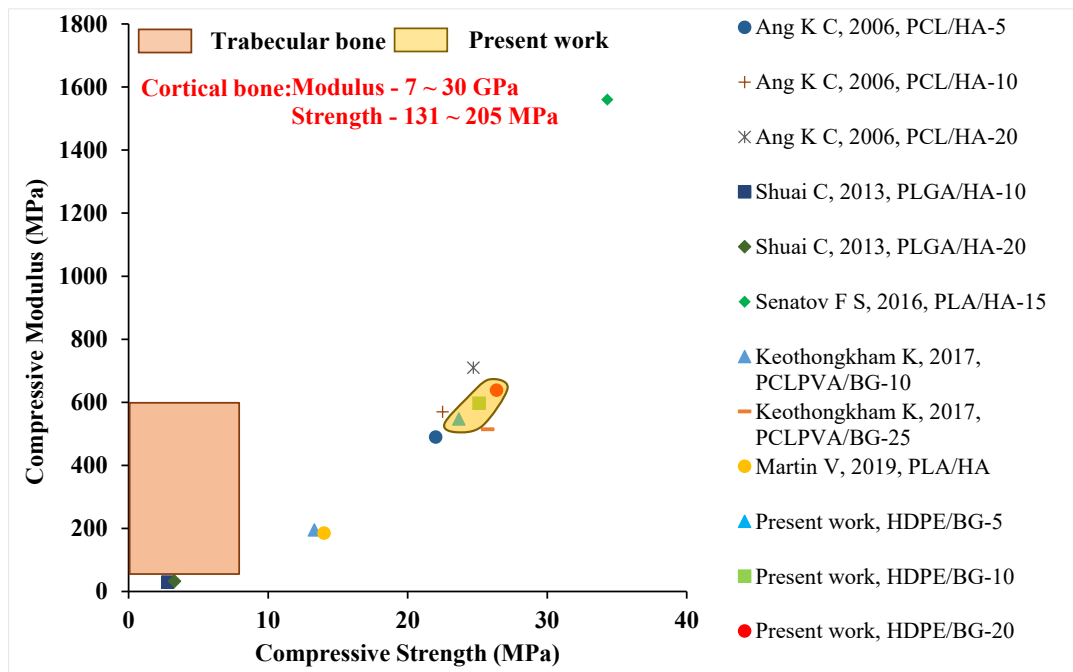


Figure 7.4. Compressive properties of the developed composites are compared with properties of biocompatible composites from the available studies.

7.3 Quasi-static compression

Figure 7.5 illustrates the quasi-static compression behaviour of the developed neat H and H/BAG composites at the strain rates of 0.001, 0.01, and 0.1 s^{-1} . Table 7.2 lists the test results at various strain rates. The concomitant higher elastic modulus of BAG makes it to act like stress concentrators leading to increased modulus and yield strength of the composites. This trend is similar to the increase in strain rate as well. H₂₀ samples at a 0.1 s^{-1} strain rate exhibit 1.17 and 1.25 times higher modulus and yield strength than the corresponding H₂₀ sample at a 0.001 s^{-1} strain rate. At increased strain rates, the time available for the HDPE lamellar to rearrange is restricted, leading to decreased yield strain. Yield strain is decreased with an increase in BAG, highlighting the reduction in the proportion of HDPE to undergo deformation. Neat H samples at 0.001 s^{-1} strain rate show 18.46 and 39.61% higher yield strain when compared with H₂₀ samples at 0.001 s^{-1} and neat H samples at 0.1 s^{-1} strain rate, respectively. Addition of stiffer BAG results in decreased energy absorption of composites. At 0.001 s^{-1} strain rate, the energy absorption of neat H is 13.50% higher than H₂₀ samples. Energy absorption increases with an increase in strain rate. Energy absorption of neat H at 0.001 s^{-1} strain rate is 14.47% lower than its value at 0.1 s^{-1} strain rate. As mentioned earlier,

an increase in BAG content reduces the HDPE portion available for deformation, and an increase in strain rate results in limited time for HDPE lamellae to rearrange. Such conditions lead to decreased densification strain with increasing BAG content and strain rate (Kumar et al. 2016, Omar et al. 2012). At 0.001 s^{-1} , the neat H sample shows an 8.51% greater densification strain than H₂₀ samples. The densification strain of neat H at 0.001 s^{-1} strain rate is 13.96% lower than its value at 0.1 s^{-1} strain rate.

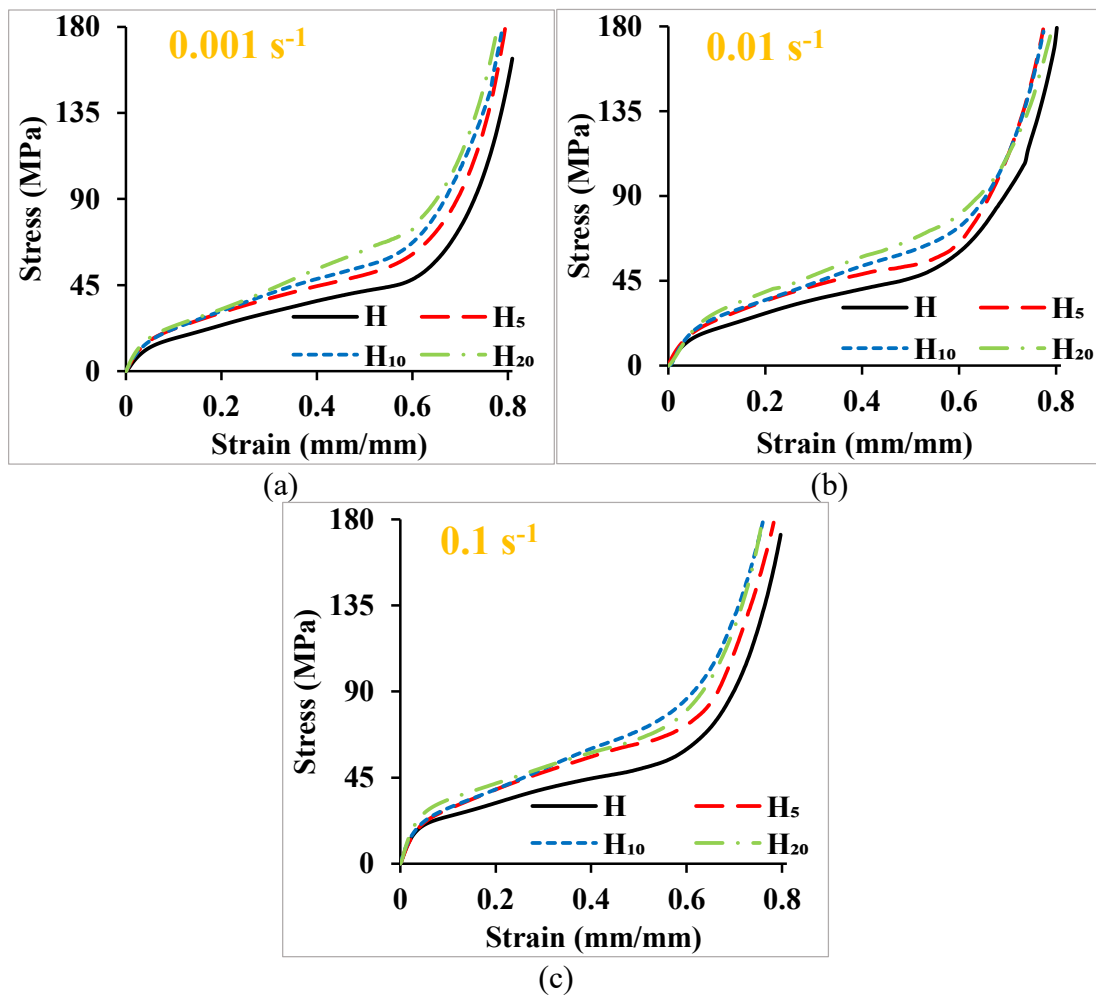


Figure 7.5. Representative stress-strain plots at different strain rates of (a) 0.001 , (b) 0.01 , and (c) 0.1 s^{-1} .

7.3.1 Micrographic analysis

The samples show a similar level of strains (Figure 7.5), and deformation features of the samples at different strain rates appear identical as the tests are performed in quasi-static conditions.

Figure 7.6a shows the compression sample before testing, and Figure 7.6b shows the symmetric barrelling of the post-compression sample. The effective dissipation of the compression loads leads to homogeneous deformation without cracking and fragmentation of the samples (Liu et al. 2020). Such structural integrity signifies the load-bearing capacity of the developed feedstock. This indicates the selection of proper printing parameters resulting in zero print induced defects (Doddamani 2020, Jeyachandran et al. 2020). Under compression loading, secondary tensile stresses are developed perpendicular to applied loading, resulting in shear-barrelling of the samples, and subsequent shear bands are formed (II) (Swetha and Kumar 2011). The deformed samples are polished to a mirror finish in the transverse and longitudinal directions (Figure 7.6c, d) to visualize the formed shear bands under an OM. Figure 7.6c, d show that the shear bands have originated at the center of the sample and progressed along the propagation direction towards the edges. In-sets of Figure 7.6c show the multiple branching of the transverse shear bands due to compressive stress along the propagation direction, leading to flow serrations. Such serrations indicate the transition of formed shear bands into cracks. Crazes are formed as a preventive measure to dissipate more energy to restrict microcrack initiation and propagation, leading to failure of samples (Figure 7.7f). Voids formed along the exterior contour of the samples (Figure 7.6d) are a result of cleaved chemical bonds of the matrix indicating a higher degree of deformation (Smith et al.).

Furthermore, tested samples are freeze fractured in the transverse and longitudinal direction to elucidate the different deformation features. Figure 7.7a, b show the fractured neat H and H₂₀ samples along the longitudinal direction. Neat H sample (Figure 7.7a) shows multiple wrinkles, aiding in enhanced energy absorption under compression loading (Omar et al. 2012). Brittle fractured surfaces (Figure 7.7a) indicate failure of the amorphous HDPE region as the crystalline portion is responsible for ductile deformation (Jayavardhan and Doddamani 2018). Figure 7.7b shows the formation of HDPE fibrils as the stiffer BAG restricts the flow of the HDPE under compression loading. No visible cracks are a clear indication of the ductile deformation under applied compressive loading. Ductile deformation is evident from the micrographs taken along the transverse direction (Figure 7.7c - f). In region II, energy

absorption is accomplished through void elongation, leading to the formation, extension, and rupturing of fibrils (Figure 7.7e). Such ductile elongation leads to the formation of ductile deformation bands (Figure 7.7d) along the elongation direction to delay crack initiation and propagation (Jeyachandran et al. 2020, Omar et al. 2012). High compliance and insufficient interlaminar adhesion led to the micro buckling of the HDPE matrix under compression in the transverse direction (Figure 7.7e). Such buckling deformation avoids the fatal failure of the samples (Iragi et al. 2019).

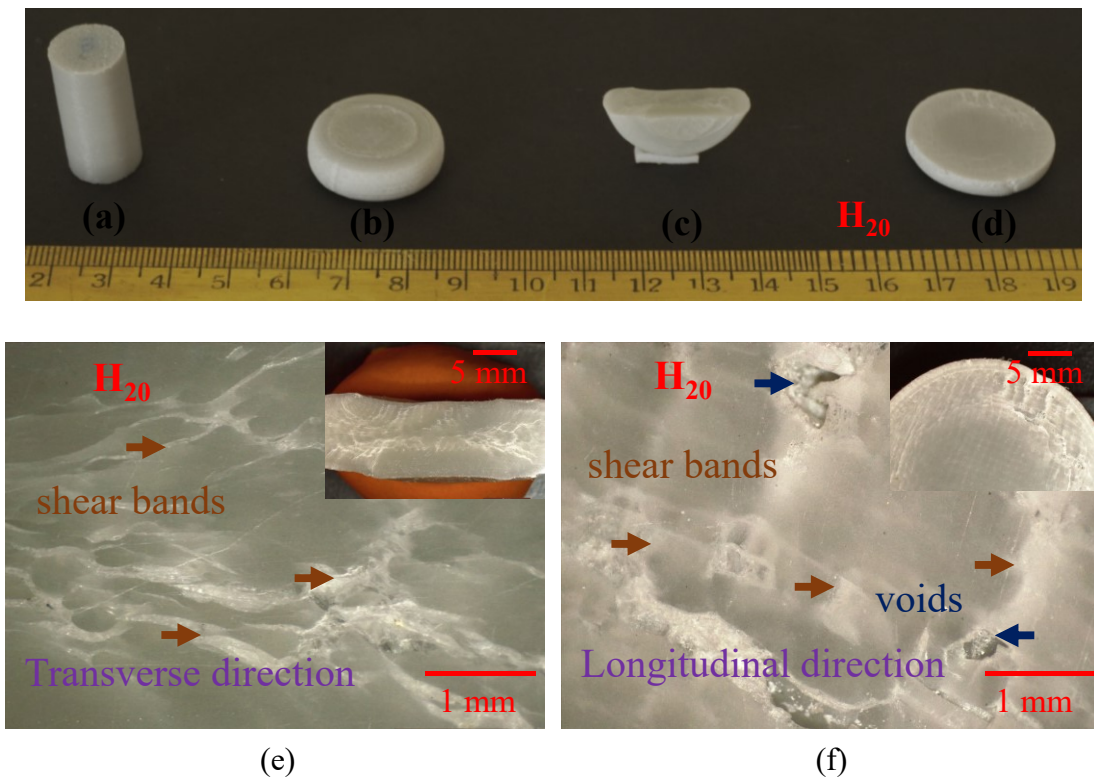


Figure 7.6. Compression sample (a) before the test and (b) showing barrelling effect – after the test. Polished H₂₀ post-compression samples in (c) transverse and (d) longitudinal directions. Optical micrography of polished post-compression samples showing shear bands (e-f).

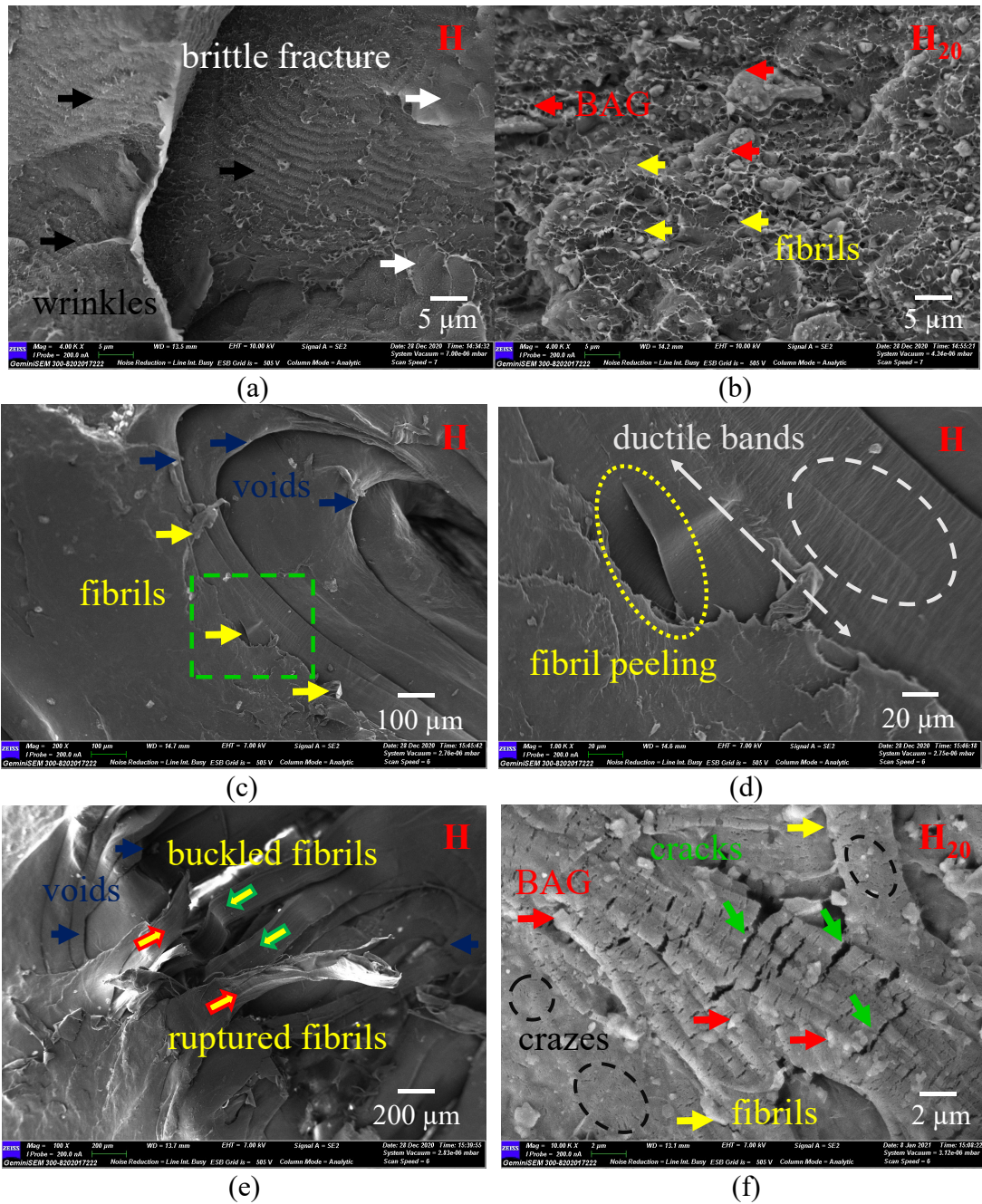


Figure 7.7. Micrography showing various features under compression load (a) wrinkles and brittle fracture, (b) HDPE fibrils and stiffer BAG, (c) void elongation and fibril formation, (d) fibril peeling, ductile bands and elongation direction at higher magnification (e) voids, ruptured and buckled fibrils and (f) craze formation and crack propagation

Table 7.2. Quasi-static compression behaviour of printed samples at 0.001, 0.01 and 0.1 s⁻¹.

Strain rate (s ⁻¹)	Sample	Modulus (MPa)	Yield strength (MPa)	Yield strain (%)	Energy absorption at 40% strain (MJ/m ³)	Densification stress (MPa)	Densification strain (MPa)
0.001	H	505.32±11.11	16.09±0.36	5.58±0.15	17.11±0.48	42.46±0.97	58.35±1.23
	H ₅	571.73±11.32	20.39±0.46	5.22±0.11	17.91±0.43	54.59±1.27	55.61±1.05
	H ₁₀	622.27±15.06	20.97±0.38	5.17±0.14	18.75±0.49	62.62±1.69	54.37±1.20
	H ₂₀	671.80±12.79	22.12±0.42	4.55±0.12	19.78±0.44	60.14±1.84	52.67±1.52
0.01	H	580.86±13.39	17.29±0.19	4.31±0.05	17.83±0.28	55.00±1.10	53.17±1.17
	H ₅	613.14±18.43	21.03±0.42	4.28±0.08	18.54±0.36	62.57±1.28	51.99±1.25
	H ₁₀	654.92±12.44	21.98±0.46	4.12±0.08	19.29±0.21	66.44±1.31	49.67±1.32
	H ₂₀	718.27±15.12	24.90±0.43	3.98±0.10	20.34±0.45	64.85±1.39	48.18±1.07
0.1	H	663.00±11.94	21.93±0.47	3.37±0.07	18.09±0.49	57.09±1.71	51.2±1.13
	H ₅	709.11±14.18	23.07±0.35	3.05±0.06	19.84±0.48	71.75±1.51	49.36±1.09
	H ₁₀	749.72±18.74	23.85±0.48	2.95±0.06	21.79±0.31	70.00±1.54	49.33±1.21
	H ₂₀	782.95±14.08	27.61±0.56	2.54±0.06	22.64±0.67	68.00±2.04	46.84±0.92

7.4 Conclusions

Compression properties (static and quasi-static) of the developed neat H and H/BAG composites are experimentally investigated. The results of static compression tests are compared with the properties of trabecular bones for potential implant fabrication. Results are summarized as follows:

- All the samples exhibit the same levels of strain and similar deformation features irrespective of strain rate (static and quasi-static).
- Stress-strain curves are divided into three distinct regions to understand the deformation mechanism.
- The fractured surface shows brittle surface, wrinkles, fibrils (buckled, elongated, ruptured, peeled), voids, crazes, cracks, and ductile bands.

Static compression

- Compression strength and modulus increase with BAG addition. H₂₀ samples show 18.04 and 22.87 % higher compression strength and modulus.
- Energy absorption of the developed composites improved with BAG addition. H₂₀ exhibited 1.18 and 1.05 times better energy absorption than H₅ and neat H samples, respectively.
- Densification strain decreases with BAG addition. H₂₀ samples exhibit a 4% reduced densification strain than H₅ samples.
- The compression strength and modulus of the developed composites are higher than the trabecular bone.

Quasi-static compression

- Compressive modulus and strength increase with BAG addition and strain rate. H₂₀ samples at a 0.1 s⁻¹ strain rate exhibit 1.17 and 1.25 times higher modulus and yield strength than the corresponding H₂₀ sample at a 0.001 s⁻¹ strain rate.
- Addition of stiffer BAG results in increased energy absorption of composites. At 0.001 s⁻¹ strain rate, the energy absorption of H₂₀ is 15.02% higher than neat H samples.

- Energy absorption increases with an increase in strain rate. Energy absorption at 0.001 s^{-1} is 14.47 % lower for neat H samples than its value at 0.1 s^{-1} strain rate.

Densification strain increases with BAG addition. Neat H samples show an 8.51% higher densification strain than H₂₀ samples at a 0.001 s^{-1} strain rate.

8 IMPACT TEST

8.1 Impact test

The impact characteristics of the developed feedstock are studied, and Figure 8.1 shows the impact strength of the printed samples. All the samples broke entirely during the test. The impact strength of the samples decreases with BAG addition (Table 8.1). H₂₀ samples exhibit 62.16 % reduced impact strength compared to neat H samples. The results agree with the previous studies on HDPE composites with particulate fillers (Awad et al. 2020, da Costa et al. 2007, Muniyandi et al. 2013). The added BAG fillers act as stress concentrators, and upon applying impact load, cracks will propagate quickly along with the poor H/BAG interface with less energy (Yang et al. 2016). This explains the enhanced stiffness (Jeyachandran et al. 2020) and reduced impact toughness of the developed H/BAG composites (Yang et al. 2016).

8.2 Micrography analysis

Fibrils indicate severe plastic deformation of neat H samples, which enhances effective dissipation of applied impact energy (Wang et al. 2009), as seen in Figure 8.2a. Debonding of stiffer BAG from the matrix, development of micro-voids along the interface, and local plastic deformation of HDPE matrix surrounding BAG are observed in Figure 8.2b. This leads to a decrease in the impact toughness of the developed H/BAG composites.

8.3 Conclusions

- Addition of BAG results in enhanced stiffness of the H/BAG composites.
- The impact strength of the samples decreases with the addition of BAG, and H₂₀ samples show 62.16% reduced impact strength.
- Insufficient adhesion between H and BAG favours swift propagation of cracks leading to localized plastic deformation followed by micro-voids' development.

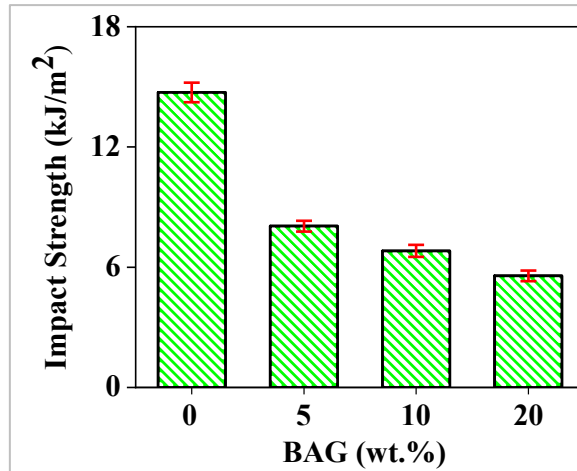


Figure 8.1. Impact strength of printed samples.

Table 8.1. Impact strength and % reduction in impact strength of printed samples.

Sample	Impact strength (kJ/m ²)	% reduction wrt neat H
H	14.72 ± 0.47	-
H ₅	8.05 ± 0.26	45.31
H ₁₀	6.82 ± 0.30	53.67
H ₂₀	5.57 ± 0.26	62.16

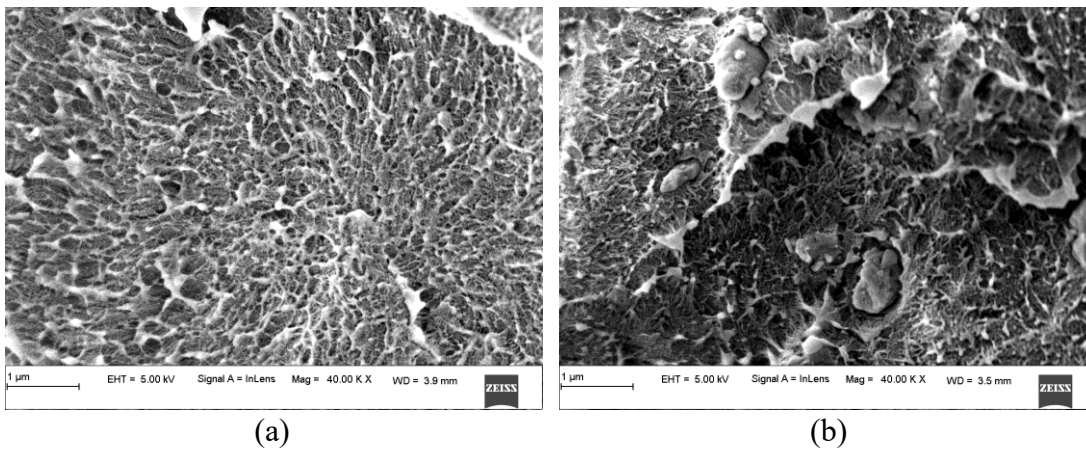


Figure 8.2. Micrographs of fractured (a) neat H and (b) H₂₀ samples.

9 DYNAMIC MECHANICAL ANALYSIS

9.1 Temperature sweep

The reinforcing effect of BAG particles is evaluated by studying storage modulus, loss modulus, and damping factor concerning temperature and frequency (Figure 9.1 and Figure 9.2). The analysis is carried out for the temperature range of 28 – 120 °C at 1 and 10 Hz. Table 9.1 and Table 9.2 show storage modulus, loss modulus, and damping factor values at three reference temperatures 40, 80, and 120 °C for 1 and 10 Hz, respectively. The glass transition temperature (T_g) of HDPE is around -110 °C. Therefore, the current analysis is carried out entirely in the rubbery region. This results in dynamic curves with no peaks indicating phase transitions (Doddamani 2020, Zeltmann et al. 2016).

Storage modulus characterizes the elastic state of the samples, and it is found to be increasing with BAG addition (Figure 9.1a and Figure 9.2a). The increase in the stiffness of the samples with the addition of BAG leads to enhanced energy absorption resulting in higher storage modulus. The trend is similar for both 1 and 10 Hz. H₂₀ composite displays the highest storage modulus for the entire sweep range, signifying the reinforcing effect of BAG by restricting the HDPE mobility. At 1 Hz, H₂₀ samples exhibit 1.32, 1.38, and 1.90 times higher storage modulus than neat H samples at three reference temperatures. Similarly, at 10 Hz, H₂₀ samples exhibit 1.40, 1.52, and 2.15 times higher storage modulus than neat H samples at three reference temperatures. As the sweep temperature approaches the crystal T_m , the crystal phase restricting the segmental motion of the amorphous phase diminishes. This phenomenon is attributed to the decrease in E' with increasing sweep temperature. The storage modulus of H₂₀ is reduced by 84.88 and 84.03 % with the increase in temperature from 40 to 120 °C at 1 and 10 Hz, respectively.

Loss modulus signifies the capacity of the samples to dissipate energy. Figure 9.1b and Figure 9.2b show that the loss modulus of the samples increases till a specific temperature (~45 – 50 °C) and starts decreasing with a further increase in temperature. The obtained peak signifies α - relaxation of the HDPE polymer, which leads to the

formation of an amorphous phase at the expense of crystallinity (Zeltmann et al. 2016). H/BAG samples exhibit higher loss modulus at all temperatures and increase with BAG addition. At 1 Hz, H₂₀ samples display 1.15, 1.18, and 1.64 times higher loss modulus than neat H samples at three reference temperatures. Similarly, at 10 Hz, H₂₀ samples display 1.14, 1.32, and 1.80 times higher loss modulus than neat H samples at three reference temperatures. The loss modulus of H₂₀ is reduced by 75.41 and 72.47 %, with an increase in temperature from 40 to 120 °C at 1 and 10 Hz, respectively.

The damping factor, $\tan \delta$ is the ratio of E'' and E' , signifying the material's relative spectrum of viscous and elastic nature. As the temperature increases, elastic nature disappears, and the viscous nature predominates the samples leading to an increase in $\tan \delta$ (Doddamani 2020, Zeltmann et al. 2016). The damping factor of H₂₀ samples is increased (Figure 9.1c and Figure 9.2c) 1.62 and 1.72 times, respectively, at 1 and 10 Hz as the temperature increased from 40 to 120 °C. However, the damping factor decreases with BAG addition due to restricted HDPE chain movement adding BAG. H₂₀ samples at 1 Hz display 12.87, 14.36, and 13.91 % decreased damping factor than neat H samples at three reference temperatures. Similarly, at 10 Hz, H₂₀ samples exhibit 19.03, 18.38, and 15.76 % decreased damping factor than neat H samples at three reference temperatures.

The mechanical integrity of the biomedical materials is essential as various loads like tensile, flexural, compression, torsional, shear, and buckling act inside the body during various instances. Especially viscoelastic properties depend on non-linear and time-dependent mechanical properties (Petersmann et al. 2020). To simulate the clinical condition, the average body temperature of 37 °C and physiological frequency of 1 and 10 Hz, which may be analogous to chewing, slow walking, and fast running, are selected (Barbieri et al. 2013, Chrysafi et al. 2020). E' , E'' and $\tan \delta$ of composites at 37 °C increases with an increase in BAG addition (Table 9.3). Furthermore, an increase in the damping factor with the addition of BAG exhibits the enhanced ability to dissipate energy which is essential for implant development (Liu et al. 2018, Paxton et al. 2019, Paxton et al. 2021, Petersmann et al. 2020). H₂₀ exhibits 1.28, 1.52, and 1.21 times

higher E' , E'' and $\tan \delta$ respectively than the neat H samples at 1 Hz. Similarly, E' , E'' and $\tan \delta$ of H₂₀ samples are 1.30, 1.40, and 1.08 times higher than the neat H samples, respectively, at 10 Hz. Thus, adding BAG to HDPE results in enhanced mechanical property at the selected clinical temperature.

9.2 Conclusions

The effect of temperature and BAG addition on the viscoelastic behaviour of the developed neat H and H/BAG feedstock composites are presented. Storage modulus, loss modulus, and damping factor are analyzed from the experimental results, and the following conclusions are drawn:

- Storage modulus increases with BAG addition, and H₂₀ samples display the maximum storage modulus.
- Storage modulus decreases with temperature for neat H and H/BAG composites. The deviation of storage modulus at increased temperature is in a tight range.
- The loss modulus of the H/BAG composites is higher than the neat H counterpart.
- Damping factor decreases with BAG addition due to restricted HDPE molecular mobility.
- The changes in the storage modulus, loss modulus, and loss factor with the increase in temperature below the melting point indicate the disappearance of crystal phases that restrict the mobility of the amorphous phase. This emphasizes the necessity of considering the temperature-dependent viscoelastic properties while designing the H/BAG implants.
- At a clinical temperature of 37 °C, storage modulus, loss modulus and loss factor is observed to increase with BAG addition highlighting the enhanced ability to dissipate energy.
- Such developed H/BAG composites with enhanced viscoelastic properties can be used as implants and scaffolds where stiffness and enhanced damping abilities play a significant role.

Table 9.1. Comparison of storage modulus, loss modulus and Tan δ of samples from temperature sweep at 1 Hz and three representative temperatures

Sample	E' (MPa)			E'' (MPa)			tan δ ($\times 10^{-2}$)		
	40 °C	80 °C	120 °C	40 °C	80 °C	120 °C	40 °C	80 °C	120 °C
H	1631.50 ± 29.367	581.70 ± 10.75	171.07 ± 3.25	186.35 ± 3.54	101.58 ± 1.93	32.11 ± 0.64	11.42 ± 0.003	17.46 ± 0.003	18.77 ± 0.004
H ₅	1864.36 ± 33.56	643.23 ± 12.30	195.23 ± 3.76	195.27 ± 3.71	106.74 ± 2.14	35.01 ± 0.71	10.47 ± 0.002	16.60 ± 0.006	17.93 ± 0.005
H ₁₀	2007.99 ± 36.14	717.11 ± 13.47	255.07 ± 4.84	206.63 ± 3.93	113.60 ± 2.22	43.34 ± 0.84	10.29 ± 0.002	15.84 ± 0.002	16.97 ± 0.003
H ₂₀	2144.54 ± 38.60	804.41 ± 15.78	324.31 ± 6.17	213.53 ± 4.05	120.26 ± 2.29	52.50 ± 1.02	9.95 ± 0.001	14.95 ± 0.005	16.16 ± 0.002

Table 9.2. Comparison of storage modulus, loss modulus and Tan δ of samples from temperature sweep at 10 Hz and three representative temperatures

Sample	E' (MPa)			E'' (MPa)			tan δ ($\times 10^{-2}$)		
	40 °C	80 °C	120 °C	40 °C	80 °C	120 °C	40 °C	80 °C	120 °C
H	1826.88 ± 32.44	656.22 ± 12.74	190.01 ± 3.11	221.57 ± 4.19	121.86 ± 2.84	38.58 ± 0.73	12.14 ± 0.21	18.38 ± 0.34	20.11 ± 0.40
H ₅	2124.47 ± 38.35	733.82 ± 13.22	220.62 ± 4.17	237.33 ± 4.22	130.74 ± 2.55	42.71 ± 0.87	11.20 ± 0.22	17.76 ± 0.33	19.35 ± 0.39
H ₁₀	2399.31 ± 42.22	835.45 ± 15.93	293.67 ± 5.49	254.65 ± 4.83	139.74 ± 2.75	55.31 ± 0.99	10.86 ± 0.27	16.73 ± 0.31	18.19 ± 0.36
H ₂₀	2560.74 ± 46.09	995.02 ± 18.33	408.79 ± 7.57	251.60 ± 4.79	161.34 ± 3.15	69.27 ± 1.29	9.83 ± 0.19	16.21 ± 0.30	16.94 ± 0.33

Table 9.3. Storage modulus, loss modulus and Tan δ at the physiological condition of 37 °C at 1 and 10 Hz

Sample	E' (MPa)		E'' (MPa)		tan δ ($\times 10^{-2}$)	
	1 Hz	10 Hz	1 Hz	10 Hz	1 Hz	10 Hz
H	1765.71 ± 34.44	1999.07 ± 38.99	159.77 ± 3.20	175.67 ± 3.57	8.60 ± 0.18	8.77 ± 0.18
H ₅	1924.41 ± 38.49	2320.92 ± 45.26	187.05 ± 4.12	217.43 ± 4.34	9.73 ± 0.20	9.32 ± 0.20
H ₁₀	1921.52 ± 40.36	2503.06 ± 48.81	218.05 ± 5.01	245.74 ± 4.94	11.36 ± 0.25	9.78 ± 0.21
H ₂₀	2254.54 ± 46.22	2505.12 ± 48.85	242.30 ± 5.82	247.54 ± 4.90	12.76 ± 0.31	9.85 ± 0.21

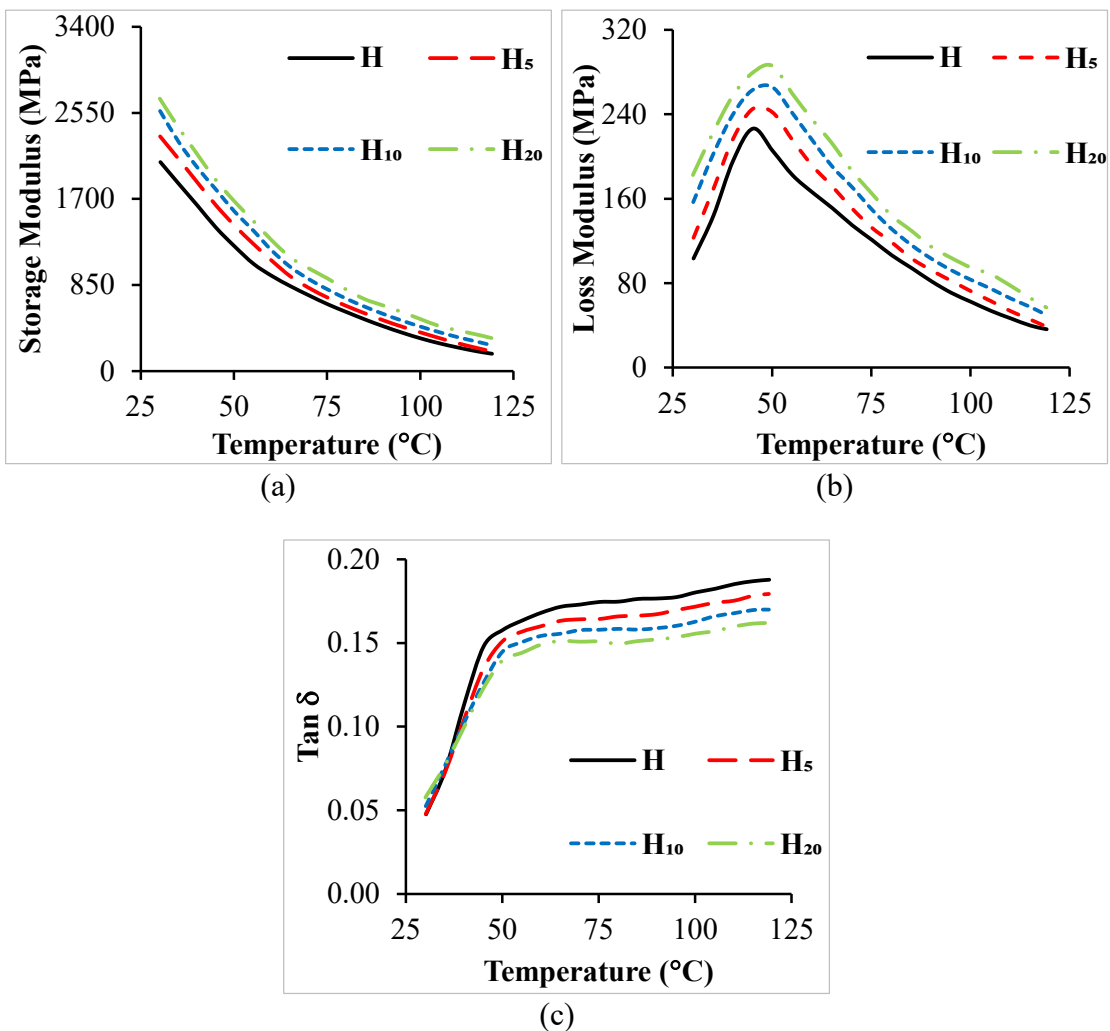


Figure 9.1. (a) Storage modulus, (b) loss modulus, and (c) Tan δ results from temperature sweep at 1 Hz.

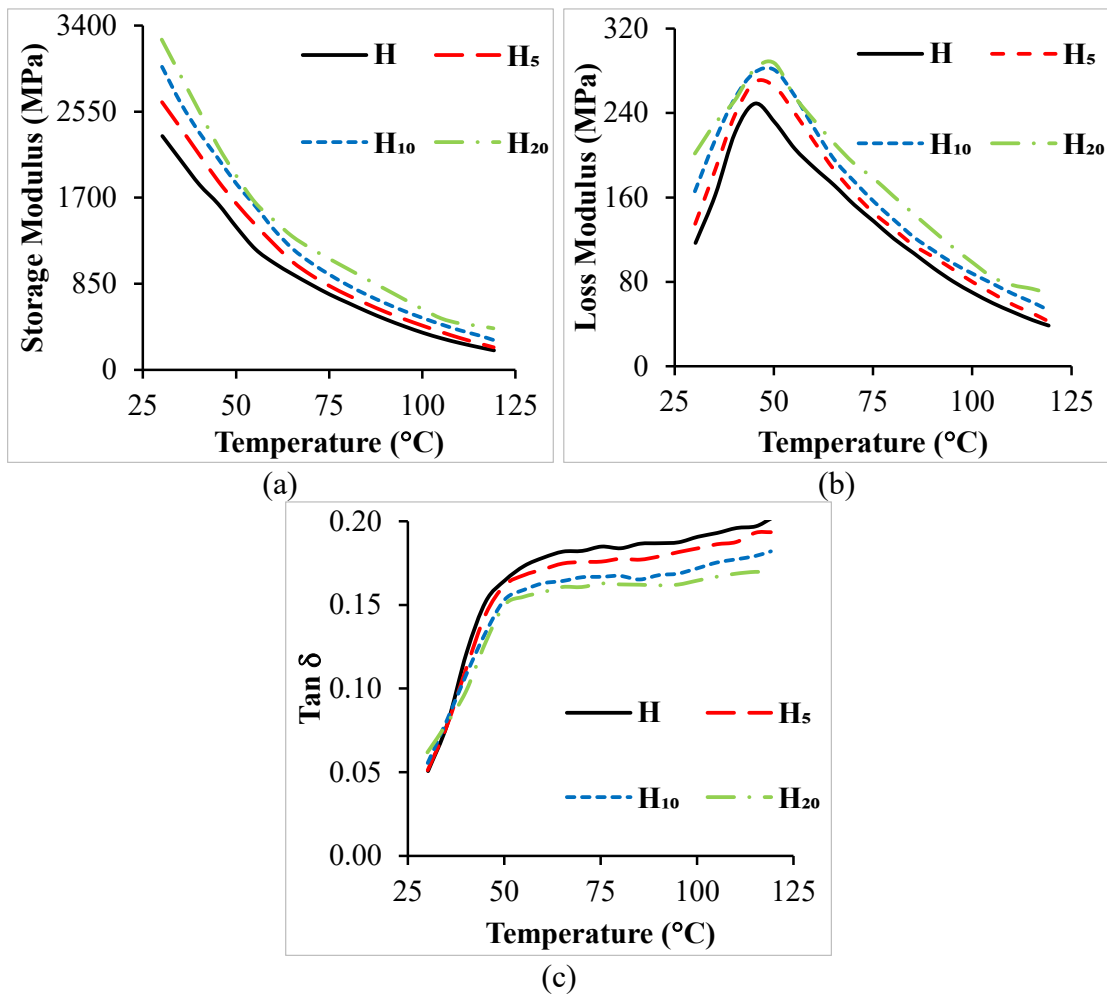


Figure 9.2. (a) Storage modulus, (b) loss modulus, and (c) Tan δ results from temperature sweep at 10 Hz.

10 SUMMARY AND CONCLUSIONS

10.1 Summary

Present work deals with developing BAG reinforced HDPE composite filament feedstock for the FFF process for possible fabrication of biomedical implants and scaffolds. BAG is known for controlled reactivity with bodily fluids. The innate brittleness of the BAG restricts its direct usage in load-bearing applications. The drawback can be overcome by developing BAG-based polymer composites to mimic bone properties for cranial and facial reconstruction. H/BAG composites containing 5, 10, and 20 wt.% of BAG are melt compounded using a twin-screw extruder. As received HDPE granules and composite blends are extruded into filaments to be used as feedstock for the FFF process. Extensive investigation is carried out to evaluate the printability of the developed filament feedstock and the effect of BAG reinforcement in HDPE matrix on the mechanical properties of printed samples.

The thermal degradation properties of the feedstock are studied to determine the processing temperatures for melt compounding, filament extrusion, and sample printing. Also, thermal and melt behaviours are studied to evaluate the printability of the developed filament feedstock. Characterizations such as TGA, DSC, XRD, MFI, CTE, and rheology are carried out to understand the behaviour of feedstock during printing. The printability of the developed feedstock is evaluated for print adhesion and print-induced defects such as warpage, inept diffusion, delamination, voids, underfill and overfill. Printing parameters such as T_p , T_e , T_b , LT, multiplier, and printing speed are optimized to yield dimensionally stable, defect-free samples.

The effect of BAG reinforcement on the mechanical properties of the printed samples is investigated. Tensile, flexural, and compression tests are carried out, and the obtained values are compared with the properties of other bio-composites. The feasibility of tailoring the properties is evaluated by correlating with the trabecular bone properties. Quasi-static compression behaviour is also studied to analyze the effect of various strain rates and BAG reinforcement. In addition, impact and DMA properties are studied.

10.2 Conclusions

The prime conclusions are summarized as follows:

Blend and filament characterization

- Micrography and elemental mapping of composite blends show homogeneous dispersion of BAG in HDPE matrix.
- The developed filament feedstock is circular in cross-section, and the average diameter is 1.75 ± 0.05 mm, which is well within the acceptable limit for printability.
- Density and void percentage increase with BAG addition. H₂₀ filaments show a 13.8% higher density than neat H filaments and 13.31 % porosity.
- The dispersion of BAG in HDPE is found to be homogeneous and suitable for enhancing mechanical properties.
- T_{d5} and T_{dmax} of filament feedstock are higher than H_G. Residual weights corresponding to the BAG content of the composites obtained from TG curves are within the appreciable limit.
- T_{d5} and T_{dmax} are found to be unaffected by BAG addition. This highlights that the thermal stability of the developed composites is as good as neat H counterparts.
- T_c of the filament feedstock increases with respect to H_G. In contrast, T_m of the filament feedstock remains comparable with that of H_G.
- Crystallinity decreases with BAG addition, and H₂₀ exhibits 38.43% reduced crystallinity.
- Crystallinity estimated from XRD data is in agreement with the DSC investigation.
- The matrix HDPE can be processed within the temperature range of 130 – 460 °C without any degradation of HDPE matrix and for enhanced shear mixing of filler and moldability (filament extrusion and 3DP).
- Ultimate tensile strength and elongation at ultimate tensile strength decrease with BAG addition. H₂₀ samples show 14.95 and 60.91% lower ultimate tensile strength and elongation at ultimate tensile strength, respectively.
- Tensile modulus increases with BAG addition, and H₂₀ filaments show a 1.56 times higher modulus than neat H filaments.

Substrate and print adhesion

- The proposed SEBS adhesives are found to provide excellent adhesion to the first layer leading to dimensionally stable printed samples.
- Detachment of the printed samples from the substrate is easier without any necessity for secondary finishing operations.
- SEBS adhesives are found to be stable at prolonged and elevated temperature conditions.

Thermal behaviour analysis

- The coefficient of thermal expansion decreases with BAG addition. H₂₀ samples show a 50.62% reduced coefficient of thermal expansion than neat H samples.
- The thermal stability of the developed composites is as good as neat H counterparts as T_{d5}, and T_{dmax} is found to be unaffected by BAG addition.
- T_{d5} and T_{dmax} of prints are lower than their filament counterpart, and H₂₀ printed samples exhibit 2.34 and 3.27% lower T_{d5} and T_{dmax}, respectively than their filament counterpart.
- The degree of crystallinity decreases with BAG addition. H₂₀ shows a 38.43 and 34.25% reduced degree of crystallinity than neat H filaments and printed samples, respectively. XRD evaluation of crystallinity is analogous to the DSC estimation.
- Due to cold-crystallization, printed samples' crystallinity is higher than their filament counterparts.
- Solidification-induced shrinkage is reduced by increasing T_b to 110 °C and providing a raft of 8mm.
- T_p is increased to 240 °C to render printed samples with zero print-induced defects.
- T_e is elevated to 70 °C to minimize thermal gradient along Z-axis, leading to dimensionally stable printed samples with negligible warpage and delamination.
- Printed samples are cooled to room temperature inside the build chamber via natural convection.

Melt behaviour analysis

- MFI decreases with BAG addition. H₂₀ samples show 37.15% reduced MFI than neat H samples.

- Storage and loss modulus increases with BAG addition. At low frequency (0.0628 rad/s), H₂₀ samples display 10.78 and 3.71 times higher storage and loss modulus, respectively, than neat H samples.
- The complex viscosity of the composite feedstock increases with BAG addition. H₂₀ shows 1.73 times higher complex viscosity than neat H samples at a lower frequency of 0.0628 rad/sec.
- Higher complex viscosity of composite feedstock leads to incomplete deposition of material. Material flow rate (extruder multiplier) is enhanced to 1.05x and 1.1x for H₁₀ and H₂₀ samples to get essential interfacial diffusion and wetting.
- The developed feedstock is printed at an increased material flow rate without any slippage or breakage at the entry of the nozzle.

Surface and microstructural features of printed sample

- Optimized print parameters result in seamless diffusion of layers with zero weld line defects resulting in enhanced mechanical properties.
- Samples printed with the optimized parameters are found to be dimensionally stable and free of delamination and swelling.
- The porosity of the samples increases with BAG addition, and the values are close to that of their respective filaments.

Tensile properties

- Tensile modulus increases with BAG addition. H₂₀ samples display 1.82 times higher modulus than neat H samples.
- Ultimate tensile strength decreases with BAG addition. H₂₀ shows a 12.9% reduced ultimate tensile strength compared to neat H samples.
- The fracture strength of the samples increases with BAG addition. And H₂₀ samples exhibit 1.48 times higher fracture strength than neat H samples.
- Printed neat H and H/BAG samples exhibit 1.09, 1.26, 1.19, and 1.27 times better modulus than the respective filament feedstock. The printed neat H samples display 26% higher modulus than injection molded samples.

- The tensile strength of the developed composites is comparable to trabecular bone's tensile strength. Whereas the tensile modulus of the H/BAG composite is found to be higher than trabecular bone.

Flexural properties

- The flexural modulus of the composites is higher than the neat H samples. H₂₀ shows 1.45 times higher modulus than neat H samples.
- Flexural strength increases with an increase in BAG addition. H₂₀ shows 1.20 times higher strength than neat H samples.
- The printed neat H samples show 1.85 times higher flexural modulus when compared with the injection-moulded counterpart.
- The flexural strength of the developed composites is comparable with the flexural strength of trabecular bone. In contrast, the flexural modulus of the H/BAG composite is found to be higher than trabecular bone.

Compression properties

- All the samples exhibit the same levels of strain and similar deformation features irrespective of strain rate (static and quasi-static).
- Stress-strain curves are divided into three distinct regions to understand the deformation mechanism.
- The fractured surface shows brittle surface, wrinkles, fibrils (buckled, elongated, ruptured, peeled), voids, crazes, cracks, and ductile bands.

Static compression

- Compression strength and modulus increase with BAG addition. H₂₀ samples show 18.04 and 22.87 % higher compression strength and modulus.
- Energy absorption of the developed composites improved with BAG addition. H₂₀ exhibited 1.18 and 1.05 times better energy absorption than H₅ and neat H samples, respectively.
- Densification strain decreases with BAG addition. H₂₀ samples exhibit a 4% reduced densification strain than H₅ samples.

- The compression strength and modulus of the developed composites are higher than the trabecular bone.

Quasi-static compression

- Compressive modulus and strength increase with BAG addition and strain rate. H₂₀ samples at a 0.1 s⁻¹ strain rate exhibit 1.17 and 1.25 times higher modulus and yield strength than the corresponding H₂₀ sample at a 0.001 s⁻¹ strain rate.
- Addition of stiffer BAG results in decreased energy absorption of composites. At 0.001 s⁻¹ strain rate, the energy absorption of neat H is 13.50% higher than H₂₀ samples.
- Energy absorption increases with an increase in strain rate. Energy absorption at 0.001 s⁻¹ is 14.47 % lower for neat H samples than its value at 0.1 s⁻¹ strain rate.
- Densification strain increases with BAG addition. Neat H samples show an 8.51% higher densification strain than H₂₀ samples at a 0.001 s⁻¹ strain rate.

Impact Properties

- Addition of BAG results in enhanced stiffness of the H/BAG composites.
- The impact strength of the samples decreases with the addition of BAG, and H₂₀ samples show 62.16% reduced impact strength.

DMA behaviour

- Storage modulus increases with BAG addition, and H₂₀ samples display the maximum storage modulus.
- Storage modulus decreases with temperature for neat H and H/BAG composites. The deviation of storage modulus at increased temperature is in a close range.
- The loss modulus of the H/BAG composites is higher than the neat H counterpart.
- Damping factor decreases with BAG addition due to restricted HDPE molecular mobility.
- The changes in the storage modulus, loss modulus, and loss factor with the increase in temperature below the melting point indicate the disappearance of crystal phases that restrict the mobility of the amorphous phase. This emphasizes the necessity of

considering the temperature-dependent viscoelastic properties while designing the H/BAG implants.

- At a clinical temperature of 37 °C, storage modulus, loss modulus and loss factor is observed to increase with BAG addition highlighting the enhanced ability to dissipate energy.
- Such developed H/BAG composites with enhanced viscoelastic properties can be used as implants and scaffolds where stiffness and enhanced damping abilities play a significant role.

The present doctoral work successfully exhibited the prospects of melt compounding of BAG reinforced HDPE composites to develop filament feedstock and subsequent printing using the FFF process. The printability of the developed feedstock is evaluated. The mechanical properties of the developed H/BAG composites can be tailored via controlled porosity to mimic the properties of the trabecular bone. The experimental results exhibited as part of the work can be used to fabricate on-demand patient-specific biomedical implants and scaffolds.

SCOPE OF FUTURE WORK

The present work evaluates the printability of BAG reinforced HDPE composite filaments for the FFF process. The mechanical properties of the developed composites are investigated. Biological studies can be carried out to understand the interaction of the developed composites with bodily fluids. Further, tribological and creep behaviour of the developed composites can be evaluated. The effect of thermal processing and BAG reinforcement on the crystal morphology can be evaluated to enhance the mechanical properties. A porous scaffold can be fabricated to study the load-bearing characteristics. Geometric tolerances of the FFF process for the developed material system can be evaluated based on standard artifacts with generic geometric features. Direct pellet extrusion of the H/BAG composites can circumvent the additional melt compounding process. The surface-treated HDPE reinforced with BAG can be evaluated for its resulting properties. Crosslinking of BAG with polydopamine to study the interfacial interaction with HDPE matrix can be carried out.

REFERENCES

- Abeykoon, C., Kelly, A. L., Brown, E. C. and Coates, P. D. (2016). "The effect of materials, process settings and screw geometry on energy consumption and melt temperature in single screw extrusion." *Applied Energy*, 180, 880-894.
- Aktitiz, İ., Varol, R., Akkurt, N. and Saraç, M. F. (2020). "In-situ synthesis of 3D printable mono-and Bi-metallic (Cu/Ag) nanoparticles embedded polymeric structures with enhanced electromechanical properties." *Polymer Testing*, 90, 106724.
- Al-allaq, A. A., Kashan, J. S., El-Wakad, M. T. and Soliman, A. M. (2021). "Multiwall carbon nanotube reinforced HA/HDPE biocomposite for bone reconstruction." *Periodicals of Engineering and Natural Sciences (PEN)*, 9(2), 930-939.
- Al Rashid, A., Khan, S. A., Al-Ghamdi, S. G. and Koç, M. (2021). "Additive manufacturing of polymer nanocomposites: Needs and challenges in materials, processes, and applications." *Journal of Materials Research and Technology*, 14, 910-941.
- Ang, K., Leong, K., Chua, C. and Chandrasekaran, M. (2007). "Compressive properties and degradability of poly (ϵ -caprolactone)/hydroxyapatite composites under accelerated hydrolytic degradation." *Journal of Biomedical Materials Research Part A*, 80(3), 655-660.
- Arencón, D. and Velasco, J. I. (2009). "Fracture Toughness of Polypropylene-Based Particulate Composites." *Materials*, 2(4), 2046-2094.
- ASTM D618-13, *Standard Practice for Conditioning Plastics for Testing*, ASTM International, PA, USA.
- ASTM D638-14, *Standard Test Method for Tensile Properties of Plastics*, ASTM International, PA, USA.
- ASTM D695-15, *Standard Test Method for Compressive Properties of Rigid Plastics*, ASTM International, PA, USA.
- ASTM D790-17, *Standard Test Methods for Flexural Properties of Unreinforced and Reinforced Plastics and Electrical Insulating Materials*, ASTM International, PA, USA.
- ASTM D792-13, *Standard Test Methods for Density and Specific Gravity (Relative Density) of Plastics by Displacement*, ASTM International, PA, USA.
- ASTM D1238-13, *Standard Test Method for Melt Flow Rates of Thermoplastics by Extrusion Plastometer*, ASTM International, PA, USA.

ASTM D3418-15, *Standard Test Method for Transition Temperatures and Enthalpies of Fusion and Crystallization of Polymers by Differential Scanning Calorimetry*, ASTM International, PA, USA.

ASTM D4440-15, *Standard Test Method for Plastics: Dynamic Mechanical Properties Melt Rheology*, ASTM International, PA, USA.

ASTM D5023-15, *Standard test method for plastics: Dynamic mechanical properties: In flexure (three-point bending)*, ASTM International, PA, USA.

ASTM D6110-18, *Standard test methods for determining the Charpy impact resistance of notched specimens of plastics*, ASTM International, PA, USA.

ASTM E228-17, *Standard Test Method for Linear Thermal Expansion of Solid Materials with a Push-rod Dilatometer1*, ASTM International, PA, USA.

Awad, A., El-Gamasy, R., Abd El-Wahab, A. A. and Abdellatif, M. H. (2020). "Assessment of mechanical properties of HDPE composite with addition of marble and granite dust." *Ain Shams Engineering Journal*, 11(4), 1211-1217.

Bakır, A. A., Atik, R. and Özerinç, S. (2021). "Effect of fused deposition modeling process parameters on the mechanical properties of recycled polyethylene terephthalate parts." *Journal of applied polymer science*, 138(3), 49709.

Balla, V. K., Bodhak, S., Datta, P., Kundu, B., Das, M., Bandyopadhyay, A. and Bose, S. (2020). Biointegration of three-dimensional-printed biomaterials and biomedical devices *Biointegration of Medical Implant Materials* (pp. 433-482): Elsevier.

Barbieri, D., de Bruijn, J. D., Luo, X., Fare, S., Grijpma, D. W. and Yuan, H. (2013). "Controlling dynamic mechanical properties and degradation of composites for bone regeneration by means of filler content." *Journal of the Mechanical Behaviour of Biomedical Materials*, 20, 162-172.

Beatrice, C. A. G., Shimomura, K. M. B., Backes, E. H., Harb, S. V., Costa, L. C., Passador, F. R. and Pessan, L. A. (2021). "Engineering printable composites of poly (ϵ -polycaprolactone)/ β -tricalcium phosphate for biomedical applications." *Polymer Composites*, 42(3), 1198-1213.

Beesetty, P., Patil, B. and Doddamani, M. (2020). "Mechanical behavior of additively manufactured Nanoclay/HDPE nanocomposites." *Composite Structures*, 112442.

Bharath Kumar, B., Doddamani, M., Zeltmann, S. E., Gupta, N., Gurupadu, S. and Sailaja, R. (2016). "Effect of particle surface treatment and blending method on flexural properties of injection-molded cenosphere/HDPE syntactic foams." *Journal of Materials Science*, 51(8), 3793-3805.

- Bharath Kumar, B., Zeltmann, S. E., Doddamani, M., Gupta, N., Gurupadu, S. and Sailaja, R. (2016). "Effect of cenosphere surface treatment and blending method on the tensile properties of thermoplastic matrix syntactic foams." *Journal of applied polymer science*, 133(35).
- Bharath Kumar, B. R., Singh, A. K., Doddamani, M., Luong, D. D. and Gupta, N. (2016). "Quasi-Static and High Strain Rate Compressive Response of Injection-Molded Cenosphere/HDPE Syntactic Foam." *JOM*, 68(7), 1861-1871.
- Bonthu, D., Bharath, H., Gururaja, S., Prabhakar, P. and Doddamani, M. (2020). "3D printing of syntactic foam cored sandwich composite." *Composites Part C: Open Access*, 3, 100068.
- Boparai, K. S., Singh, R. and Singh, H. (2016). "Process optimization of single screw extruder for development of Nylon 6-Al-Al₂O₃ alternative FDM filament." *Rapid Prototyping Journal*, 22(4), 766-776.
- Bose, S., Vahabzadeh, S. and Bandyopadhyay, A. (2013). "Bone tissue engineering using 3D printing." *Materials Today*, 16(12), 496-504.
- Brackett, J., Yan, Y., Cauthen, D., Kishore, V., Lindahl, J., Smith, T., Sudbury, Z., Ning, H., Kunc, V. and Duty, C. (2021). "Characterizing material transitions in large-scale Additive Manufacturing." *Additive Manufacturing*, 38, 101750.
- Bragaglia, M., Lamastra, F. R., Russo, P., Vitiello, L., Rinaldi, M., Fabbrocino, F. and Nanni, F. (2021). "A comparison of thermally conductive polyamide 6-boron nitride composites produced via additive layer manufacturing and compression molding." *Polymer Composites*, 42(6), 2751-2765.
- Butler, M. F., Donald, A. M., Bras, W., Mant, G. R., Derbyshire, G. E. and Ryan, A. J. (1995). "A real-time simultaneous small-and wide-angle X-ray scattering study of in-situ deformation of isotropic polyethylene." *Macromolecules*, 28(19), 6383-6393.
- Cao, S., Wei, X.-F., Sun, Z.-J. and Zhang, H.-H. (2015). "Investigation on urea-formaldehyde resin as an in-powder adhesive for the fabrication of Al₂O₃/borosilicate-glass composite parts by three dimensional printing (3DP)." *Journal of Materials Processing Technology*, 217, 241-252.
- Chalisgaonkar, V., Das, M. and Balla, V. K. (2018). "Laser processing of Ti composite coatings reinforced with hydroxyapatite and bioglass." *Additive Manufacturing*, 20, 134-143.
- Chen, J., Yang, W., Yu, G.-p., Wang, M., Ni, H.-y. and Shen, K.-z. (2008). "Continuous extrusion and tensile strength of self-reinforced HDPE/UHMWPE sheet." *Journal of Materials Processing Technology*, 202(1-3), 165-169.

Choi, S.-Y., Shin, H.-I., Kwon, T.-Y. and Kwon, T.-G. (2017). "Histopathological and scanning electron microscopy findings of retrieved porous polyethylene implants." *International Journal of Oral and Maxillofacial Surgery*, 46(5), 582-585.

Chowdhury, S. R., Mishra, A., Pradhan, B. and Saha, D. (2004). "Wear characteristic and biocompatibility of some polymer composite acetabular cups." *Wear*, 256(11-12), 1026-1036.

Chrysafi, I., Kontonasaki, E., Anastasiou, A. D., Patsiaoura, D., Papadopoulou, L., Vourlias, G., Vouvoudi, E. and Bikiaris, D. (2020). "Mechanical and thermal properties of PMMA resin composites for interim fixed prostheses reinforced with calcium β -pyrophosphate." *Journal of the Mechanical Behavior of Biomedical Materials*, 112, 104094.

da Costa, H. M., Ramos, V. D. and de Oliveira, M. G. (2007). "Degradation of polypropylene (PP) during multiple extrusions: Thermal analysis, mechanical properties and analysis of variance." *Polymer Testing*, 26(5), 676-684.

Dahl, K. A., Moritz, N. and Vallittu, P. K. (2018). "Flexural and torsional properties of a glass fiber-reinforced composite diaphyseal bone model with multidirectional fiber orientation." *Journal of the Mechanical Behavior of Biomedical Materials*, 87, 143-147.

Daver, F., Lee, K. P. M., Brandt, M. and Shanks, R. (2018). "Cork-PLA composite filaments for fused deposition modelling." *Composites Science and Technology*, 168, 230-237.

de Carvalho, M. S., Azevedo, J. B. and Barbosa, J. D. V. (2020). "Effect of the melt flow index of an HDPE matrix on the properties of composites with wood particles." *Polymer Testing*, 90, 106678.

Deshpande, S. and Munoli, A. (2010). "Long-term results of high-density porous polyethylene implants in facial skeletal augmentation: An Indian perspective." *Indian Journal of Plastic Surgery*, 43(01), 034-039.

Dey, A., Roan Eagle, I. N. and Yodo, N. (2021). "A review on filament materials for fused filament fabrication." *Journal of manufacturing and materials processing*, 5(3), 69.

Diederichs, E. V., Picard, M. C., Chang, B. P., Misra, M., Mielewski, D. F. and Mohanty, A. K. (2019). "Strategy to improve printability of renewable resource-based engineering plastic tailored for fdm applications." *ACS omega*, 4(23), 20297-20307.

Distler, T., Fournier, N., Grünewald, A., Polley, C., Seitz, H., Detsch, R. and Boccaccini, A. R. (2020). "Polymer-bioactive glass composite filaments for 3D scaffold manufacturing by fused deposition modeling: fabrication and characterization." *Frontiers in bioengineering and biotechnology*, 8, 552.

- Doddamani, M. (2019). "Effect of surface treatment on quasi-static compression and dynamic mechanical analysis of syntactic foams." *Composites Part B: Engineering*, 165, 365-378.
- Doddamani, M. (2020). "Dynamic mechanical analysis of 3D printed eco-friendly lightweight composite." *Composites Communications*.
- Doddamani, M. (2020). "Influence of microballoon wall thickness on dynamic mechanical analysis of closed cell foams." *Materials Research Express*, 6(12), 125348.
- Dong, C., Zhu, S., Mizuno, M. and Hashimoto, M. (2011). "Fatigue behavior of HDPE composite reinforced with Silane modified TiO₂." *Journal of Materials Science & Technology*, 27(7), 659-667.
- Dutta, S., Devi, K. B., Gupta, S., Kundu, B., Balla, V. K. and Roy, M. (2019). "Mechanical and in vitro degradation behavior of magnesium-bioactive glass composites prepared by SPS for biomedical applications." *Journal of Biomedical Materials Research Part B: Applied Biomaterials*, 107(2), 352-365.
- Economidou, S. N. and Karalekas, D. (2016). "Optical sensor-based measurements of thermal expansion coefficient in additive manufacturing." *Polymer Testing*, 51, 117-121.
- Elhattab, K., Bhaduri, S. B., Lawrence, J. G. and Sikder, P. (2021). "Fused filament fabrication (three-dimensional printing) of amorphous magnesium phosphate/polylactic acid macroporous biocomposite scaffolds." *ACS Applied Bio Materials*, 4(4), 3276-3286.
- Fan, J. and Wang, C. (2018). "Dynamic compressive response of a developed polymer composite at different strain rates." *Composites Part B: Engineering*, 152, 96-101.
- Fonseca, C. A. and Harrison, I. R. (1998). "An investigation of co-crystallization in LDPE/HDPE blends using DSC and TREF." *Thermochimica acta*, 313(1), 37-41.
- Fouad, H. and Elleithy, R. (2011). "High density polyethylene/graphite nanocomposites for total hip joint replacements: Processing and in vitro characterization." *Journal of the Mechanical Behavior of Biomedical Materials*, 4(7), 1376-1383.
- Fouad, H., Elleithy, R. and Alothman, O. Y. (2013). "Thermo-mechanical, wear and fracture behavior of high-density polyethylene/hydroxyapatite nano composite for biomedical applications: effect of accelerated ageing." *Journal of Materials Science & Technology*, 29(6), 573-581.
- Gao, X., Qi, S., Zhang, D., Su, Y. and Wang, D. (2020). "The role of poly (ethylene glycol) on crystallization, interlayer bond and mechanical performance of polylactide parts fabricated by fused filament fabrication." *Additive Manufacturing*, 35, 101414.

Gebler, M., Uiterkamp, A. J. S. and Visser, C. (2014). "A global sustainability perspective on 3D printing technologies." *Energy policy*, 74, 158-167.

Ghorbani, F., Sahranavard, M., Mousavi Nejad, Z., Li, D., Zamanian, A. and Yu, B. (2020). "Surface functionalization of three dimensional-printed polycaprolactone-bioactive glass scaffolds by grafting GelMA under UV irradiation." *Frontiers in Materials*, 7, 528590.

HS, B., Bonthu, D., Prabhakar, P. and Doddamani, M. (2020). "Three-dimensional printed lightweight composite foams." *ACS omega*, 5(35), 22536-22550.

Iragi, M., Pascual-Gonzalez, C., Esnaola, A., Lopes, C. and Aretxabaleta, L. (2019). "Ply and interlaminar behaviours of 3D printed continuous carbon fibre-reinforced thermoplastic laminates; effects of processing conditions and microstructure." *Additive Manufacturing*, 30, 100884.

Jaggi, H. S., Kumar, Y., Satapathy, B. K., Ray, A. R. and Patnaik, A. (2012). "Analytical interpretations of structural and mechanical response of high density polyethylene/hydroxyapatite bio-composites." *Materials & Design (1980-2015)*, 36, 757-766.

Jayavardhan, M. and Doddamani, M. (2018). "Quasi-static compressive response of compression molded glass microballoon/HDPE syntactic foam." *Composites Part B: Engineering*, 149, 165-177.

Jeyachandran, P., Bontha, S., Bodhak, S., Balla, V. K., Kundu, B. and Doddamani, M. (2020). "Mechanical behaviour of additively manufactured bioactive glass/high density polyethylene composites." *Journal of the Mechanical Behavior of Biomedical Materials*, 103830.

Kaur, G., Kumar, V., Baino, F., Mauro, J. C., Pickrell, G., Evans, I. and Bretcanu, O. (2019). "Mechanical properties of bioactive glasses, ceramics, glass-ceramics and composites: State-of-the-art review and future challenges." *Materials Science and Engineering: C*, 104, 109895.

Keothongkham, K., Charoenphandhu, N., Thongbunchoo, J., Suntornsaratoon, P., Krishnamra, N., Tang, I.-M. and Pon-On, W. (2017). "Evaluation of bioactive glass incorporated poly (caprolactone)-poly (vinyl alcohol) matrix and the effect of BMP-2 modification." *Materials Science and Engineering: C*, 74, 47-54.

Khalifa, M., Wuzella, G., Bagawan, A. H., Lammer, H. and Mahendran, A. R. (2022). "Poly (vinylidene fluoride)/Mica nanocomposite: a potential material for photovoltaic backsheets application." *Materials Chemistry and Physics*, 277, 125551.

Khan, P. K., Mahato, A., Kundu, B., Nandi, S. K., Mukherjee, P., Datta, S., Sarkar, S., Mukherjee, J., Nath, S. and Balla, V. K. (2016). "Influence of single and binary doping

of strontium and lithium on in vivo biological properties of bioactive glass scaffolds." *Scientific Reports*, 6(1), 1-18.

Khatua, C., Bhattacharya, D., Kundu, B., Balla, V. K., Bodhak, S. and Goswami, S. (2018). "Multiferroic reinforced bioactive glass composites for bone tissue engineering applications." *Advanced Engineering Materials*, 20(12), 1800329.

Khatua, C., Bodhak, S., Kundu, B. and Balla, V. K. (2018). "In vitro bioactivity and bone mineralization of bismuth ferrite reinforced bioactive glass composites." *Materialia*, 4, 361-366.

Kim, C. G., Han, K. S., Lee, S., Kim, M. C., Kim, S. Y. and Nah, J. (2021). "Fabrication of Biocompatible Polycaprolactone–Hydroxyapatite Composite Filaments for the FDM 3D Printing of Bone Scaffolds." *Applied Sciences*, 11(14), 6351.

Konka, J., Buxadera-Palomero, J., Espanol, M. and Ginebra, M.-P. (2021). "3D printing of hierarchical porous biomimetic hydroxyapatite scaffolds: Adding concavities to the convex filaments." *Acta biomaterialia*, 134, 744-759.

Kousiatza, C., Tzetzis, D. and Karalekas, D. (2019). "In-situ characterization of 3D printed continuous fiber reinforced composites: A methodological study using fiber Bragg grating sensors." *Composites Science and Technology*, 174, 134-141.

Kumar, B. B., Singh, A. K., Doddamani, M., Luong, D. D. and Gupta, N. (2016). "Quasi-static and high strain rate compressive response of injection-molded cenosphere/HDPE syntactic foam." *JOM*, 68(7), 1861-1871.

Kumar, S., Singh, R., Singh, T. and Batish, A. (2020). "Fused filament fabrication: A comprehensive review." *Journal of Thermoplastic Composite Materials*, 0892705720970629.

Lacambra-Andreu, X., Dergham, N., Magallanes-Perdomo, M., Meille, S., Chevalier, J., Chenal, J.-M., Maazouz, A. and Lamnawar, K. (2021). "Model Composites Based on Poly (lactic acid) and Bioactive Glass Fillers for Bone Regeneration." *Polymers*, 13(17), 2991.

Lamm, M. E., Wang, L., Kishore, V., Tekinalp, H., Kunc, V., Wang, J., Gardner, D. J. and Ozcan, S. (2020). "Material extrusion additive manufacturing of wood and lignocellulosic filled composites." *Polymers*, 12(9), 2115.

Lee, H., Lee, J. W., Hong, I.-K. and Lee, S. (2014). "Optimal two-stage single-screw design for polymethyl methacrylate extrusion by taguchi technique." *Journal of Industrial and Engineering Chemistry*, 20(3), 1119-1125.

Lee, K. P. M., Brandt, M., Shanks, R. and Daver, F. (2020). "Rheology and 3D Printability of Percolated Graphene–Polyamide-6 Composites." *Polymers*, 12(9), 2014.

Li, F., Gao, L., Gao, H. and Cui, Y. (2017). "The mechanical properties and modeling of creep behavior of UHMWPE/Nano-HA composites." *Journal of Materials Engineering and Performance*, 26(9), 4514-4521.

Lin, J.-H., Pan, Y.-J., Liu, C.-F., Huang, C.-L., Hsieh, C.-T., Chen, C.-K., Lin, Z.-I. and Lou, C.-W. (2015). "Preparation and compatibility evaluation of polypropylene/high density polyethylene polyblends." *Materials*, 8(12), 8850-8859.

Liu, P., Dinwiddie, R. B., Keum, J. K., Vasudevan, R. K., Jesse, S., Nguyen, N. A., Lindahl, J. M. and Kunc, V. (2018). "Rheology, crystal structure, and nanomechanical properties in large-scale additive manufacturing of polyphenylene sulfide/carbon fiber composites." *Composites Science and Technology*, 168, 263-271.

Liu, S., Xu, S., Song, J., Zhou, J., Xu, L., Li, X. and Zou, M. (2020). "Mechanical properties and failure deformation mechanisms of yak horn under quasi-static compression and dynamic impact." *Journal of the Mechanical Behavior of Biomedical Materials*, 103753.

Liu, T., Huang, K., Li, L., Gu, Z., Liu, X., Peng, X. and Kuang, T. (2019). "High performance high-density polyethylene/hydroxyapatite nanocomposites for load-bearing bone substitute: fabrication, in vitro and in vivo biocompatibility evaluation." *Composites Science and Technology*, 175, 100-110.

Liu, Z., Wang, Y. and Shi, J. (2019). "Tensile performance of fused deposition modeling PA 6 polymer composites with nanoparticle reinforcement and/or continuous fiber reinforcement." *Journal of Micro and Nano-Manufacturing*, 7(4).

Lu, X., Tang, L., Wang, L., Zhao, J., Li, D., Wu, Z. and Xiao, P. (2016). "Morphology and properties of bio-based poly (lactic acid)/high-density polyethylene blends and their glass fiber reinforced composites." *Polymer Testing*, 54, 90-97.

Mahesh, V., Joseph, A. S., Mahesh, V., Harursampath, D. and VN, C. (2021). "Investigation on the mechanical properties of additively manufactured PETG composites reinforced with OMMT nanoclay and carbon fibers." *Polymer Composites*, 42(5), 2380-2395.

Maroulakos, M., Kamperos, G., Tayebi, L., Halazonetis, D. and Ren, Y. (2019). "Applications of 3D printing on craniofacial bone repair: A systematic review." *Journal of Dentistry*, 80, 1-14.

Martin, V., Ribeiro, I. A., Alves, M. M., Gonçalves, L., Claudio, R. A., Grenho, L., Fernandes, M. H., Gomes, P., Santos, C. F. and Bettencourt, A. F. (2019). "Engineering a multifunctional 3D-printed PLA-collagen-minocycline-nanoHydroxyapatite scaffold with combined antimicrobial and osteogenic effects for bone regeneration." *Materials Science and Engineering: C*, 101, 15-26.

- Mavrikakis, I., Francis, N., Poitelea, C., Parkin, B., Brittain, P. and Olver, J. (2009). "Medpor® lower eyelid spacer: does it Biointegrate?". *Orbit*, 28(1), 58-62.
- Morales, M. A., Atencio Martinez, C. L., Maranon, A., Hernandez, C., Michaud, V. and Porras, A. (2021). "Development and characterization of rice husk and recycled polypropylene composite filaments for 3D printing." *Polymers*, 13(7), 1067.
- Mummareddy, B., Maravola, M., MacDonald, E., Walker, J., Hetzel, B., Conner, B. and Cortes, P. (2020). "The fracture properties of metal-ceramic composites manufactured via stereolithography." *International Journal of Applied Ceramic Technology*, 17(2), 413-423.
- Muniyandi, S. K., Sohaili, J. and Hassan, A. (2013). "Mechanical, thermal, morphological and leaching properties of nonmetallic printed circuit board waste in recycled HDPE composites." *Journal of Cleaner production*, 57, 327-334.
- Nabipour, M., Akhouni, B. and Bagheri Saed, A. (2020). "Manufacturing of polymer/metal composites by fused deposition modeling process with polyethylene." *Journal of applied polymer science*, 137(21), 48717.
- Nurhudan, A. I., Supriadi, S., Whulanza, Y. and Saragih, A. S. (2021). "Additive manufacturing of metallic based on extrusion process: A review." *Journal of Manufacturing Processes*, 66, 228-237.
- Omar, M. F., Akil, H. M. and Ahmad, Z. A. (2012). "Effect of molecular structures on dynamic compression properties of polyethylene." *Materials Science and Engineering: A*, 538, 125-134.
- Pahlevanzadeh, F., Bakhsheshi-Rad, H. and Hamzah, E. (2018). "In-vitro biocompatibility, bioactivity, and mechanical strength of PMMA-PCL polymer containing fluorapatite and graphene oxide bone cements." *Journal of the Mechanical Behavior of Biomedical Materials*, 82, 257-267.
- Palacios-Ibáñez, B., Relinque, J. J., Moreno-Sánchez, D., de León, A. S., Delgado, F. J., Escobar-Galindo, R. and Molina, S. I. (2022). "Synthesis and Characterisation of ASA-PEEK Composites for Fused Filament Fabrication." *Polymers*, 14(3), 496.
- Pan, S., Shen, H. and Zhang, L. (2021). "Effect of carbon nanotube on thermal, tribological and mechanical properties of 3D printing polyphenylene sulfide." *Additive Manufacturing*, 47, 102247.
- Paspali, A., Bao, Y., Gawne, D. T., Piestert, F. and Reinelt, S. (2018). "The influence of nanostructure on the mechanical properties of 3D printed polylactide/nanoclay composites." *Composites Part B: Engineering*, 152, 160-168.
- Patil, B., Kumar, B. B., Bontha, S., Balla, V. K., Powar, S., Kumar, V. H., Suresha, S. and Doddamani, M. (2019). "Eco-friendly lightweight filament synthesis and

mechanical characterization of additively manufactured closed cell foams." *Composites Science and Technology*, 183, 107816.

Paxton, N. C., Allenby, M. C., Lewis, P. M. and Woodruff, M. A. (2019). "Biomedical applications of polyethylene." *European Polymer Journal*, 118, 412-428.

Paxton, N. C., Dinoro, J., Ren, J., Ross, M. T., Daley, R., Zhou, R., Bazaka, K., Thompson, R. G., Yue, Z. and Beirne, S. (2021). "Additive manufacturing enables personalised porous high-density polyethylene surgical implant manufacturing with improved tissue and vascular ingrowth." *Applied Materials Today*, 22, 100965.

Peñas, M. I., Calafel, M. I., Aguirresarobe, R. H., Tierno, M., Conde, J. I., Pascual, B. and Santamaría, A. (2020). "How Is Rheology Involved in 3D Printing of Phase-Separated PVC-Acrylate Copolymers Obtained by Free Radical Polymerization." *Polymers*, 12(9), 2070.

Peng, B., Yang, Y., Ju, T. and Cavicchi, K. A. (2020). "Fused filament fabrication 4D printing of a highly extensible, self-healing, shape memory elastomer based on thermoplastic polymer blends." *ACS applied materials & interfaces*, 13(11), 12777-12788.

Petersmann, S., Spoerk-Erdely, P., Feuchter, M., Wieme, T., Arbeiter, F. and Spoerk, M. (2020). "Process-induced morphological features in material extrusion-based additive manufacturing of polypropylene." *Additive Manufacturing*, 35, 101384.

Petersmann, S., Spoerk, M., Van De Steene, W., Üçal, M., Wiener, J., Pinter, G. and Arbeiter, F. (2020). "Mechanical properties of polymeric implant materials produced by extrusion-based additive manufacturing." *Journal of the Mechanical Behavior of Biomedical Materials*, 104, 103611.

Ponnamma, D., Cabibihan, J.-J., Rajan, M., Pethaiah, S. S., Deshmukh, K., Gogoi, J. P., Pasha, S. K., Ahamed, M. B., Krishnegowda, J. and Chandrashekar, B. (2019). "Synthesis, optimization and applications of ZnO/polymer nanocomposites." *Materials Science and Engineering: C*.

Potyondy, T., Uquillas, J. A., Tebon, P. J., Byambaa, B., Hasan, A., Tavafoghi, M., Mary, H., Aninwene, G. E., Pountos, I. and Khademhosseini, A. (2021). "Recent advances in 3D bioprinting of musculoskeletal tissues." *Biofabrication*, 13(2), 022001.

Riaz, M., Zia, R., Saleemi, F., Hussain, T., Bashir, F. and Ikhrum, H. (2016). "Effect of Ti+ 4 on in vitro bioactivity and antibacterial activity of silicate glass-ceramics." *Materials Science and Engineering: C*, 69, 1058-1067.

Ribeiro, I., Matos, F., Jacinto, C., Salman, H., Cardeal, G., Carvalho, H., Godina, R. and Peças, P. (2020). "Framework for life cycle sustainability assessment of additive manufacturing." *Sustainability*, 12(3), 929.

Rodzeń, K., Sharma, P. K., McIlhagger, A., Mokhtari, M., Dave, F., Tormey, D., Sherlock, R., Meenan, B. J. and Boyd, A. (2021). "The direct 3D printing of functional PEEK/hydroxyapatite composites via a fused filament fabrication approach." *Polymers*, 13(4), 545.

Roy, P. and Sailaja, R. (2015). "Mechanical, thermal and bio-compatibility studies of PAEK-hydroxyapatite nanocomposites." *Journal of the Mechanical Behavior of Biomedical Materials*, 49, 1-11.

Saleh Alghamdi, S., John, S., Roy Choudhury, N. and Dutta, N. K. (2021). "Additive manufacturing of polymer materials: Progress, promise and challenges." *Polymers*, 13(5), 753.

Salem, A., Bensalah, W. and Mezlini, S. (2021). "Effect of hygrothermal aging on the tribological behavior of HDPE composites for bio-implant application." *Polymer Testing*, 94, 107050.

Salmoria, G. V., Ahrens, C. H., Klauss, P., Paggi, R. A., Oliveira, R. G. and Lago, A. (2007). "Rapid manufacturing of polyethylene parts with controlled pore size gradients using selective laser sintering." *Materials Research*, 10, 211-214.

Samsudin, D., Ismail, H., Othman, N. and Hamid, Z. A. A. (2016). "Comparative study of glut palmitate salt and polyethylene grafted maleic anhydride compatibilizer on the properties of silica filled high-density polyethylene composites." *Polymer Testing*, 52, 104-110.

Santos, S. C., Spaniol, K. G., Chaves-Silva, N. E., Fernandes, R. P., Tavares, D. S., Acchar, W. and dos Santos, E. A. (2021). "Copper-containing bioactive glass/PVA membranes for guided bone regeneration." *Journal of Non-Crystalline Solids*, 557, 120628.

Schirmeister, C. G., Hees, T., Licht, E. H. and Muelhaupt, R. (2019). "3D printing of high density polyethylene by fused filament fabrication." *Additive Manufacturing*, 28, 152-159.

Schirmeister, C. G., Schächtele, S., Keßler, Y., Hees, T., Köhler, R., Schmitz, K., Licht, E. H. and Muelhaupt, R. (2021). "Low Warpage Nanophase-Separated Polypropylene/Olefinic Elastomer Reactor Blend Composites with Digitally Tuned Glass Fiber Orientation by Extrusion-Based Additive Manufacturing." *ACS Applied Polymer Materials*, 3(4), 2070-2081.

Senatov, F. S., Niaza, K. V., Zadorozhnyy, M. Y., Maksimkin, A., Kaloshkin, S. and Estrin, Y. (2016). "Mechanical properties and shape memory effect of 3D-printed PLA-based porous scaffolds." *Journal of the Mechanical Behavior of Biomedical Materials*, 57, 139-148.

Shuai, C., Yang, B., Peng, S. and Li, Z. (2013). "Development of composite porous scaffolds based on poly (lactide-co-glycolide)/nano-hydroxyapatite via selective laser sintering." *The International Journal of Advanced Manufacturing Technology*, 69(1-4), 51-57.

Siacor, F. D. C., Chen, Q., Zhao, J. Y., Han, L., Valino, A. D., Taboada, E. B., Caldona, E. B. and Advincula, R. C. (2021). "On the additive manufacturing (3D printing) of viscoelastic materials and flow behavior: From composites to food manufacturing." *Additive Manufacturing*, 45, 102043.

Singh, A. K., Patil, B., Hoffmann, N., Saltonstall, B., Doddamani, M. and Gupta, N. (2018). "Additive Manufacturing of Syntactic Foams: Part 1: Development, Properties, and Recycling Potential of Filaments." *JOM*, 70(3), 303-309.

Singh, A. K., Saltonstall, B., Patil, B., Hoffmann, N., Doddamani, M. and Gupta, N. (2018). "Additive manufacturing of syntactic foams: Part 2: specimen printing and mechanical property characterization." *JOM*, 70(3), 310-314.

Singh, P., Balla, V. K., Tofangchi, A., Atre, S. V. and Kate, K. H. (2020). "Printability studies of Ti-6Al-4 V by metal fused filament fabrication (MF3)." *International Journal of Refractory Metals and Hard Materials*, 105249.

Singh, P., Shaikh, Q., Balla, V. K., Atre, S. V. and Kate, K. H. (2020). "Estimating Powder-Polymer Material Properties Used in Design for Metal Fused Filament Fabrication (DfMF 3)." *JOM*, 72(1), 485-495.

Singh, R., Bedi, P., Fraternali, F. and Ahuja, I. P. S. (2016). "Effect of single particle size, double particle size and triple particle size Al₂O₃ in Nylon-6 matrix on mechanical properties of feed stock filament for FDM." *Composites Part B: Engineering*, 106, 20-27.

Singh, R., Singh, S. and Mankotia, K. (2016). "Development of ABS based wire as feedstock filament of FDM for industrial applications." *Rapid Prototyping Journal*.

Sinha, S. and Meisel, N. A. (2020). "Predicting Material Properties for Embedded Structures Created with Polymer Material Extrusion Additive Manufacturing." *Additive Manufacturing*, 101247.

Smith, J. A., Li, S., Mele, E., Goulas, A., Engström, D. and Silberschmidt, V. V. "Printability and mechanical performance of biomedical PDMS-PEEK composites developed for material extrusion." *Journal of the Mechanical Behavior of Biomedical Materials*, 104291.

Spoerk, M., Arbeiter, F., Cajner, H., Sapkota, J. and Holzer, C. (2017). "Parametric optimization of intra-and inter-layer strengths in parts produced by extrusion-based additive manufacturing of poly (lactic acid)." *Journal of applied polymer science*, 134(41), 45401.

- Spoerk, M., Arbeiter, F., Raguž, I., Holzer, C. and Gonzalez-Gutierrez, J. (2019). "Mechanical Recyclability of Polypropylene Composites Produced by Material Extrusion-Based Additive Manufacturing." *Polymers*, 11(8), 1318.
- Spoerk, M., Arbeiter, F., Raguž, I., Weingrill, G., Fischinger, T., Traxler, G., Schuschnigg, S., Cardon, L. and Holzer, C. (2018). "Polypropylene filled with glass spheres in extrusion-based additive manufacturing: effect of filler size and printing chamber temperature." *Macromolecular Materials and Engineering*, 303(7), 1800179.
- Spoerk, M., Holzer, C. and Gonzalez-Gutierrez, J. (2020). "Material extrusion-based additive manufacturing of polypropylene: A review on how to improve dimensional inaccuracy and warpage." *Journal of applied polymer science*, 137(12), 48545.
- Spoerk, M., Sapkota, J., Weingrill, G., Fischinger, T., Arbeiter, F. and Holzer, C. (2017). "Shrinkage and warpage optimization of expanded-perlite-filled polypropylene composites in extrusion-based additive manufacturing." *Macromolecular Materials and Engineering*, 302(10), 1700143.
- Spoerk, M., Savandaiah, C., Arbeiter, F., Sapkota, J. and Holzer, C. (2019). "Optimization of mechanical properties of glass-spheres-filled polypropylene composites for extrusion-based additive manufacturing." *Polymer Composites*, 40(2), 638-651.
- Spoerk, M., Savandaiah, C., Arbeiter, F., Traxler, G., Cardon, L., Holzer, C. and Sapkota, J. (2018). "Anisotropic properties of oriented short carbon fibre filled polypropylene parts fabricated by extrusion-based additive manufacturing." *Composites Part A: Applied Science and Manufacturing*, 113, 95-104.
- Stolz, B., Mader, M., Volk, L., Steinberg, T. and Mülhaupt, R. (2020). "Cryo-3D Printing of Hierarchically Porous Polyhydroxymethylene Scaffolds for Hard Tissue Regeneration." *Macromolecular Materials and Engineering*, 2000541.
- Suwanprateeb, J., Thammarakcharoen, F., Wongsuvan, V. and Chokevivat, W. (2012). "Development of porous powder printed high density polyethylene for personalized bone implants." *Journal of Porous Materials*, 19(5), 623-632.
- Swetha, C. and Kumar, R. (2011). "Quasi-static uni-axial compression behaviour of hollow glass microspheres/epoxy based syntactic foams." *Materials & Design*, 32(8-9), 4152-4163.
- Takahashi, Y., Ishida, T. and Furusaka, M. (1988). "Monoclinic-to-orthorhombic transformation in polyethylene." *Journal of Polymer Science Part B: Polymer Physics*, 26(11), 2267-2277.
- Tan, L. J., Zhu, W. and Zhou, K. (2020). "Recent progress on polymer materials for additive manufacturing." *Advanced Functional Materials*, 30(43), 2003062.

Tjong, S. C. (2012). *Polymer composites with carbonaceous nanofillers: properties and applications*: John Wiley & Sons.

Vaes, D. and Van Puyvelde, P. (2021). "Semi-crystalline feedstock for filament-based 3D printing of polymers." *Progress in Polymer Science*, 101411.

Victor, S. P. and Muthu, J. (2014). "Bioactive, mechanically favorable, and biodegradable copolymer nanocomposites for orthopedic applications." *Materials Science and Engineering: C*, 39, 150-160.

Vijayavenkataraman, S., Yan, W.-C., Lu, W. F., Wang, C.-H. and Fuh, J. Y. H. (2018). "3D bioprinting of tissues and organs for regenerative medicine." *Advanced drug delivery reviews*, 132, 296-332.

Wang, B., Qu, S. and Li, X. (2018). "Preparation and Anodizing of SiCp/Al Composites with Relatively High Fraction of SiCp." *Scanning*, 2018.

Wang, J., Xie, H., Weng, Z., Senthil, T. and Wu, L. (2016). "A novel approach to improve mechanical properties of parts fabricated by fused deposition modeling." *Materials & Design*, 105, 152-159.

Wang, L., Qiu, J., Sakai, E. and Wei, X. (2016). "The relationship between microstructure and mechanical properties of carbon nanotubes/poly(lactic acid) nanocomposites prepared by twin-screw extrusion." *Composites Part A: Applied Science and Manufacturing*, 89, 18-25.

Wang, Y., Shi, J., Han, L. and Xiang, F. (2009). "Crystallization and mechanical properties of T-ZnOw/HDPE composites." *Materials Science and Engineering: A*, 501(1-2), 220-228.

Wang, Z.-P., Huang, Y.-F., Xu, J.-Z., Niu, B., Zhang, X.-L., Zhong, G.-J., Xu, L. and Li, Z.-M. (2015). "Injection-molded hydroxyapatite/polyethylene bone-analogue biocomposites via structure manipulation." *Journal of Materials Chemistry B*, 3(38), 7585-7593.

Wu, Y., Zhu, L., Jiang, H., Liu, W., Liu, Y., Cao, Y. and Zhou, G. (2010). "Engineering cartilage substitute with a specific size and shape using porous high-density polyethylene (HDPE) as internal support." *Journal of Plastic, Reconstructive & Aesthetic Surgery*, 63(4), e370-e375.

Xiang, D., Guo, J., Kumar, A., Chen, B. and Harkin-Jones, E. (2017). "Effect of processing conditions on the structure, electrical and mechanical properties of melt mixed high density polyethylene/multi-walled CNT composites in compression molding." *Materials Testing*, 59(2), 136-147.

Yang, S., Bai, S. and Wang, Q. (2016). "Morphology, mechanical and thermal oxidative aging properties of HDPE composites reinforced by nonmetals recycled from waste printed circuit boards." *Waste Management*, 57, 168-175.

Yang, X., Zhang, L., Chen, X., Sun, X., Yang, G., Guo, X., Yang, H., Gao, C. and Gou, Z. (2012). "Incorporation of B₂O₃ in CaO-SiO₂-P₂O₅ bioactive glass system for improving strength of low-temperature co-fired porous glass ceramics." *Journal of Non-Crystalline Solids*, 358(9), 1171-1179.

Yao, Q., Noeaid, P., Detsch, R., Roether, J. A., Dong, Y., Goudouri, O. M., Schubert, D. W. and Boccaccini, A. R. (2014). "Bioglass®/chitosan-polycaprolactone bilayered composite scaffolds intended for osteochondral tissue engineering." *Journal of Biomedical Materials Research Part A*, 102(12), 4510-4518.

Yeo, T., Ko, Y.-G., Kim, E. J., Kwon, O. K., Chung, H. Y. and Kwon, O. H. (2021). "Promoting bone regeneration by 3D-printed poly (glycolic acid)/hydroxyapatite composite scaffolds." *Journal of Industrial and Engineering Chemistry*, 94, 343-351.

Zeltmann, S. E., Kumar, B. B., Doddamani, M. and Gupta, N. (2016). "Prediction of strain rate sensitivity of high density polyethylene using integral transform of dynamic mechanical analysis data." *Polymer*, 101, 1-6.

Zhao, Y., Song, M. and Liu, J. (2008). "Characteristics of bioactive glass coatings obtained by pulsed laser deposition." *Surface and Interface Analysis: An International Journal devoted to the development and application of techniques for the analysis of surfaces, interfaces and thin films*, 40(11), 1463-1468.

Zheng, X., Zhang, X., Wang, Y., Liu, Y., Pan, Y., Li, Y., Ji, M., Zhao, X., Huang, S. and Yao, Q. (2021). "Hypoxia-mimicking 3D bioglass-nanoclay scaffolds promote endogenous bone regeneration." *Bioactive Materials*, 6(10), 3485-3495.

LIST OF PUBLICATIONS

Sl. No.	Title of the paper	Authors (in the same order as in the paper. Underline the Research Scholar's name)	Name of the Journal/Conference/Symposium, Vol., No., Pages	Month & Year of Publication	Category *
1	Mechanical behavior of additively manufactured bioactive glass/high density polyethylene composites	<u>Praveen Jeyachandran</u> , Srikanth Bontha, Subhadip Bodhak, Vamsi Krishna Balla, Biswanath Kundu, Mrityunjay Doddamani.	Journal of the Mechanical Behavior of Biomedical Materials, 108. (Elsevier, SCIE, SCOPUS, IF-4.042)	April, 2020	1
2	Material extrusion additive manufacturing of bioactive glass/high density polyethylene composites	<u>Praveen Jeyachandran</u> , Srikanth Bontha, Subhadip Bodhak, Vamsi Krishna Balla, Mrityunjay Doddamani.	Composites Science and Technology, 213. (Elsevier, SCI, SCOPUS, IF-9.879)	July, 2021	1
3	Quasi-static compressive behavior of bioactive glass reinforced high density polyethylene composites	<u>Praveen Jeyachandran</u> , Srikanth Bontha, Subhadip Bodhak, Vamsi Krishna Balla, Mrityunjay Doddamani.	Materials letters, 311. (Elsevier, SCI, SCOPUS, IF-3.574)	December, 2021	1
4	Development of Thermoplastic Feedstock Filament for 3D Printing.	<u>Praveen Jeyachandran</u> , Balu Patil, Mrityunjay Doddamani, Srikanth Bontha, Vamsi Krishna Balla.	International Conference on Precision, Meso, Micro and Nano Engineering (COPEM 10), IIT Madras, India.	December, 2017	3
5	Bioglass/Thermoplastic Composite for Biomedical Applications using 3DP	<u>Praveen Jeyachandran</u> , Srikanth Bontha, Subhadip Bodhak, Vamsi Krishna Balla, Mrityunjay Doddamani.	Indian Institute of Metals National Metallurgists' Day – Annual Technical Meeting 2018, Hotel JW Marriott, Kolkata, India.	November, 2018	3

* Category: 1: Journal paper, full paper reviewed 2: Journal paper, Abstract reviewed 3: Conference/Symposium paper, full paper reviewed 4: Conference/Symposium paper, abstract reviewed 5: others (including papers in Workshops, NITK Research Bulletins, Short notes etc.) (If the paper has been accepted for publication but yet to be published, the supporting documents must be attached.)

Praveen J.

Praveen J
Research Scholar

Dr. Srikanth Bontha

Dr. Srikanth Bontha
Research Guide

Dr. Mrityunjay Doddamani

Dr. Mrityunjay Doddamani
Research Guide

BIO-DATA

1. Name: **PRAVEEN J**
2. Father's Name: R JEYACHANDRAN
3. Date of Birth: 02-01-1992
4. Nationality: Indian
5. Marital Status: Married
6. Address:

<i>Permanent Address</i>	<i>Present Address</i>
S/O, R JEYACHANDRAN, B-2, Thendral Nagar, Rajapalayam, Virudhunagar – 626117. Tamil Nadu, India.	Department of Mechanical Engineering, National Institute of Technology Karnataka, Mangaluru, Dakshina Kannada – 575025. Karnataka, India.
7. Mobile Number: +91-759-846-3556
8. Email ID: praveen.rjc92@gmail.com / praveenrjc@yahoo.in
9. Education Qualification:

Qualification	University/Board	Year of passing	CGPA
Ph.D., (Mechanical Engineering)	National Institute of Technology Karnataka, Mangaluru	Pursuing	8.69
M.E., (Production Engineering)	Anna University, Chennai	2015	9.64
B.E., (Mechanical Engineering)	Anna University, Chennai	2013	8.74

I declare that the above information is true and correct to the best of my knowledge.



(PRAVEEN J)